



Stockholm
University

Bachelor Thesis

Degree Project in
Geochemistry 30 hp

Mid-Late Holocene Paleoclimate and Paleoenvironmental Reconstruction from a Peat Core in Danau Padang, Central Sumatra, Using Microbial Membrane Lipids and other Geochemical Methods

Guillermo Jarne Bueno



Stockholm 2022

Department of Geological Sciences
Stockholm University
SE-106 91 Stockholm

Acknowledgements

First of all, I would like to thank my supervisor Rienk Smittenberg for trusting me with this project, and for having confidence in my capabilities. I would also like to give a very special thanks to Petter Hällberg, who not only guided me through all the lab work, but also helped me navigate through the occasionally murky waters of this project (e.g., the peak integration). In addition, he always made me feel welcome during my lab work at SU. Moreover, I am grateful to Julia Steinbach for her assistance in the lab, and to Madalina Jäggi and Negar Naghipour for carrying out the EA-IRMS and radiocarbon analyses, respectively. Furthermore, I would like to express my gratitude to my partner Andrew Nolan, who not only proofread my entire thesis, but who also made sure that I wouldn't have to do any household chores during the final weeks, to guarantee that I would finish this work in time. Finally, I would like to mention my mother Maria Bueno, and my friend Camila Jiménez, for their endless support and encouragement.

Abstract

The Indo-Pacific warm pool (IPWP) plays a key role in the global atmospheric circulation and the global hydrologic cycle. Its expansion, associated to global warming, has been linked to anomalous weather events all around the world. Therefore, it is important to investigate its role in the coupled ocean-atmosphere system, including its relation and response to abrupt climate changes. In this thesis work, an 8,000-year peat core sequence from Danau Padang, Sumatra, is analyzed. This region lies at the western edge of the IPWP. The main focus was to reconstruct paleotemperatures using glycerol dialkyl glycerol tetraethers (GDGTs), membrane-spanning lipids produced by archaea and bacteria. In peats, the relative distribution of GDGTs can be used as proxies for temperature and pH. Current temperatures at the study site remain virtually identical year-round (~ 22 °C). The temperature reconstruction produced by applying a peat-specific calibration shows gradual warming over the last 8,000 years and core top temperatures of ~ 27 °C. The warming amplitude is likely excessively large, and modern temperatures are overestimated by 5 °C. Thus, after ruling out other possible sources of error, it was concluded that a temperature calibration error was the most likely cause of the broad temperature range, suggesting the need for a tropical peat-specific calibration. However, this record most probably remains relevant in a qualitative matter, supported by other temperature records from central western and southwestern Sumatra. The record from Danau Padang is in agreement with climate models, which simulate warming during the second half of the Holocene, as opposed to most proxy records ('Holocene temperature conundrum'). Moreover, there is substantial evidence that a cold event took place between 5,000 and 4,000 years ago, which was also characterized by high erosion rates. $\delta^{13}\text{C}$, $\delta^{15}\text{N}$, and C/N values suggest that C3 plants have been the dominant vegetation type at the study site for the last 8,000 years, which is supported by palynological studies from Danau Padang and other surrounding areas. To reconstruct the paleohydrology, and in the absence of a δD record from the study site, several qualitative indicators inferred from different geochemical signals (Ti/Al, magnetic susceptibility, carbon accumulation rates, density measurements, and *isoGDGTs-0/brGDGTs*) were combined with a $\delta^{18}\text{O}$ speleothem record from the Tangga Cave (Wurtzel *et al.* 2018), which is 200 km northwest of the study site. The analysis of leaf wax n-alkane distributions, as well as their compound specific stable isotopes, could provide more conclusive information about changes in vegetation type, precipitation regimes, and temperature. In conclusion, the temperature record produced in this thesis work shows great promise, being one of the first terrestrial temperature records from the IPWP.

Table of Contents

1. Introduction	6
2. Background	8
2.1 <i>Peat and Peatlands</i>	8
2.2 <i>Study Site</i>	11
2.2.1 <i>Location, Geography, and Geology</i>	11
2.2.2 <i>Vegetation at Danau Padang</i>	12
2.2.3 <i>Current Climate at Danau Padang</i>	13
2.3 <i>Climatological Conditions and Patterns of the Region</i>	15
3. Methods	18
3.1 <i>GDGTs as Paleoenvironmental Proxies</i>	18
3.1.1 <i>GDGTs</i>	18
3.1.2 <i>Isoprenoidal GDGTs</i>	18
3.1.3 <i>Branched GDGTs</i>	20
3.1.4 <i>7-methyl brGDGTs</i>	24
3.1.5 <i>H-GDGTs</i>	24
3.2 <i>Sample Preparation</i>	25
3.3 <i>Lipid Extraction</i>	25
3.4 <i>Fractionation</i>	26
3.5 <i>Sub-sample Preparation for GC-MS and HPLC-MS Analyses</i>	26
3.6 <i>HPLC-MS Analysis and Quantification</i>	27
3.7 <i>Elemental Analysis</i>	28
3.8 <i>XRF and Magnetic Susceptibility Analyses</i>	28
3.9 <i>Chronology</i>	29
4. Results	29
4.1 <i>Core Description and Chronology</i>	29
4.2 <i>GDGTs and Derived Indices</i>	30
4.3 <i>Elemental Analysis (C, N, and their isotopes)</i>	36
4.4 <i>XRF and Magnetic Susceptibility</i>	37
4.5 <i>Bulk Density and Carbon Accumulation Rates</i>	38
5. Discussion	40
5.1 <i>BrGDGTs</i>	40
5.2 <i>Temperature Reconstruction</i>	40
5.3 <i>pH Reconstruction</i>	47
5.4 <i>Vegetation Reconstruction</i>	47

5.5 XRF Measurements.....	48
5.6 Precipitation and Input of Minerogenic Material.....	48
5.7 Compiled Paleoclimatic and Paleoenvironmental Reconstruction.....	52
6. Conclusions and Future Prospects.....	53
7. References.....	55
Appendix A. GDGT Results.....	63
Appendix B. Elemental Analysis Results (C, N, $\delta^{13}\text{C}$, and $\delta^{15}\text{N}$).....	78
Appendix C. XRF Results.....	80
Appendix D. Density Measurements and Carbon Accumulation Rate Calculations.....	82
Appendix E. Alternative Chromatographic Peak Integrations.....	84
Appendix F. Other MBT'_{SME} Temperature Calibrations.....	92

1. Introduction

The Indo-Pacific warm pool (IPWP) is a region of the equatorial eastern Indian and western Pacific Oceans where sea surface temperatures (SSTs) remain above 28 °C all year round (Dang *et al.* 2020). The IPWP is the largest source of water vapor, and the region of highest precipitation on Earth, which leads to vigorous atmospheric convection (Niedermeyer *et al.* 2014), although precipitation exceeds evaporation (Gagan *et al.* 2004). Therefore, this region plays a key role in the global atmospheric circulation (Griffiths *et al.* 2010), and the global hydrologic cycle (Niedermeyer *et al.* 2014). The IPWP is directly linked to a range of climate systems: the Intertropical Convergence Zone (ITCZ), The Madden-Julian Oscillation (MJO), El Niño Southern Oscillation (ENSO), the East Asian and the Australian-Indonesian Monsoon systems, the Indian Ocean Dipole (IOD), sometimes also called the Indian Ocean Zonal Mode (IOZM), and other major global climate teleconnections (Niedermeyer *et al.* 2014; Griffiths *et al.* 2010; Kuhnert *et al.* 2014). The IPWP is thought to affect global climate from interannual to millennial timescales (Gagan *et al.* 2004).

The IPWP has been expanding on average over $2 \times 10^5 \text{ km}^2$ per year since the beginning of the 20th century, and more than $4 \times 10^5 \text{ km}^2$ per year since the 1980s, due to a rise in SSTs associated with human-induced climate change (Roxy *et al.* 2019). This has led to increased rainfall over Southeast Asia, northern Australia, the Amazon rainforest, and southwest Africa, as well as drying over the west coast of the tropical Americas (Roxy *et al.* 2019). Evidence suggests that the expansion of the IPWP is linked to changes in the MJO, which in turn have been associated with extreme weather events such as the recent California droughts, and the Southeast Asia floods of 2011, among others (Roxy *et al.* 2019). Furthermore, the fact that almost 10 % of the world's population lives in Southeast Asia (U.N. 2019) makes it even more important to further investigate the role of the IPWP in the coupled ocean-atmosphere system, including its relation and response to abrupt climate changes (Mohtadi *et al.* 2010). This in turn can improve the prediction of catastrophic weather events, as well as future climate change (Dang *et al.* 2020). To do this, it is necessary to find and collect high-resolution continuous paleoclimatic records, which are mostly found in late Quaternary deposits. Marine sediments have been widely used due to their continuous deposition, abundance, widespread distribution, and large time span (Ruddiman 2014). However, they generally lack the resolution required to study small climate variations. Higher-resolution marine records can be obtained from coral reefs, whereas lake sediments, speleothems, tree rings, and ice cores constitute useful high-resolution terrestrial records (Ruddiman 2014). Nevertheless, the lack of annual growth rings in tropical trees (Gagan *et al.* 2004), the virtual absence of ice records at low latitudes, along with the difficult accessibility of many speleothems, have resulted in a scarcity of continental paleoclimate records from the tropics (Griffiths *et al.* 2010). This is particularly true for the Maritime Continent, which includes the Indonesian Archipelago.

Peat is a type of deposit that is formed from the accumulation of partly decomposed plant remains in wetlands, where anoxic or suboxic conditions prevail (Naafs *et al.* 2019). This oxygen deficiency results in a remarkable preservation of organic matter, which allows for the use of a wide variety of proxies (Naafs *et al.* 2017a) that yield information about past vegetation, climate, hydrology, and other environmental factors, as well as microbial processes

and carbon-cycle dynamics (Hobbie *et al.* 2017; Davies *et al.* 2021; Chambers *et al.* 2012). Peat-based organic proxies include biomarkers, bulk isotope ratios, plant macrofossils, testate amoebae, and pollen grains (Naafs *et al.* 2017a). Nevertheless, small inorganic particles are also well preserved, so inorganic geochemical analyses can provide useful information as well (Weiss *et al.* 2002; Chambers *et al.* 2012). Peat deposits present five advantages compared to most other environmental archives: (i) they are almost entirely constituted of autochthonous organic matter; (ii) they are widely distributed; (iii) they present an array of proxy measures; (iv) they can be dated using radiocarbon techniques; and, in the case of ombrogenous (precipitation-fed) peatlands, (v) they mostly reflect atmospheric processes, since they are isolated from groundwater (Chambers & Charman 2004; Chambers *et al.* 2012). Peatlands cover around 2-3 % of the Earth's land surface, mostly at boreal and northern-hemisphere temperate latitudes (Page *et al.* 2010). However, 11 % of the peatland surface is located within tropical latitudes, 56 % of which is found in Southeast Asia, mostly in Indonesia and Malaysia (Rieley & Page 2016). Peatlands represent important carbon sinks and are therefore key elements in the global carbon cycle (Page *et al.* 2010). Unfortunately, the clearance and unsustainable management of tropical peatland, which are already extensive in Southeast Asia, are major sources of carbon emissions, apart from having other important ecological impacts (Rieley & Page 2016). Thus, the study of tropical peatlands in this region is of particular interest, even more so given the scarcity of current studies on this matter. The increased interest in peat records observed over the last four decades can be attributed to important developments in the understanding of peatland systems, and to the discovery of new organic and inorganic geochemical proxies that have revolutionized paleoenvironmental studies (Chambers & Charman 2004).

The aim of this study is to analyze a peat core from Danau Padang, in the Kerinci area of Sumatra (Fig. 3), spanning from the second half of the Holocene to the present, in order to obtain paleoclimate and paleoenvironmental records to: (i) contribute with new data about climate variability during the Holocene that can potentially be used to tackle the 'Holocene temperature conundrum' (temperature records show gradual cooling during the second half of the Holocene, while climate models simulate warming; Liu *et al.* 2014); (ii) provide a terrestrial record that can be contrasted with pre-existing (mostly marine) records from nearby regions, which in turn can help to improve the calibration of different proxies, as well as to study regional differences in climate (e.g., between terrestrial and marine environments); (iii) obtain important information about peatland composition and dynamics in central Sumatra, which is scarce; (iv) test the methodology and calibration of peat-based organic proxies applied to tropical peat from this region. Thus, this is not an exclusively descriptive study, since it also focuses on evaluating and discussing the implications of the results obtained for the issues mentioned above.

The main focus of this thesis work is the application of geochemical proxies for past temperatures, based on the relative abundances of certain microbial lipids that are found in peats. Glycerol dialkyl glycerol tetraethers (GDGTs) are membrane-spanning lipids produced by archaea and a few select bacteria, and their discovery has led to the development of several new proxies (Schouten *et al.* 2013). Branched GDGTs (*brGDGTs*) are ubiquitous in many terrestrial settings, such as mineral soils and peat (where they are particularly abundant),

although they can also be found in fluvial, lacustrine, and marine environments (Weijers *et al.* 2007; De Jonge *et al.* 2014). In contrast to isoprenoidal GDGTs (*iso*GDGTs), which are archaea-derived, *br*GDGTs have a bacterial origin. They consist of two glycerol groups enclosing two linear C₂₈ alkyl chains, each with 0-2 extra methyl groups (located in the C5-C7 positions) and 0-2 cyclopentane rings (Fig. 8) (De Jonge *et al.* 2013). The degrees of methylation and cyclisation of *br*GDGTs have shown to correlate with mean annual atmospheric temperature (MAAT) and pH, respectively (Weijers *et al.* 2007). This will be the focal point of this project.

The analytical techniques used include: (i) coupled High Performance Liquid Chromatography-Mass Spectrometry (HPLC-MS) for *br*GDGTs analysis; (ii) elemental analysis for C and N contents as well as their stable isotope ratios, used to study vegetation type and degree of decomposition among others; (iii) radiometric dating to build a depth-age model; (iv) and X-ray Fluorescence (XRF) for the relative composition of inorganic elements, which can be used as a proxy for detrital input. Local vegetation assemblages were obtained from a study conducted by Morley (1982) based on pollen analysis.

2. Background

2.1 Peat and Peatlands

Peat is considered a type of soil which is more than 30 cm thick, made of over 65 % organic matter from partially decomposed plant remains (Rieley & Page 2016), and typically acidic (pH 3-6) (Naafs *et al.* 2017a). Peat deposits are commonly comprised of an acrotelm and a catotelm. The former is located above the water table (most of the year) and therefore oxic conditions predominate, which facilitate active decomposition (Naafs *et al.* 2017a). Conversely, the catotelm (located below the acrotelm) is permanently water-saturated, and therefore dominated by anoxic conditions, which inhibit decomposition (Naafs *et al.* 2017a). Peats can be divided into ombrogenous and topogenous, depending on their water source. The former typically have a convex surface (Takada *et al.* 2016), a pH lower than 4.0, and are fed by meteoric water (Weiss *et al.* 2002). Therefore, they contain an isotopic signal that reflects the source water composition and the climate conditions in which the plants that form it grew (Tillman *et al.* 2010). The only external input of nutrients in these peatlands are aerosols and dust (Takada *et al.* 2016). Ombrogenous peatlands are sometimes referred to as true peat swamps. Conversely, topogenous peatlands are found along the margins of lowland rivers, are formed by their flooding, and normally have a pH higher than 4.0 (Weiss *et al.* 2002; Takada *et al.* 2016). Peatlands can be found at all latitudes where waterlogged and oxygen depleted conditions exist (Naafs *et al.* 2017a). These conditions are dependent on topography, the silt content in rivers (must be low for topogenous peat to form), and net evaporation (precipitation must exceed evaporation, for ombrogenous peats to form) (Takada *et al.* 2016). Moreover, the degree of decomposition is also dependent on the chemical conditions of the soil. For instance, low pH and high levels of sulfur limit microbial activity, which inhibit decomposition (Takada *et al.* 2016). Peatlands can present a wide range of vegetation types, with high- and middle-latitude ombrogenous peatlands being typically dominated by *Sphagnum* (peat moss), sub-

tropical peatlands being characterized by *Sagittaria* (arrowhead) and *Cyperaceae* (sedge), and tropical peatlands, where peat-swamp forests can grow (Naafs *et al.* 2017a).

The northern hemisphere hosts about 89 % of the peat area (Fig. 1), which is primarily located in low temperature and high precipitation areas with even topography (Rieley & Page 2016). This includes large areas in northern Europe and North America, where peat is derived predominately from the remains of mosses, shrubs, and small trees (Rieley & Page 2016). Peatlands in the southern hemisphere are much rarer, and are mostly found in Argentina, Chile, and New Zealand (Chambers & Charman 2004). Tropical peatlands are most abundant in Southeast Asia, Africa, Central and South America (Page *et al.* 2010), and they are primarily made of the remains of rainforest vegetation, although high-altitude tropical peatlands can resemble those from higher latitudes (Rieley & Page 2016). More than half of the global tropical peatland area is concentrated in Southeast Asia, primarily in Indonesia and, to a considerably lesser extent, in Malaysia (Fig. 2) (Page *et al.* 2010). Within Indonesia, Sumatra hosts the largest area of peatland. It is considered that most tropical peatlands are ombrogenous. Peat deposits in Indonesia can be up to 20 m thick and date back to the late Pleistocene (Takada *et al.* 2016). Indonesian peatlands primarily host peat swamp forests and can be classified based on their hydrological and geological characteristics into: (i) coastal peatlands, located along coastal and deltaic areas where peat has accumulated over ocean sediments (Page *et al.* 2010); (ii) transitional peatlands, which are further inland and at higher elevations; and (iii) inland peatlands, which are far from the coast (Osaki *et al.* 2016; Page *et al.* 2010). Additionally, some isolated deposits have formed around lakes (Page *et al.* 2010). Such is the case for the sediments analyzed in this study.

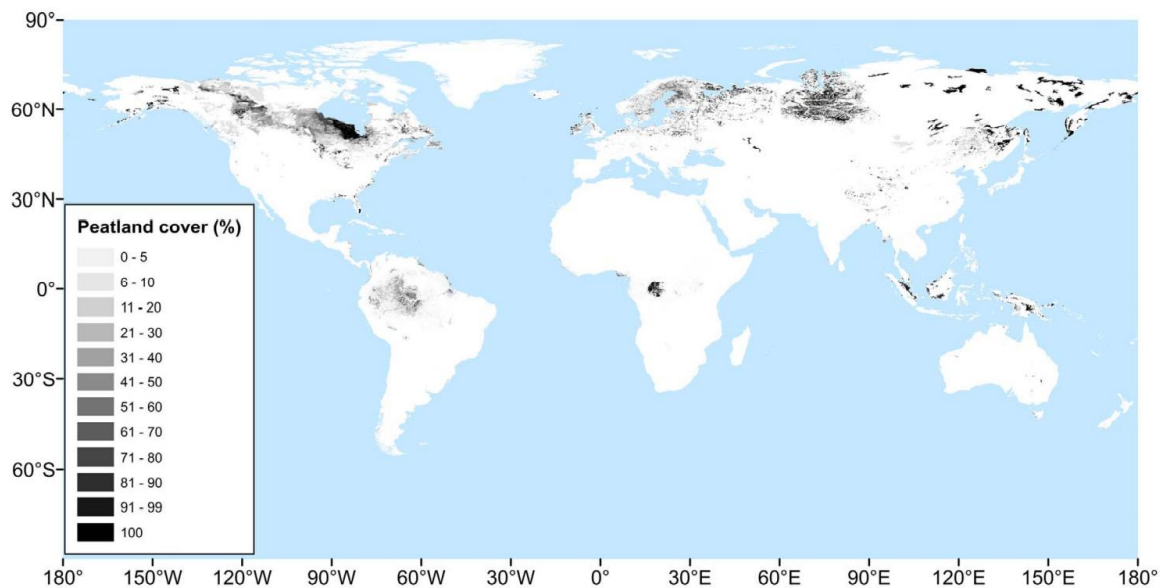


Figure 1. Global distribution of peatland according to PEATMAP, based on a meta-analysis by Xu *et al.* 2018. Figure from Xu *et al.* 2018, reproduced with permission from Elsevier. Note that almost 90 % of the peatland area occurs in the northern hemisphere at middle and high latitudes.

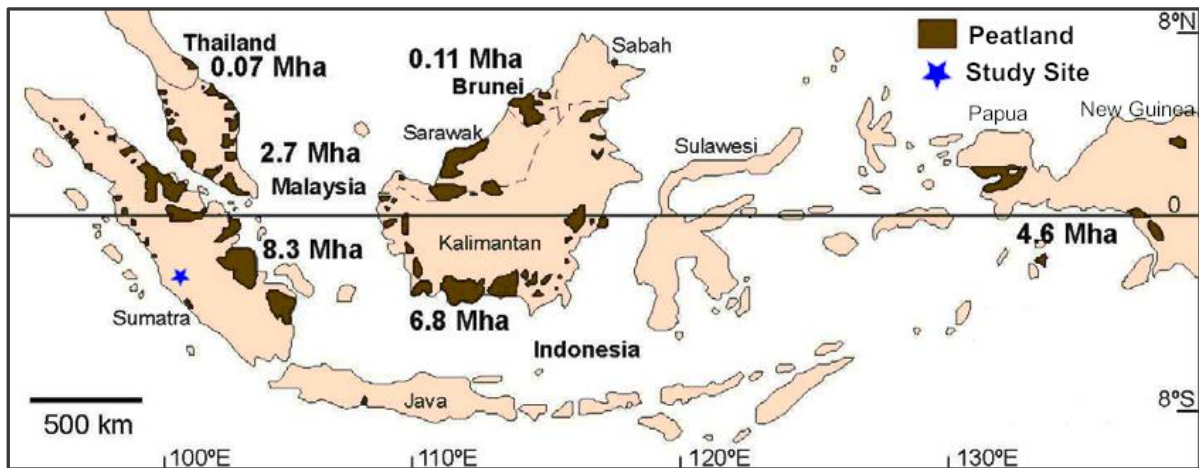


Figure 2. Distribution of peatlands (in million ha) in Southeast Asia, and the location of the study site (Danau Padang, central Sumatra). Figure adapted from Page *et al.* 2004, with permission from John Wiley & Sons, Inc.

Peatland ecosystems are large net carbon absorbers in their natural state. Nevertheless, their destruction, primarily by human activity, has been causing huge amounts of carbon to be released into the atmosphere in a very short time, which unfortunately exacerbates human-induced climate change (Osaki 2016). The conversion of peatland forests into industrial agricultural fields is accompanied by the drainage of peat, which in turn becomes oxidized, leading to the release of its carbon as a consequence of decomposition (Osaki 2016). Fire is often used as the preferred land clearance mechanism, accelerating the release of carbon and causing grave loss of biodiversity (Rieley & Page 2016). These problems are particularly widespread in Southeast Asia, where peat deforestation, as well as anthropogenic and wildfires, have turned this area into a significant source of atmospheric carbon (Rieley & Page 2016). In the case of Indonesia, deforestation and peat drainage was initially aggravated by the government's 'Transmigration Programme', aimed to relocate people from densely populated areas. However, palm oil and paper pulp plantations have become the main contributors to this issue in the past few decades (Rieley & Page 2016). Droughts associated with the increased frequency and intensity of El Niño events, have caused widespread fires, such as those experienced in 1997 and 2002, aggravating peatland destruction even further (Osaki *et al.* 2016). Thus, it is of prime importance to better understand the interactions between the climate in Southeast Asia, the global climate, and peatland clearance. The use of peatland for agriculture in Indonesia is a practice that originated among indigenous communities thousands of years ago, but that has only become unsustainable relatively recently (Osaki *et al.* 2016). The main conundrum regarding peatland use and management coincides with one of the principal challenges that humanity faces today, which is, in the words of Joosten (2016:45): "how to reconcile the short-term demands of people with the long-term interests of society".

The ideas that coal originates from peat and that during the Carboniferous, tropical climate conditions were widespread, had already been proposed in the late 18th century by Franz von Beroldingen (Joosten 2016). However, it was not until 1909 that the scientific community finally accepted the evidence supporting that peat could form in the tropics, and not only in cold regions, after the publication of *Die Tropen-Sumpfflachmoor-Natur der Moore des*

produktiven Carbons (The tropical swamp fen character of the peatlands of the productive Carboniferous) by Henri Potonié (1909). Until then, most scientists argued that organic matter in the tropics would decompose too quickly to form peat. Potonié sustained, however, that only topogenous peatlands could exist in the tropics, which was later refuted by Elisabeth Polak, in 1933 (Joosten 2016).

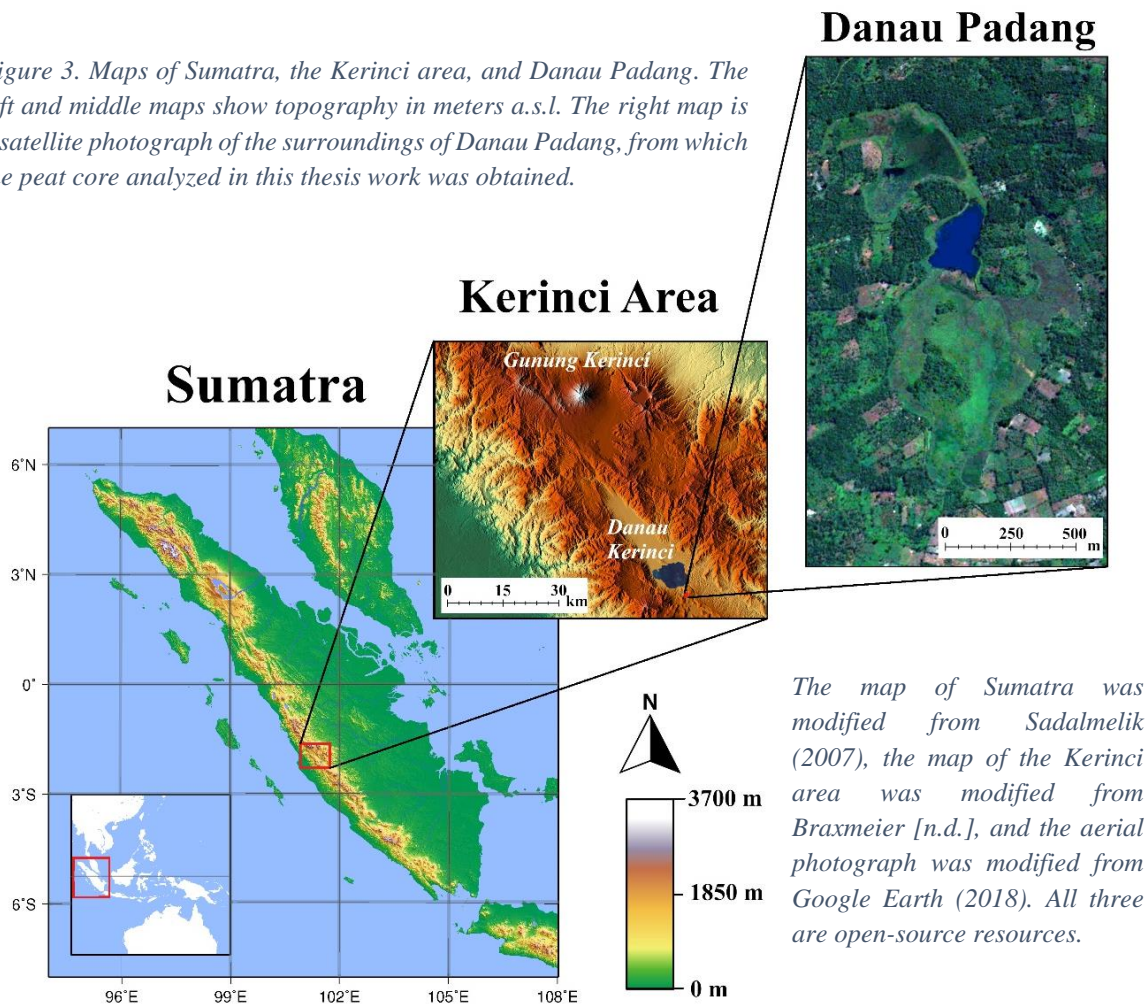
Until the 1980s, peat deposits had not been considered useful archives of paleoclimate and paleoenvironmental changes (Chambers *et al.* 2012). Barber (1981) changed this when he proposed that peatlands provide a continuous record of paleohydrologic conditions, which contradicted the then widely accepted ‘cyclic peat bog regeneration’ hypothesis (Chambers *et al.* 2012). The acceptance of peatlands as archives of Holocene, and sometimes Pleistocene, climate change has increased rapidly since then.

2.2 Study Site

2.2.1 Location, Geography, and Geology

The peat core analyzed in this study (RP-1A-REPA) was extracted in March 2018 by a team from the State University of Padang (Indonesia) and the Nanyang Technological University (Singapore), from Danau (lake) Padang, with coordinates 2°12'17''S and 101°31'36''E. Danau Padang is situated in the southern part of the Kerinci Regency, which in turn is located in the Jambi province of Central Sumatra (Indonesia). The Kerinci area lies in the middle of the Barisan Mountains, where the Kerinci (rift) Valley spans from about 12 km southeast of Kaju Aro, to Danau Kerinci, which has a surface of circa 55 km² (Morley 1982). The rift valley, which lies on a geological fault line, widens from approximately 2 km at its northern-most part to about 15 km at its southern end, which are delimited by Gunung (mount) Kerinci (3,700 m a.s.l.) and subsidiary volcanoes (Gunung Tua & Gunung Raja, among others), respectively. Danau Padang is located approximately at 959 m a.s.l. (above sea level), at the border between montane and lowland rainforests. It consists of a 2 km x 0.4 km valley bog where swamp forest and herbaceous swamp vegetation are dominant (Morley 1982), and an open water body of approximately 50,000 m² is present. It is surrounded by rolling hills that rise up to 300 m above the base topography. The bedrock of the area consists of intermediate and mafic volcanic rock (Morley 1982).

Figure 3. Maps of Sumatra, the Kerinci area, and Danau Padang. The left and middle maps show topography in meters a.s.l. The right map is a satellite photograph of the surroundings of Danau Padang, from which the peat core analyzed in this thesis work was obtained.



2.2.2 Vegetation at Danau Padang

The vegetation in the Kerinci area is mainly dependent on altitude, ranging from rain forests at 1,000 m a.s.l. to tropical shrubs and herbs near the top of Gunung Kerinci (3,600 m a.s.l.) (Morley 1982). Most of the area below 1,300 m a.s.l. has been cleared of its original vegetation cover. Morley made a reconstruction of the swamp vegetation surrounding Danau Padang in 1982 (Fig. 4 & Table 1). This vegetation distribution does not match that of today, but it is nonetheless relevant, since it yields information about past plant communities, some of them natural of this peatland. The aerial photograph from Figure 4 reveals how much of this land has been cleared in the last four decades.

Figure 4. Difference in vegetation cover in Danau Padang over the last four decades. The map on the left-hand side was redrawn from Morley (1982) and it shows the vegetation cover of the area in 1982. Note that this figure is only an approximation, since georeferencing was not possible. The map legend is explained in Table 1 (below). The vegetation data was obtained from Figure 5 of Morley (1982). The satellite aerial photograph used as a background (left-hand side) was taken in 1985 and was obtained from Google Earth. The photograph on the right-hand side was taken in 2018 and was modified from Google Earth.

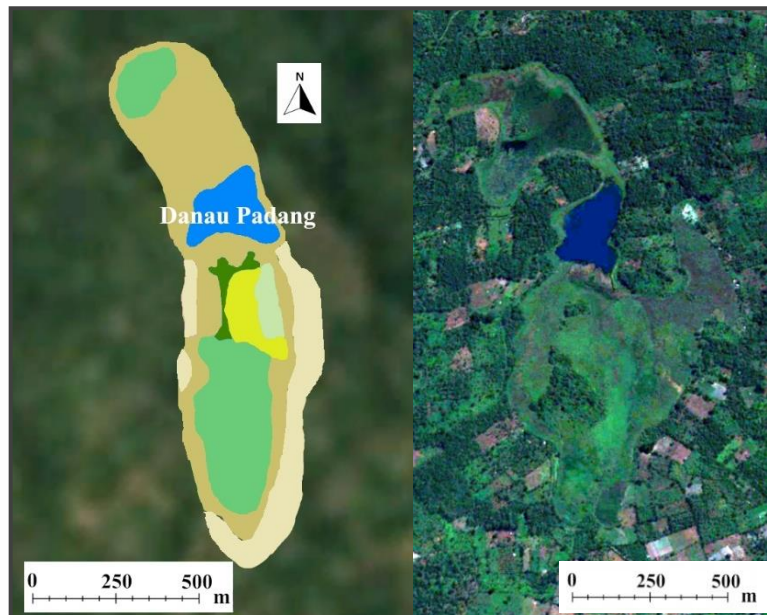





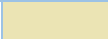


Table 1. Description of the different vegetation types found in Danau Padang, as well as legend for Figure 4. Data from Morley (1982).

Vegetation Type	Color	Description	Comments
Herbaceous swamp		Dominated by <i>Machaerina rubiginosa</i> .	The presence of sporadic woody trees and shrubs indicated unstable vegetation, and hinted the existence and relatively recent disappearance of a previous vegetation cover.
Pteridium swam		Overwhelmingly dominated by <i>Pteridium aquilinum</i> .	This type of vegetation occupied areas where clear signs of recent fires were found.
Euodia swamp forest		Presents a canopy of approximately 10 m high, dominated by <i>Euodia macrophylla</i> .	This patch of vegetation is thought to be regenerated due to the presence of regrowth taxa, and the fact that woody peat is underlain by less woody material.
Myrsine swamp forest		Its canopy is shorter than 5 meters, dominated by <i>Myrsine affinis</i> . However, it displays great taxonomic diversity.	Due to its high diversity and absence of regrowth vegetation, this vegetation type is thought to be one of the natural communities of this peatland.
Ilex cymose swamp forest		Although dominated by <i>Ilex cymose</i> trees, forming a canopy of roughly 20 meters in height, it is also highly diverse.	Ilex cymose swamp forest is also thought to be one of the natural communities of this peatland.
Rice paddy			

2.2.3 Current Climate at Danau Padang

The Depati Parbo weather station is the nearest one to Danau Padang, located 14 km to the northwest. The mean annual atmospheric temperature (MAAT) recorded at this weather station was roughly 23 °C (Fig. 5) during the period 1980-2016 (Weatherspark [2017]). This weather station is located approximately at 790 m a.s.l., so given that the lapse rate of the troposphere at low latitudes is usually 6.0 °C/km (Ruddiman 2014), the estimated MAAT at Danau Padang

is approximately 22 °C (Fig. 5). This is slightly warmer than the estimated MAAT reported by Morley (1982), which was somewhat above 20 °C in 1982. This could be partially explained by the measured increase in atmospheric carbon dioxide from 341 ppm in 1982 to 403 ppm in 2016 (NOAA 2021), and the subsequent greenhouse warming associated with it. Monthly rainfall values are given in Figure 6. The mean annual rainfall for the period 1980-2016 recorded at Depati Parbo was just below 1700 mm (Weatherspark [2017]), with a monthly average of roughly 140 mm. This is in agreement with the rainfall values reported by Raflus *et al.* (2018) for Sungai Penuh, a town located 7.5 km to the northwest of Depati Parbo. During 1980-2016, the average monthly rainfall between October and April was above 140 mm, peaking in November at over 200 mm. Between May and September the average monthly rainfall was below 140 mm, with the minimum in July, at slightly below 90 mm.

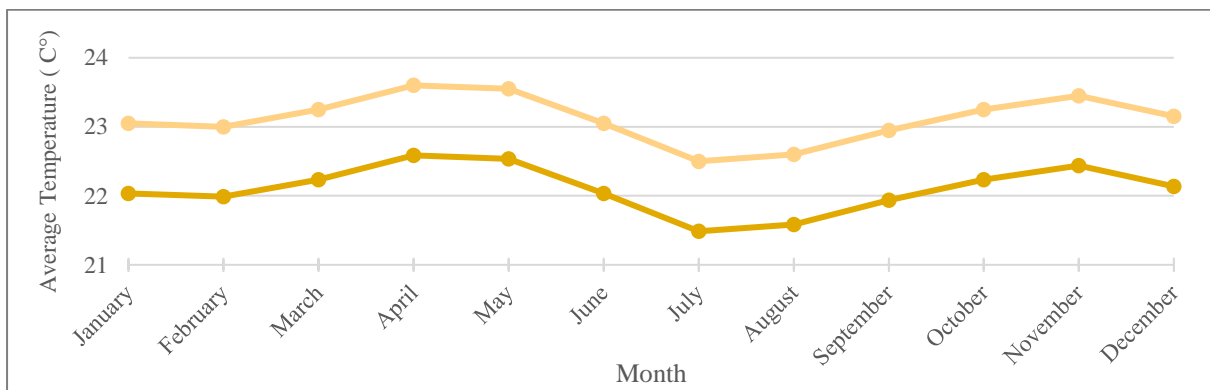


Figure 5. Average monthly temperatures recorded at the Depati Parbo weather station (pale orange), at 790 m a.s.l., and estimated for Danau Padang (dark orange) at 959 m a.s.l., for the period 1980-2016. Data from weatherspark [2017], and estimations for Danau Padang (central Sumatra) calculated using a lapse rate of 6.0 °C/km. Note that there is negligible seasonal temperature variability due to proximity to the equator.

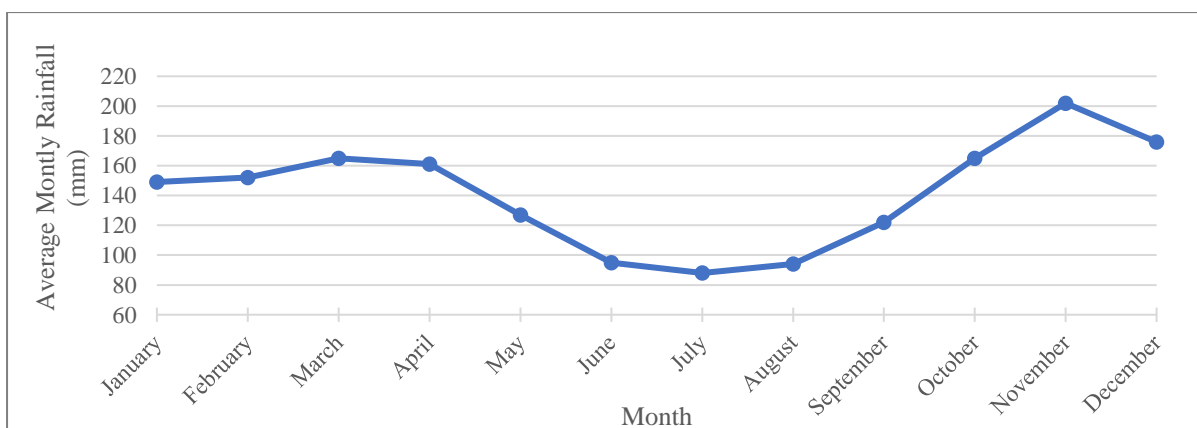


Figure 6. Average Monthly rainfall values recorded at the Depati Parbo weather station (Sumatra) for the period 1980-2016. Data from weatherspark [2017]. The wet season, associated with the northwest monsoon, occurs during the austral summer, while the dry season, linked to the southeast monsoon, occurs during the austral winter.

2.3 Climatological Conditions and Patterns of the Region

The ITCZ is the region near the equator where northern and southern trade winds meet, causing the air to rise and cool, which leads to intense precipitation (Ruddiman 2014). As it was mentioned in the introduction, the IPWP plays a key role in the global climate system. Vigorous convection and precipitation take place in this region, making it an important component of global climate teleconnections (Kuhnert *et al.* 2014). Within the IPWP, precipitation slightly exceeds evaporation, stabilizing the upper ocean and producing a shallow mixed layer in this region (Gagan *et al.* 2004). Equatorial trade winds drive and accumulate warm surface waters in the IPWP (Dang *et al.* 2020). Some of the collected heat is released to the atmosphere, driving powerful atmospheric convection and transporting air toward the poles. Rapid surface cooling at the poles and an increase in ocean water salinity (due to salt rejection during ice formation) cause the water to sink and allow for the formation of deep water, which flows ascending back toward the equator driven by thermohaline circulation (Ruddiman 2014; Gagan *et al.* 2004). The combination and balance of these processes lead to the stabilization of the IPWP (Gagan *et al.* 2004). Shifts in the ITCZ, which in turn affect monsoonal winds, exert control over the regional hydrology in the IPWP on a seasonal basis (Niedermeyer *et al.* 2014). Seasonal changes in insolation cause the ITCZ to move northward during the boreal summer and southward during the austral summer (Ruddiman 2014).

The difference in heat capacity between the ocean and land is responsible for the monsoons. During the summer, continents heat up faster than the ocean, due to the higher heat capacity of water, which causes air to rise, producing a low-pressure zone over the continent (Ruddiman 2014). This causes moist air to flow from the ocean to land, which gradually heats up and ascends. Water vapor condenses as the moist air rises and cools, releasing great amounts of water in the form of precipitation. This is known as the summer monsoon. Conversely, the winter monsoon is characterized by precipitation out in the ocean, due to the more rapid cooling of land surfaces compared to water, which creates a low-pressure zone over the ocean, and a high-pressure zone over the continent (Ruddiman 2014). Indonesia lays within the southern sector of the ITCZ, where rainfall is dominated by the Australian-Indonesian monsoon system, which is responsible for approximately 70 % of the annual precipitation in the region (Griffiths *et al.* 2010). During the boreal winter, monsoon winds blow from the Eurasian continent to Australia, passing through the Bay of Bengal and carrying warm and moist air to Indonesia, delivering abundant precipitation (Setiawan *et al.* 2015). This is also known as the northwest monsoon season in austral Indonesia, since winds blow from the northwest in the southern hemisphere. Conversely, during the austral winter, winds blow from the Australian continent toward Asia, in an easterly direction in the southern hemisphere (Wheeler & McBride 2012). This southeast monsoon represents the dry season over austral Indonesia. Changes in the strength and timing of the Australian-Indonesian monsoon can have devastating consequences for the millions of people that live on the Maritime Continent, particularly in Indonesia (Griffiths *et al.* 2010). Hence, it is essential to improve our understanding of the factors that have influenced monsoon variability in the past and in the present.

The MJO is considered the strongest mode of intraseasonal variability in the Asian-Australian monsoon region, and in the tropics in general (Wheeler & McBride 2012). The MJO

is characterized by a band of rainclouds and winds that moves eastward within tropical latitudes (Roxy *et al.* 2019). Normally, MJO events begin over the Indian Ocean, and they weaken as they move eastward over the central Pacific, although some can travel much further east, reaching the Atlantic and beyond (IITM [2019]). The MJO is more intense during the boreal winter and spring, and weaker during the summer and fall seasons (Goswami 2012). The IPWP has expanded from $2.2 \times 10^7 \text{ km}^2$ during the period 1900-1980 to $4 \times 10^7 \text{ km}^2$ during 1981-2018 (Roxy *et al.* 2019). This expansion has not been uniform, with more warming over the west Pacific than over the Indian Ocean. This temperature gradient drives moisture from the Indian Ocean to the west Pacific, enhancing cloud formation in the latter (IITM [2019]). Therefore, the expansion of the IPWP has led to important alterations in the life cycle of MJO events. During the period 2000-2018, compared to 1981-1999, the residence time of convective cloud bands associated with the MJO increased by over five days over the Maritime Continent and the west Pacific, while it was reduced by more than 3 days over the Indian Ocean (Roxy *et al.* 2019). These changes have caused increased rainfall over the Maritime continent, northern Australia, the west Pacific, the Amazon basin, and southwest Africa (IITM [2019]). Simultaneously, precipitation has decreased over the central and east Pacific, east Africa, both coasts of the United States, and the Ganges and Yangtze basins in India and China, respectively (Roxy *et al.* 2019). The MJO regulates monsoons, ENSO events, and the formation of tropical cyclones (Roxy *et al.* 2019). It can affect and initiate extreme weather events all around the globe, such as hurricanes, floods, droughts, and extreme temperatures (IITM [2019]). For instance, many of the recent droughts in California and Africa, as well as the southeast Asia floods (in 2011), have taken place during years when the MJO residence time over the Indian Ocean was reduced (Roxy *et al.* 2019).

On an interannual scale, the role of the tropics in the climate system, as well as changes in the hydrology of the IPWP, are mainly governed by the ENSO and the IOD (Niedermeyer *et al.* 2014). Both are characterized by temperature and precipitation anomalies, the former taking place in the Pacific, while the latter takes place in the Indian Ocean. Under normal conditions, there is a positive W-E temperature and precipitation gradient over the Indian Ocean. During positive IOD events, anomalous cooling and decreased precipitation take place over the eastern Indian Ocean (Indonesia), while the western Indian Ocean (East Africa) becomes warmer, which is accompanied by increased rainfall (Duvel 2012). This results in a weakening or even reversal of the Indian Ocean precipitation gradient (Niedermeyer *et al.* 2014). Negative IOD events are characterized by the opposite anomalies. It has been proposed that patterns similar to current IOD events have contributed to climate variability during the Holocene, but also acting from multidecadal to millennial time scales (Kuhnert *et al.* 2014).

El Niño-Southern Oscillation is a variation in the winds and ocean currents of the tropical Pacific Ocean that occurs at irregular intervals that range from two to seven years (Ruddiman 2014). During normal (non-El Niño) conditions, the higher SSTs of the western Pacific (in the IPWP) lead to increased evaporation and precipitation in this area. This generates a low-pressure zone where air rises and flows toward South America, where it cools and sinks, resulting in a high-pressure zone. This convective cell, also known as the Walker Circulation, causes strong trade winds to drive warm surface waters westward, leading to the upwelling of deep (cooler and nutrient-rich) waters along the west coast of South America (Ruddiman 2014).

During non-El Niño years, rainfall is scarce along the coast of South America due to the relatively cold SSTs, and the consequent low evaporation rates. Conversely, during El Niño events, the IPWP, and therefore the low-pressure zone, shift eastward, reaching the central Pacific (Gagan *et al.* 2004). Weaker trade winds fail to push water westward along the Pacific, southerly trade winds along the coast of South America weaken, and as a result, upwelling does not take place. The lack of nutrients causes ecological devastation, affecting fish, sea birds and mammals (Ruddiman 2014). Ultimately, it also affects humans due to the scarcity of fish available for fishing. Moreover, the rearrangement of the convective centers in the Walker Circulation of the Pacific leads to the formation of a low-pressure zone over the eastern tropical Pacific. This in turn is responsible for heavy cloud formation and precipitation that can bring about flash floods, affecting the west coast of South America (Ruddiman 2014). Additionally, El Niño conditions result in drying in Northern Australia and the Maritime Continent. Lastly, La Niña events occur when abnormally strong trade winds, and the increased upwelling associated with them in the eastern tropical Pacific, lead to exceptionally cool SSTs in this region (Gagan *et al.* 2004; Ruddiman 2014). This displaces the IPWP westward and the tropical western Pacific, including the Maritime Continent and Northern Australia, exhibit abnormally high amounts of precipitation (Gagan *et al.* 2004). ENSO variability has increased during the 20th and 21st centuries in association with greenhouse warming (Dang *et al.* 2020). Therefore, studying the variability of the ENSO during the Holocene is highly relevant for the understanding and prediction of future climate change.

The western and southern coasts of Sumatra and Java, respectively, are dominated by the South Java Current, which plays a key role in the distribution of freshwater in and out of the southeastern Indian Ocean (Sprintall *et al.* 2010). During the northwest monsoon season, and particularly during monsoon transitions that take place around April-May and October-November each year (Sprintall *et al.* 2010), low-salinity warm waters are transported from the warm pool region of the eastern equatorial Indian Ocean toward the southeast (Setiawan *et al.* 2015). However, the direction of this current is reversed during the southeast monsoon season, during the austral winter, carrying higher-salinity waters toward the northwest. The winds responsible for the southeast monsoon generate upwelling along the coasts of southern Java and Sumatra (Susanto *et al.* 2001). During El Niño years, anomalously strong easterly winds seem to be associated with the prolongation of upwelling into November and its expansion toward northern Sumatra (Susanto *et al.* 2001). The Indonesian Throughflow (ITF) is another important ocean current in this region, which transports warm waters from the Pacific Ocean into the Indian Ocean via several passages within the seas of the Maritime Continent (Setiawan *et al.* 2015). Since the ITF influences the freshwater and heat fluxes between the Indian and Pacific Oceans, it likely plays an important role in the Asian monsoon and the ENSO (Setiawan *et al.* 2015). Low-salinity and high-temperature waters from the Java Sea flow through the Sunda Strait, which separates Sumatra from Java (Setiawan *et al.* 2015). Precipitation in west Sumatra is mostly derived from the Indian Ocean, since the Barisan Mountains are an orographic barrier for the moisture coming from the Pacific (Niedermeyer *et al.* 2014). From the leeward side of the Barisan Mountains to the east coast of Sumatra, additional moisture is provided from the Pacific (Niedermeyer *et al.* 2014).

3. Methods

3.1 GDGTs as Paleoenvironmental Proxies

3.1.1 GDGTs

Most biological membranes are composed of glycerophospholipids, in which two chains of straight fatty acids are linked to glycerol through ester bonds, with the glycerol being also connected to a phosphate hydrophilic polar head group. Glycolipids are also common, where the polar head group consists of a sugar molecule instead of a phosphate group. Normally, the polarity of these molecules allows for the formation of bilayers, in which the hydrophobic alkyl chains (pointing inward) act as barriers to water and ions. However, many archaea and certain bacteria synthesize membrane lipids consisting of isoprenoid (archaea) or methyl-branched (bacteria) chains, linked to two glycerol moieties through ether bonds, forming a monolayer. These membrane-spanning lipids are called glycerol dialkyl glycerol tetraethers (GDGTs) (Fig. 7 & 8). It is believed that a monolayer and ether bonds increase the stability of the membrane compared to a bilayer and ester bonds (Schouten *et al.* 2013). This is supported by the fact that many extremophilic archaea biosynthesize GDGTs (Schouten *et al.* 2013). However, since the 1970s it has been increasingly evident, particularly in the last two decades, that GDGTs are also produced in mesophilic environments, such as lacustrine and marine environments, mineral soils, and peats (De Jonge *et al.* 2013). Initially, GDGTs were analyzed through GC-MS (Gas Chromatography-Mass Spectrometry) after the cleavage of ether bonds, which was an arduous process that only provided information about the released alkyl chains (Hopmans *et al.* 2016). However, it was not until the 2000s that the study of GDGTs became truly relevant in the field of organic geochemistry, with the development of HPLC-MS (High Performance Liquid Chromatography-Mass Spectrometry) (Hopmans *et al.* 2000). This analytical method led to the discovery of new GDGTs, such as crenarchaeol and several branched GDGTs (*brGDGTs*), including those in their intact form (with their polar head groups) (Hopmans *et al.* 2016). These new GDGTs were then widely found in mesophilic environments, which led to the development of several geochemical proxies used to reconstruct different paleoenvironmental parameters. *BrGDGTs* are predominant in terrestrial environments, while crenarchaeol is mostly found in marine and lacustrine environments (Naafs *et al.* 2016). Furthermore, GDGTs have been used for the tracing of certain taxonomic groups within the Archaea and Bacteria domains, as well as to study carbon acquisition pathways (Schouten *et al.* 2013).

3.1.2 Isoprenoidal GDGTs

Different isoprenoidal GDGTs (*isoGDGTs*) are produced by a wide range of archaea (Naafs *et al.* 2019). However, the use of *isoGDGTs* as proxies is mainly limited to marine and lacustrine environments (Naafs *et al.* 2019). They range from *isoGDGTs-0* to *isoGDGTs-8* depending on the number of cyclopentane moieties (Fig. 7) (Schouten *et al.* 2013). Crenarchaeol, which contains 4 cyclopentane and 1 cyclohexane moieties, is exclusively known to be produced by Thaumarchaeota, which are aerobic ammonia-oxidizing archaea (Naafs *et al.* 2017a). *IsoGDGTs* are commonly found in relatively low concentrations in peat,

where *iso*GDGT-0, which is known to be produced by many archaea including methanogens, is abundant compared to crenarchaeol (Naafs *et al.* 2019). This, along with the fact that the concentration of most *iso*GDGTs increases with depth, suggests that *iso*GDGTs are probably produced by anaerobic archaea, probably methanogens (Naafs *et al.* 2019). Thus, in peat, the relative abundance of *iso*GDGT-0 can be used as a tracer for methanogenic archaea, which are strictly anaerobic microorganisms. Crenarchaeol, however, does not increase in concentration with depth, and it seems to be limited to the oxic acrotelm (Naafs *et al.* 2019). Hence, it is practically absent in relatively wet (with a shallow acrotelm) ombrogenous peats (Naafs *et al.* 2019). Nevertheless, it can be used in relatively dry peats as a proxy for changes in hydrology (changes in the water table) and the microbial community (Naafs *et al.* 2019). Moreover, *br*GDGTs are more abundant in terrestrial environments compared to crenarchaeol, which predominates in marine and lacustrine environments (Hopmans *et al.* 2016). This led to the development of the Branched and Isoprenoid Tetraether (BIT) Index, based on the relative abundances of *br*GDGTs and crenarchaeol (Hopmans *et al.* 2004).

The degree of cyclization of *iso*GDGTs is directly correlated with temperature in marine and lacustrine sediments, and potentially in mineral soils (Naafs *et al.* 2018 & 2019). However, this correlation appears to be absent in peats (Naafs *et al.* 2019). Nonetheless, the relative abundance of *iso*GDGT-5 seems to be dependent on temperature and pH (Naafs *et al.* 2019). *iso*GDGT-5 is only present in notable concentrations (above 1 %) in tropical ombrogenous peats, with a pH lower than 5.1 and a MAAT higher than 19.5 °C (Naafs *et al.* 2019). Such is the case for the peat studied in this project (from Danau Padang). However, further research is needed, and therefore this proxy was not applied in this thesis work.

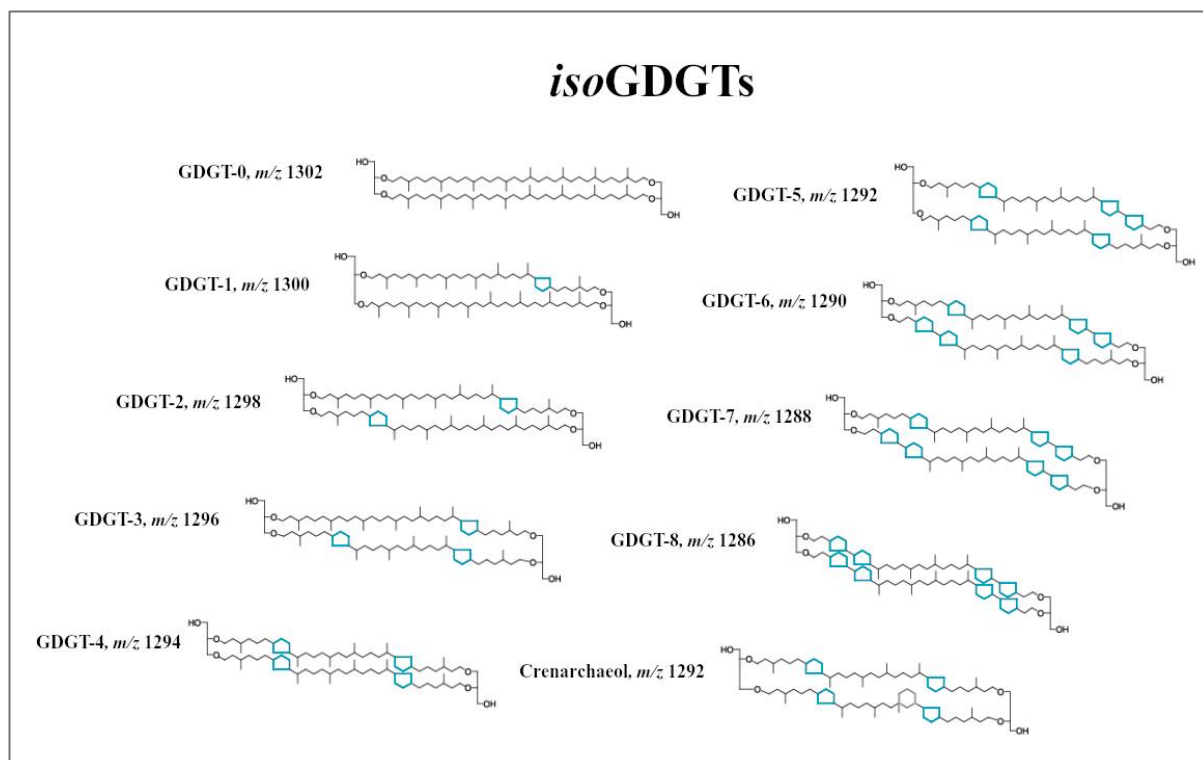


Figure 7. Chemical structure of isoprenoidal GDGTs, and their mass-to-charge ratios (*m/z*). Figure redrawn from Schouten *et al.* 2013.

3.1.3 Branched GDGTs

These membrane-spanning lipids were first identified in the 1980s through the release of 13,16-dimethyl-octacosane hydrocarbons via ether bond cleavage (Chappe *et al.* 1982). However, they were not reported in their intact form until the early 21st century, when they were found by Sinninghe Damsté *et al.* (2000) in a peat from the Netherlands. *BrGDGTs* are abundant in mesophilic environments, particularly in terrestrial sediments, such as peat and mineral soils (Schouten *et al.* 2013). Nonetheless, they can also be found in marine and lacustrine environments (Naafs *et al.* 2017b). Even though the exact biological source of *brGDGTs* is still under debate, their branched skeleton and glycerol stereochemistry suggest that they are produced by bacteria (De Jonge *et al.* 2014). Given that in peat the concentration of *brGDGTs* increases with increasing depth, and that the highest abundance is found in the anoxic catotelm, it has been suggested that they are synthesized by anaerobes (Schouten *et al.* 2013). The correlation between $\delta^{13}\text{C}$ values found in the alkyl moieties of *brGDGTs* and those of the bulk organic matter that contains them, imply a heterotrophic origin (Schouten *et al.* 2013; Naafs *et al.* 2019). *BrGDGT-Ia* (Fig. 8) has been linked to some strains of acidobacteria, such as those present in *Sphagnum* peat (Schouten *et al.* 2013). However, these strains of bacteria are aerobes and do not appear to produce other *brGDGTs*, suggesting that there are different bacteria that can biosynthesize them (Naafs *et al.* 2019). The (limited) culture data available at the present time indicates that the production of *brGDGTs* is favored at suboxic (rather than anoxic) conditions, which is in accordance with the idea that *brGDGTs* are produced by facultative anaerobes (Naafs *et al.* 2019). Nonetheless, further research is required.

In living organisms, *brGDGTs* possess polar head groups, such as glucose, glucuronyl, phosphoglycerol, and phosphohexose, all of which have been identified in peat (Naafs *et al.* 2019). However, the polar head groups are lost following the death of the source organism (Naafs *et al.* 2019). They are highly stable lipids whose carbon skeletons (core lipids) can be preserved in the environment for up to 55 Ma (De Jonge *et al.* 2014).

BrGDGTs can contain from 4 to 6 methyl groups, indicated by Roman numerals (I, II, or III, respectively) (Naafs *et al.* 2019). These can be found normally at the C-5 (α and/or ω -5) and C-6 (α and/or ω -6), and occasionally at the C-7 (α and/or ω -7), positions, the second and the latter being represented by a prime and a double prime symbol respectively (Naafs *et al.* 2019). Additionally, *brGDGTs* can include from 0 to 2 cyclopentane moieties indicated by the letters a, b, or c respectively (Naafs *et al.* 2019).

The first time *brGDGTs* were used as proxies was when Weijers *et al.* (2007) found a strong negative correlation ($R^2 = 0.7$) between the degree of Cyclization of Branched Tetraethers (CBT) and soil pH. Furthermore, the degree of Methylation of Branched Tetraethers (MBT) was shown to be linked to both MAAT ($R^2 = 0.62$) and pH ($R^2 = 0.37$) in mineral soils, which led to the combined MBT/CBT paleothermometer ($R_2 = 0.77$). This paleothermometer would be later refined by Peterse *et al.* (2012). Higher CBT values of *brGDGTs* were observed at higher pH in mineral soils and peats, while the opposite trend was found for *isoGDGTs* in hot springs (Naafs *et al.* 2019). The CBT and MBT proxies were mainly applied to mineral soils until the last decade, when they began to be used in peat. Ballantyne *et*

al. (2010) used *brGDGTs* to estimate paleotemperatures from an Arctic lignite, and Weijers *et al.* (2011) applied them to a modern peat core from France. They discovered that MAATs at the top of the peat were over 5 °C higher than those instrumentally measured, and that shifts in vegetation were accompanied by changes in the CBT (Weijers *et al.* 2011). Further studies confirmed that abnormally high temperatures and pH values were obtained when using soil-based calibrations applied to peats, compared with the values obtained by instrumental measurements (Naafs *et al.* 2017a). These discoveries suggest that pH and temperature proxies might be affected by changes in the trophic status, and that peat-specific calibrations are necessary for the reliability of these proxies (Weijers *et al.* 2011). Peat differs from mineral soils in that they are water saturated, they have a higher content of organic matter, and lower pH. This means that peats become anoxic at relatively shallow depths compared to mineral soils, affecting the distribution of GDGTs (Naafs *et al.* 2017a). Additionally, Weijers *et al.* (2011) demonstrated that most of the *brGDGTs* found in deep peat are indeed of fossil nature.

Two years later, De Jonge *et al.* (2013) reported the discovery of 6-methyl *brGDGTs* (the extra methyl groups are at the position C6) by using a silica (instead of a cyano) column, for better separation, decreasing the co-elution with 5-methyl *brGDGTs*. Furthermore, they reported the existence of additional non-symmetrical isomers. De Jonge *et al.* (2014) discovered that separation, particularly of the penta-methylated *brGDGTs*, was improved after using a sequence of four silica columns. Furthermore, they conducted a study that showed that 6-methyl *brGDGTs* globally comprise an average of 24 % of the total *brGDGTs*, and found a positive correlation between the relative abundance of 6- over 5-methyl *brGDGTs* and soil pH. This allowed for the removal of the pH dependence from the MBT index, leading to the creation of the MBT'_{5ME} index, which excludes 6-methyl *brGDGTs*, decreasing the residual mean error by approximately 1.5 °C (De Jonge *et al.* 2014). Moreover, the new CBT' index, which uses 6-methyl *brGDGTs*, reduced the error to 0.5 pH units in soils (De Jonge *et al.* 2014). Motivated by the previously limited study of GDGTs in peat, Naafs *et al.* (2017a) developed peat-specific calibrations using data from 470 samples from 96 different peatlands. They confirmed the existence of a strong negative correlation ($R^2 = 0.76$) between the MBT'_{5ME} and temperature, whereas the degree of cyclization of certain 5- and 6-methyl *brGDGTs* was linked to pH ($R^2 = 0.58$). The error associated with peat-specific calibrations is around ± 4.7 °C, which makes the use of the MBT'_{5ME} proxy unrecommended for the reconstruction of small temperature changes (< 2 °C) (Naafs *et al.* 2019). Furthermore, MBT'_{5ME} calibrations saturate at temperatures around 25-29 °C, which means that their application to past greenhouse periods should be carried out with particular heed (Naafs *et al.* 2017b).

In the present study, the distribution of *brGDGTs* was used to calculate four indices: MBT'_{5ME}, CBT_{peat}, IR_{6ME}, and IBT. The MBT'_{5ME} index reflects the ratio of tetramethylated to 5-methyl penta- and hexamethylated *brGDGTs* (De Jonge *et al.* 2014):

$$MBT'_{5me} = \frac{(Ia + Ib + Ic)}{(Ia + Ib + Ic + IIa + IIb + IIc + IIIa)} \quad (1)$$

The peat-specific calibration used was the following (Naafs *et al.* 2017a):

$$MAAT_{peat} (°C) = 52.18 \times MBT'5me - 23.05 \quad (2)$$

(n = 96, R² = 0.76, RMSE = 4.7)

Two useful variations of the CBT index have been developed in the last few years. These are the CBT' index (De Jonge *et al.* 2014), which best correlates with pH in mineral soils, and the CBT_{peat} index (Naafs *et al.* 2017a), which, by using exclusively the compounds that are significantly correlated to pH in the numerator, has a stronger correlation in peat:

$$CBT_{peat} = \log \left(\frac{Ib + IIa' + IIb + IIb' + IIIa'}{Ia + IIa + IIIa} \right) \quad (3)$$

Naafs *et al.* (2017a) also developed the following calibration:

$$pH = 2.49 \times CBT_{peat} + 8.07 \quad (4)$$

(n = 51, R² = 0.58, RMSE = 0.8)

The IR_{6ME} index reflects the proportion 6-methyl *br*GDGTs, which was also used as a proxy for pH in a qualitative manner, with a higher fractional abundance of 6-methyl *br*GDGTs (higher IR_{6ME}) being linked to higher pH (Yang *et al.* 2015):

$$IR_{6me} = \left(\frac{IIa' + IIb' + IIc' + IIIa' + IIIb' + IIIc'}{IIa + IIa' + IIb + IIb' + IIc + IIc' + IIIa + IIIa' + IIIb + IIIb' + IIIc + IIIc'} \right) \quad (5)$$

Finally, the IBT (Isomerization of Branched Tetraethers) index is inversely related to the IR_{6ME}, but it only reflects the ratio of 6- to 5-methyl penta- and hexamethylated *br*GDGTs without any cyclopentane moieties (Ding *et al.* 2015):

$$IBT = -\log \left(\frac{IIa' + IIIa'}{IIa + IIIa} \right) \quad (6)$$

In the last few years, further improvements have been made in HPLC separation, mainly by using several UHPLC (Ultra HPLC) columns in tandem (Becker *et al.* 2013; Yang *et al.* 2015; Hopmans *et al.* 2016). The separation achieved by De Jonge *et al.* (2014) was matched by the use of two UHPLC columns, but the latter showed further improvements in resolution and sensitivity, while reducing the run time of each sample (Hopmans *et al.* 2016). Further improvements in separation can be expected by the addition of more UHPLC columns, but other advances will be necessary to maintain reasonable analysis times.

The fractional abundances of the different 6-methyl *br*GDGTs correlate positively with each other, suggesting a common biological source (De Jonge *et al.* 2014). Arid soils have been found to have a higher pH, and a higher ratio of 6-methyl *br*GDGTs, compared to other soils, particularly peats (Naafs *et al.* 2017b). This could be explained by assuming that different communities that thrive in different environments produce discrete ratios of 5- to 6-methyl *br*GDGTs (Naafs *et al.* 2017b). Alternatively, it has been speculated that 6-methyl (rather than 5-) groups might provide greater membrane fluidity in dry or alkaline soils, similar to how in fatty acids, 2-methyl groups (rather than 1-) increase it (Naafs *et al.* 2017b).

The trend of lower temperatures being associated with a higher degree of methylation of *br*GDGTs has been observed both in mineral soils and peats (Naafs *et al.* 2017b). This suggests that *br*GDGTs have a common bacterial source in both environments (Naafs *et al.* 2019). An explanation for this correlation was proposed by Weijers *et al.* (2007), who argued that the additional methyl groups would decrease the packing of the membrane lipids, increasing membrane proton permeability, and allowing bacteria to maintain membrane fluidity at lower temperatures. Note that this correlation has not been observed in lacustrine sediments, and therefore, special attention must be paid across changes between lacustrine sediments and peat (Naafs *et al.* 2019). Huguet *et al.* (2014) studied the impact of a weak increase in temperature on *br*GDGTs distributions and the speed of adaptation of the source bacteria. In order to do so, analyses were conducted in *Sphagnum* peat cores from eastern France, under controlled conditions at 12 and 15 °C, over a 12-month period. The results suggested that the turnover time of *br*GDGTs in their intact polar form at the peat surface is between 3 months and 1 year, while no significant change was observed in the core lipid fraction (without polar head groups). This means that the core lipids probably have a turnover of at least one year in peat, and that the source organisms that produce *br*GDGTs can adjust the composition of the membrane lipids in between 3 months and 1 year. Other studies have estimated a turnover of *br*GDGTs of several decades (Weijers *et al.* 2010; Peterse *et al.* 2010). However, further research is required in order to obtain more conclusive turnover times.

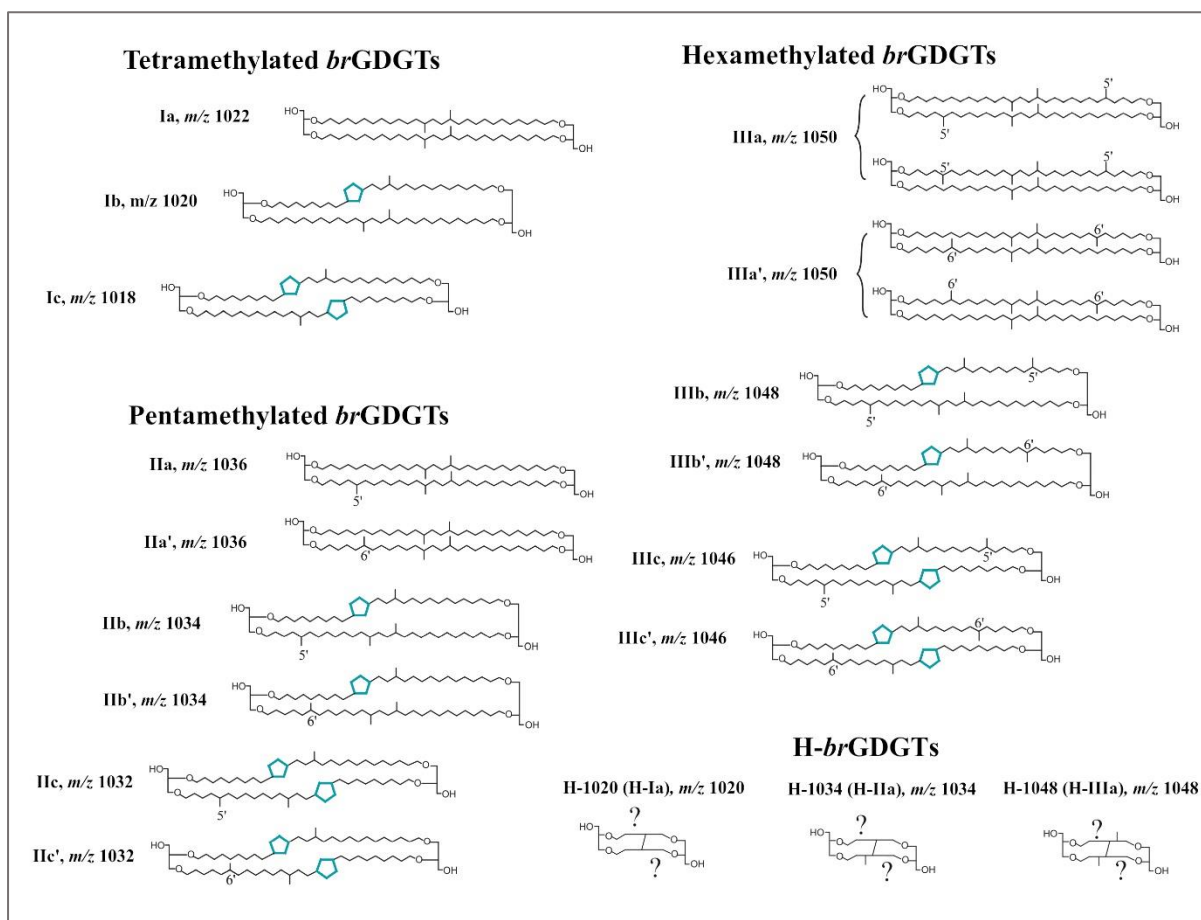


Figure 8. Chemical structure of the best known branched GDGTs, H-*br*GDGTs, and their mass-to-charge ratios (*m/z*). Figure redrawn from Naafs *et al.* 2018.

3.1.4 7-methyl brGDGTs

The considerable scatter observed in the environmental reconstructions using *brGDGTs*-based proxies, along with the discovered adjustment of membrane lipids to different temperature and pH conditions, suggests that additional methylation, cyclization, and isomerization configurations are likely to exist (Ding *et al.* 2016). The identification of 7-methyl *brGDGTs*, as well as structural isomers of the IIb and IIb' *brGDGTs*, were reported by Ding *et al.* (2016), which further complicates the calibration of *brGDGTs*-based proxies. These were identified by a modified HPLC separation combined with fraction collection and analysis of hydrocarbon chains via ether bond cleavage from Chinese and Cameroon lacustrine sediments, comprising about 5 % of the total *brGDGTs*. This indicates that the 7-methyl isomers might be universally distributed, which would mean that they would need to be considered for new *brGDGTs*-based proxy calibrations. However, the 7-methyl isomers were not found in a Siberian peat nor in a soil dataset, which calls for a meticulous re-evaluation of 7-methyl *brGDGTs* in soils and peats (Ding *et al.* 2016). Other potentially important isomers recently identified include 5/6-methyl hexamethylated *brGDGTs*, which can appear as a small peak eluting between their 5- and 6-methyl counterparts (Weber *et al.* 2015).

3.1.5 H-GDGTs

Glycerol monoalkyl glycerol tetraethers (GMGTs), also called H-GDGTs, possess an additional covalent bond (Fig. 8) compared to their dialkyl counterparts, that links the two alkyl chains (Naafs *et al.* 2019). Both H-*isoGDGTs* and H-*brGDGTs* have been identified in the last few years, and although a wider variety of H-*isoGDGTs* have been discovered, H-*brGDGTs* appear to be more abundant in peat sediments (Naafs *et al.* 2019). H-GDGTs can be identified in selected ion monitoring mode, by targeting the protonated molecules at specific *m/z*, appearing as separate peaks in the chromatogram (Naafs *et al.* 2018). In the case of H-*brGDGTs*, these peaks have been identified for *m/z* 1020 (H-Ia), 1034 (H-IIa), and 1048 (H-IIa) (Naafs *et al.* 2018). It has been found that the relative abundance of H-GDGTs compared to non-H-GDGTs is positively, although non-linearly, correlated with temperature (Naafs *et al.* 2019). Even though this correlation is not strong enough to be used as a quantitative proxy, it can be used in a qualitative manner. More research is needed in order to better identify the factors that influence the abundance of H-GDGTs. Naafs *et al.* (2018) defined the H-MBT_{acyclic} index and established that the degree of methylation of H-*brGDGTs* is linearly related to the degree of methylation of regular *brGDGTs*:

$$H - MBT_{acyclic} = \frac{H - brGDGT - Ia}{H - brGDGT - Ia + H - brGDGT - IIa + H - brGDGT - IIIa} \quad (7)$$

The lower abundance of H-GDGTs reported in mesophilic environments, compared to extreme ones, has led to the hypothesis that the additional covalent bond is an adaptation that facilitates membrane permeability at higher temperatures (Naafs *et al.* 2018). This is supported by the fact that higher concentrations of H-GDGTs, both isoprenoidal and branched, have been

found in tropical peats relative to middle- and high-latitude ones (Naafs *et al.* 2019). Knappy *et al.* (2011) speculated that H-*iso*GDGTs are biosynthetically derived from non-H-*iso*GDGTs, which is in agreement with the apparent direct correlation between H-GDGTs and their dialkyl counterparts.

3.2 Sample Preparation

The 6-meter peat core (RP-1A-REPA) was recovered from Danau Padang with a Russian D-corer by a team from the State University of Padang (Indonesia) and the Nanyang Technological University (Singapore). The core was placed in a PVC v-channel and taken to the Department of Geological Sciences of Stockholm University by Petter Hällberg. A total of 60 1-cm samples were taken for lipid analysis, with a resolution of 10 cm (the top one was named P10 and the bottom one P600, etc., after the depths at which they were taken). Additionally, 14 evenly spaced samples were taken for radiocarbon dating, and another 14 samples were retrieved for microscope identification of leaves, pollen, spores, or other remains that could potentially be used for more precise radiocarbon dating. Unfortunately, the latter task was unsuccessful since no useful remains could be identified under the microscope. Radiocarbon and microscope samples were taken from the following depths (cm): 35.5, 64, 95, 145, 185, 225, 266, 305, 345, 386, 414, 494, 535, and 603. All 60 lipid-analysis samples, as well as the 14 bulk radiocarbon samples, were stored in a freezer at -18 °C overnight, and were subsequently freeze-dried for three days using a ScanVac CoolSafe freeze dryer. The process of freeze drying removes the water from the samples through sublimation, allowing the ice to change to gas form directly, skipping the liquid phase. A vacuum pump is necessary to force the water to a collector coil, separating it from the samples. In order for the water to separate from the samples, these must be placed in the vacuum chamber covered in aluminum foil with plucked holes in it, at temperatures colder than -50 °C. After freeze-drying the samples, the 60 samples for lipid analysis were cut into rectangular prisms, they were weighted, and their dimensions were measured for density estimations. Next, all 74 samples were milled with a mortar and pestle and each one was divided into 2 sample 40-ml tubes, one containing about $\frac{3}{4}$ of the sample, and the other one containing the remaining fourth. The former was used for lipid extraction and analysis while the latter was sub-sampled for elemental analysis (EA) and stored in a refrigerated room for possible later analyses. For the EA subsampling, approximately 0.5 mg of the sediment were weighted and packed into tin capsules for solids, using a Mettler Toledo UMT2 analytical balance.

3.3 Lipid Extraction

All 60 samples were extracted using 10-20 ml of a mixture of DCM (dichloromethane) and MeOH (methanol) in a ratio 9:1 (v:v). They were then vortex mixed for a few seconds, and sonicated for 15 minutes without heat. Sonication uses sound waves to mix and agitate the particles in a solution, facilitating the extraction of the different lipids. Subsequently, 4 ml of hexane were added to facilitate separation and sedimentation. Afterwards, the samples were

centrifuged for 10 minutes at 800 rcf (Relative Centrifugal Force, unit of gravity) using an Eppendorf 5810R centrifuge, and were left to settle overnight. The supernatants were removed using glass pipettes and placed into 40-ml sample tubes. Then, the lipid extracts were carefully evaporated under a N₂ blowdown system at 25 °C. The lipid extraction was repeated 2 more times, using 20 ml of the DCM:MeOH 9:1 (v:v) solution the first time, and 15 and 10 ml the second and third times, respectively.

3.4 Fractionation

For the fractionation, empty glass pipettes were used as columns and were packed with pre-combusted and then deactivated silica gel (by the addition of 5 % water), filling approximately half of the column, and using pre-combusted cotton wool as a stopper. Then, less than 1 ml of DCM was added to each of the 60 dried samples and were swirled until dissolution was complete. Afterwards, a sufficient amount of silica gel was added to absorb the sample and the DCM completely, and they were left to dry at 25 °C. Subsequently, the dried samples were scraped down with a spatula and added to the columns. Three different fractions were eluted and collected into vials by using hexane, DCM:MeOH 1:1, and MeOH, respectively. Approximately 3-4 column volumes of each eluent were added, and the eluates were collected into separate vials. Hexane was used for the extraction of non-polar hydrocarbons (Fraction 1 or F1), such as those that comprise the chains of leaf waxes, which can be used as proxies for temperature and plant functional type, among others. The mixture of DCM:MeOH 1:1 was used as the eluent to extract polar molecules, such as sterols and GDGTs (F2). Lastly, MeOH was used to extract levoglucosan (F3), which can be used as a tracer for biomass burning. Nevertheless, the latter fractionation was carried out merely to facilitate future research, and the F3 samples were not analyzed in this thesis project. The samples were then dried out using a N₂-blowdown system at 25 °C.

3.5 Sub-sample Preparation for GC-MS and HPLC-MS Analyses

The F1 samples were prepared for GC-MS (gas chromatography-mass spectrometry) analysis by transferring them to 2-ml GCMS vials using hexane. They were subsequently dried out under N₂ at 25 °C, and later redissolved in 1000 µl of hexane. The samples were analyzed with a Shimadzu GCMS-QP2010 single quadrupole gas chromatograph-mass spectrometer at Department of Geological Sciences of Stockholm University. However, the quantification of these data never took place due to time restrictions, given the limited scope of this thesis work.

To prepare the F3 fraction, 2.00 ml of Hex:IPA (Hexane:Isopropyl Alcohol) 99:1 were added to the dry fraction. The solution was then vortex mixed, and sonicated for 15 minutes without heating. Afterwards, the top 1 ml of each sample was filtered using a syringe connected to a 0.45 micron PTFE filter, and pushed into new 2-ml vials. The bottom 1 ml of the F3 fractions, which contained the infranatant, were dried and kept for future analysis of sterols through GC-MS.

3.6 HPLC-MS Analysis and Quantification

Liquid chromatography-mass spectrometry (LC-MS) is a coupled analytical technique that combines the separation capacity of chromatography with the mass-to-charge analytical capabilities of mass spectrometry. In a chromatography, the different components of interest are separated based on their relative affinity for two immiscible phases (Rouessac & Rouessac 2007). The stationary phase is fixed within the column, while the mobile phase (in this case, the liquid solvents A and B, see below) flows through it. Once separation is achieved, an interface that transfers the separated analytes from the LC column into the mass spectrometer is needed, since the LC and MS systems are incompatible. For the present project, the interface used was atmospheric pressure chemical ionization (APCI), which uses gas-phase ion-molecule reactions at atmospheric pressure to ionize the analytes. Once in the mass spectrometer, the ionized samples are focused and accelerated to increase their kinetic energy, and subsequently subjected to a magnetic or electric field under high vacuum, which deflects their trajectory depending on their mass-to-charge ratio (Rouessac & Rouessac 2007). The results are displayed as a spectrum of mass-to-charge ratios that can be correlated to known masses of familiar molecules or fragment ions, as well as a chromatogram, whose peaks represent the variation with time of the amount of analyte in the mobile phase. Each peak corresponds to one analyte, and the area below each peak represents the concentration of that specific analyte.

The *br*GDGTs and *iso*GDGT-0 were analyzed via high-performance liquid chromatography-atmospheric pressure chemical ionization-mass spectrometry (HPLC-APCI-MS) on a Dionex UltiMate 3000 rapid separation liquid chromatography system (ThermoFisher Scientific) paired with a TSQ Quantum Access Max Triple Quadrupole mass spectrometer (ThermoFisher Scientific) at Stockholm University. Normal phase separation was achieved using two silica Acquity UPLC HILIC columns (2.1 x 150 mm) in tandem, maintained at 30 °C. The HPLC system was operated at a constant flow rate of 0.300 ml/min using hexane (solvent A) and Hex:IPA 9:1 (solvent B). The injection volume was 40,00 µl, and the total run time of each sample was 72 minutes. The initial solvent composition was 82 % A and 18 % B, which was held for 15 minutes, followed by an increase to 35 % B within 20 minutes, and another increment to 100 % also within 20 minutes. B was held at 100 % for 2 and a half minutes and then the eluents were immediately re-equilibrated to 82 % A and 18 % B until the end of the 72-minute run. Analyses were performed using selective ion monitoring mode (SIM) targeting the following ions based on mass/charge ratios: *m/z* 1302, 1050, 1048, 1046, 1036, 1034, 1032, 1022, 1020, and 1018. Triplicate analysis was conducted for samples P10-P150, and duplicate analysis for P160-P600. This was done in order to improve the accuracy of the results (by calculating mean values for each sample), and to estimate the precision of the assay by the calculation of standard deviations and coefficients of variability (sample variation). The resultant chromatograms-spectra were quantified through both a processing method and manual integration, using the Xcalibur software. *Br*GDGTs indices were calculated using the average of the replicated results obtained from each sample. The chromatographic peaks were integrated and quantified according to the integration methods and relative retention times reported in the existing literature (De Jonge *et al.* 2013 & 2014; Ding *et al.* 2016; Hopmans *et al.* 2016; Rattray & Smittenberg 2020).

3.7 Elemental Analysis

The concentrations and isotopic compositions of nitrogen and carbon in different sediment fractions were determined simultaneously using a Flash-EA 1112 Elemental Analyzer (ThermoFisher Scientific) coupled to an isotope ratio mass spectrometer (IRMS, Delta V, ThermoFisher Scientific) at the Geological Institute, ETH Zurich. The analysis was performed by Madalina Jäggi. The system was calibrated with standards of known elemental and isotopic composition. The reproducibility of measurements was better than 0.2 ‰ for both elements. Carbon and nitrogen contents are reported in percent (%) of dry weight. On the other hand, C and N isotope ratios are reported in the conventional delta-notation (δ ‰) relative to Vienna Pee Dee Belemnite (V-PDB) and standard atmospheric air, respectively. The C content is directly related to the amount of organic matter, and can provide information about the ratio of organic to minerogenic content in the sediment (Page *et al.* 2004). The carbon to nitrogen ratio (C/N) can be used as a proxy for biomass and vegetation types (together with $\delta^{13}\text{C}$ and $\delta^{15}\text{N}$) (Cloern *et al.* 2002; Ku *et al.* 2007; Yamoah *et al.* 2021) and for changes in the degree of decomposition (Kaislahti Tillman *et al.* 2010; Hobbie *et al.* 2017). Furthermore, changes in the $\delta^{13}\text{C}$ composition can sometimes reflect temperature changes, where higher $\delta^{13}\text{C}$ values in peatlands might be associated with lower temperatures (Hobbie *et al.* 2017). Additionally, $\delta^{13}\text{C}$ values seem to be affected by changes in water availability, where lower $\delta^{13}\text{C}$ values are a consequence of higher water availability (e.g., precipitation) (Kohn 2010; Russell *et al.* 2014; Amesbury *et al.* 2015), although this relationship remains controversial and should be used carefully (Amesbury *et al.* 2015). Interpreting the C, N, $\delta^{15}\text{N}$, and particularly $\delta^{13}\text{C}$ values of bulk peat sediments is highly complex due to the competing influence of a multitude of factors, some of which are still poorly understood (Eglinton & Eglinton 2008; Diefendorf & Freimuth 2017).

3.8 XRF and Magnetic Susceptibility Analyses

In order to obtain a semiquantitative chemical analysis of the heavier elements in the peat core, x-ray fluorescence (XRF) measurements were taken by the use of a third generation Avaatech XRF core scanner equipped with a Rhodium-Beryllium tube set located at the Earth Observatory of Singapore, Nanyang Technological University. To avoid the contamination and desiccation of the sediment, the core surface was covered with Ultralene foil before scanning. XRF scanning was conducted at a current of 0.75 mA, an exposure time of 10 seconds, a resolution of 2 mm, and electrical potentials of 10 and 30 kV. The following elements were detected: Al, Si, P, S, Cl, K, Ca, Ti, Cr, Mn, Fe, V, Cr, Co, Ni, Cu, Zn, Ga, Br, Rb, Sr, Y, Zr, Pb, and Bi. XRF scanners measure the ionization (removal of electrons) experienced by an atom when it is bombarded with X-rays. The resulting energy emitted (fluorescence) is unique to each chemical element. XRF analyses only provide information about the chemical composition of the outer tens of micrometers of the sample. Variations in the content of light elements (not measured by the XRF scanner), such as C, can result in opposite changes in the counts for heavier elements, such as Ti (Löwemark *et al.* 2011). Therefore, normalizing the data against a conservative element, such as Al, is necessary to minimize the influence of organic matter-content variations in the Ti signal (Löwemark *et al.* 2011). Al was chosen as a

normalizer not only because it is present in most minerals, but also because it is relatively unaffected by weathering, diagenesis, and biological processes (Löwemark *et al.* 2011). The ratio of Ti to Al (Ti/Al) was used to assess variations in the lithogenic component of the sediment, which in turn was used to interpret changes in erosion rates (wind and precipitation regimes) according to Russell *et al.* (2014) and Löwemark *et al.* (2011). A higher input of minerogenic material, from increased wind or precipitation, should lead to higher Al/Ti values, and should also be reflected in the density and magnetic susceptibility measurements (Xiao *et al.* 2017). Magnetic susceptibility measurements were taken at 4 mm resolution using a magnetic susceptibility meter mounted to an XRF scanner, by Caroline Bouvet de la Maisonneuve and her team, at the Nanyang Technological University, Singapore. This scanner measures the amount of magnetization experienced by the sediment when exposed to a magnetic field. Unfortunately, it was not possible to obtain the specifics about the XRF measurements (e.g., equipment brand, etc.)

3.9 Chronology

From the 14 radiocarbon samples taken, only 8 were analyzed (Table 2). First, to remove inorganic carbon species, the samples were placed in pre-combusted Ag cups, and were fumigated with hydrochloric acid (HCl 37 %) in a desiccator at a temperature of 60 °C for 72 hours. Samples were subsequently neutralized and dried over NaOH pellets (60 °C, 72 h) and wrapped in Sn capsules to help combustion. The radiocarbon (^{14}C) analysis was then performed using a coupled elemental analyzer-accelerator mass spectrometer system (EA: vario MICRO cube, Elementar; AMS: Mini Carbon Dating System MICADAS, IonPlus) at the Laboratory of Ion Beam Physics at the Swiss Federal Institute of Technology (ETH), Zürich. Radiocarbon data are reported as $\Delta^{14}\text{C}$ values (‰), according to the notation proposed by Stuiver & Polach (1977). The lithology and age-depth model were produced with the OxCal software (v.4.4.2) using the deposition model P-sequence ($k=0.2\text{ cm}^{-1}$) (Bronk Ramsey 2008) and the Southern Hemisphere calibration curve (Hogg *et al.* 2020). The results were expressed in calibrated years before 1950 (cal yr BP). C Accumulation rates were calculated from the vertical peat accretion rates and the bulk density measurements of the peat (according to Page *et al.* 2004).

4. Results

4.1 Core Description and Chronology

A total of 603 centimeters of sediment were recovered from Danau Padang (core RP-1A-REPA), all of it consisting of highly homogenous and unstratified peat of black-brown color. The entire section is relatively highly humified with little recognizable plant remains, with the exception of some woody material that was identified as roots, which are more abundant in the top 1 meter of sediment.

The depth-age model (Fig. 9a & Table 2) indicates that the bottom sediment, at 603 cm deep, has an age of 7,826.4 years (cal BP). The model returns a mean rate of vertical peat accretion of 0.77 mm/yr, with higher rates ($\sim 1\text{ mm/yr}$) between 6,942.5 and 3,451.8 cal yr BP,

average rates from the bottom of the core to 6,942.5 cal yr BP, and lower rates (~ 0.5 mm/yr) between 3451.8 cal yr BP and the present (Fig. 9b).

Table 2. EA-AMS Radiocarbon dates from peat core RP-1A-REPA, Danau Padang, Sumatra, Indonesia

Sample Name	Depth (cm)	ETH nr.	Radiocarbon Age (yr BP)	1 Sigma Error (yr)
P35.5	35.5	114658.1.1	1,028	50
P95	95	114659.1.1	1,801	56
P185	185	114656.1.1	3,477	56
P266	266	114652.1.1	3,814	61
P345	345	114657.1.1	4,481	62
P414	414	114655.1.1	5,105	64
P535	535	114653.1.1	5,912	64
P603	603	114654.1.1	7,051	70

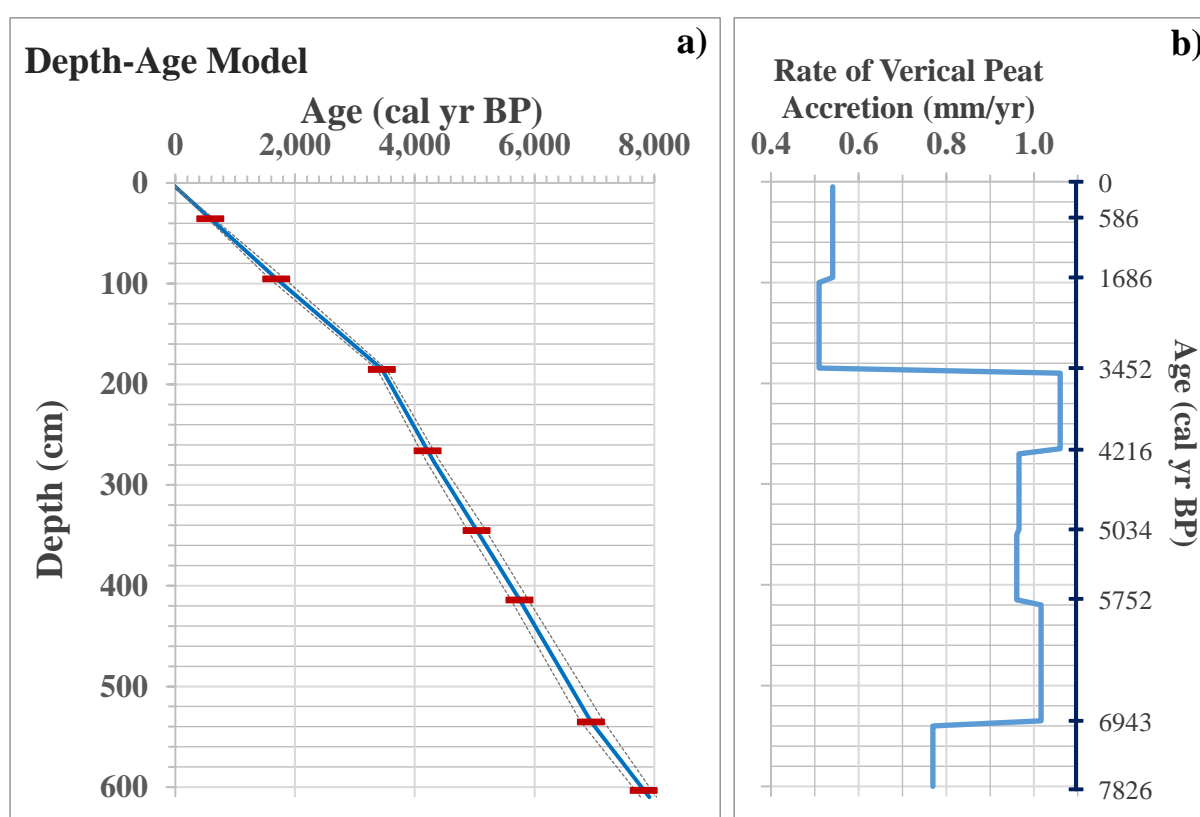


Figure 9. a) Depth-age model and, b) Rate of vertical peat accretion, for peat core RP-1A-REPA, Danau Padang, Sumatra, Indonesia. The blue line in the depth-age model represents the mean age for a given depth, while the gray dotted lines represent the 95 % confidence interval. The red markers are the radiocarbon samples. Rates of vertical peat accretion were calculated from the depth-age model.

4.2 GDGTs and Derived Indices

Firstly, after studying the resultant mass spectra, it was observed that the MS equipment was out of calibration by $-0.5 m/z$, which was later corrected during the quantification. Furthermore, shifts in retention times were observed in the chromatograms the first and second times the samples were run on the LC-MS. Retention times were shown to increase by about 2

seconds between samples P10 and P20 (10 and 20 cm deep, respectively) during the first run, and by about 4 seconds during the second run. An additional increment in retention times of approximately 1.5-2 seconds (first run) was observed between samples P220 and P250, which was then maintained until the end of the sequence (P600). This trend was also observed during the second run, but on this occasion the retention times had incremented only by ~ 0.5-1 seconds. This hindered the creation of a method for peak integration, which led to the manual integration of the majority of peaks. The following *br*GDGTs were identified and quantified: Ia, Ib, Ic, IIa, IIb, IIc, IIIa, IIIa', IIIb'; as well as the isoprenoidal GDGT-0. The correct identification of peaks was easily achieved in the case of the tetramethylated *br*GDGTs and *iso*GDGT-0. This proved to be more intricate for the penta- and hexamethylated, due to the incomplete separation of certain isomers (coelution), the presence of chromatographic peaks representing unknown isomers, and the absence of specific peaks. The peaks associated with the abundances of IIa and IIa' were difficult to integrate. However, re-analysis at slower flow rates (0.200 ml/min) and the comparison with a peat core from Danau Diatas (core Diatas 1A, ~ 100 km southeast of Danau Padang, analyzed using the same methods and equipment, by Petter Hällberg at Stockholm University) led to the conclusion that there were negligible concentrations of IIa' in all the samples, which had probably coeluted with IIa (Fig. 10). Given the low relative abundance of IIb (< 0,6 % of the *br*GDGTs, Fig. 12 & A1), peak integration was difficult due to abundant background chromatographic noise, but after using the same method as for IIa and IIa' (Fig. 10), it was determined that IIb' would not be integrated. The reason was that what appeared to be IIb' was too close to background noise in the majority of samples. Moreover, a single distinctive peak was found for *m/z* 1034 (within relevant retention times) and it was regarded as IIc, by comparing it with the relative retention times reported by De Jonge *et al.* (2014). They described virtually identical retention times for Ia and IIc. Furthermore, IIIa and IIIa' were integrated according to Ding *et al.* (2016) and De Jonge *et al.* (2014) (Fig. 11 & E1). Only one peak was found for *m/z* 1048 within relevant retention times, which was concluded to represent the abundance of IIIb', since its retention time should be slightly shorter than that of IIa (De Jonge *et al.* 2014). Finally, it was impossible to discern IIIc or IIIc', because of their low relative abundances, which impeded their differentiation from background noise. The complete quantified results can be found in Appendix A.

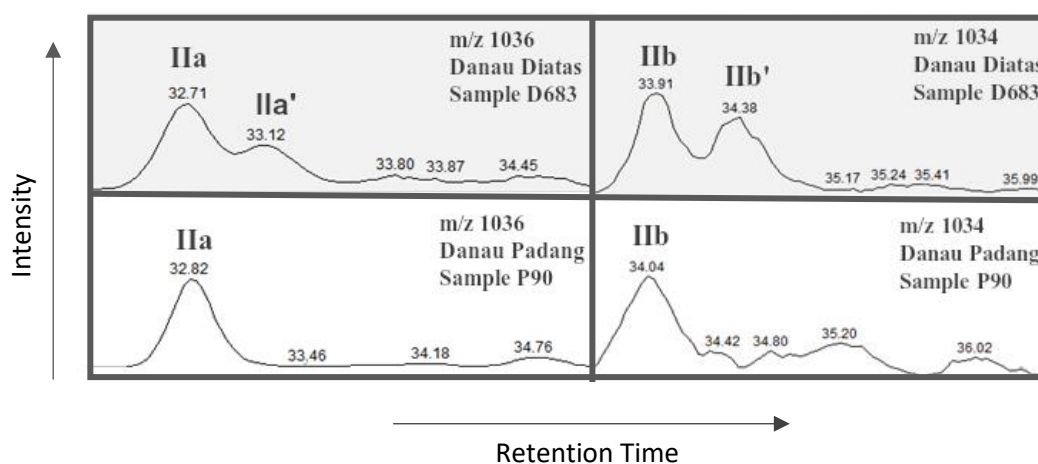


Figure 10. Comparison between the chromatograms of peat cores from Danau Padang (RP-IA-REPA) and Danau Diatas after re-analysis conducted at 0.200 ml/min for *m/z* 1036 and 1034. IIa' and IIb' could not be identified in the Danau Padang record.

All three known H-*br*GDGTs were successfully identified in the entire sequence of samples: H-1020 (H-Ia), H-1034 (H-IIa), H-1048 (H-IIIa) (Fig. 11 & Table A9). These were quantified by Petter Hällberg at the Department of Geological Sciences of Stockholm University. Additionally, multiple isomers (non-5- or 6-methyl) of *br*GDGTs were found, particularly (but not exclusively) for *m/z* 1050 and 1036 (Fig. 11). Some of these are thought to correspond to 5/6- and 7-methyl isomers (Ding *et al.* 2016). They appear as separate peaks with incomplete baseline separation.

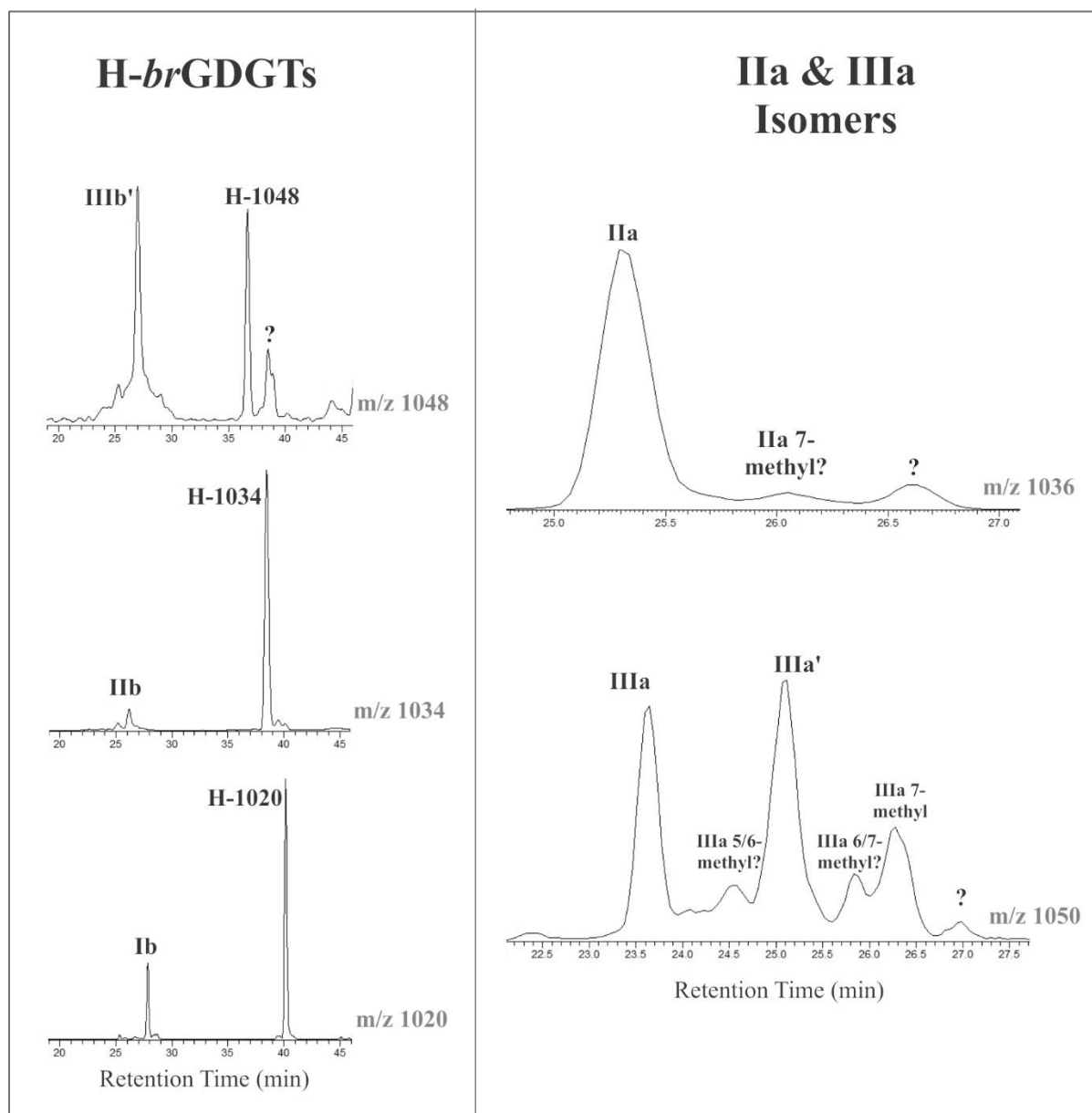


Figure 11. Chromatographic identification of H-*br*GDGTs and IIa- and IIIa-*br*GDGT isomers from sample P260 of peat core RP-1A-REPA (Danau Padang).

The results from analytical replication were all very comparable (Fig. 13 & Appendix A). In this thesis work, the results discussed refer to the calculated mean averages from the

duplicate and triplicate analyses, unless stated otherwise. Sample P530 could not be quantified the second time it was analyzed, due to an abnormally noisy chromatogram. Furthermore, it is also important to mention that the top sample (P10) yielded noisier chromatograms than the rest, with higher coefficients of variation, suggesting a lower degree of precision.

The results showed that most of the *brGDGTs* were tetramethylated (86.628 %), followed by pentamethylated (11.620 %), with hexamethylated *brGDGTs* comprising only the remaining 1.753 %. Tropical peats contain almost exclusively *brGDGT-Ia* (Naafs *et al.* 2017a), so it was unsurprising to learn that the overwhelming majority (83.217 %) of *brGDGTs* analyzed in core RP-1A-REPA (Danau Padang) were indeed Ia (Fig. 12, A1 & Table A8). The second most abundant *brGDGT* was IIa (11.406 %), followed by Ib (2.058 %), Ic (1.353 %) and IIIa' (1.006 %). The relative abundances of the rest of the quantified *brGDGTs* were below 1 %. Moreover, among the penta- and hexamethylated *brGDGTs*, 5-methyl-*brGDGTs* were found in higher abundances than their 6-methyl counterparts, which is in accordance with the

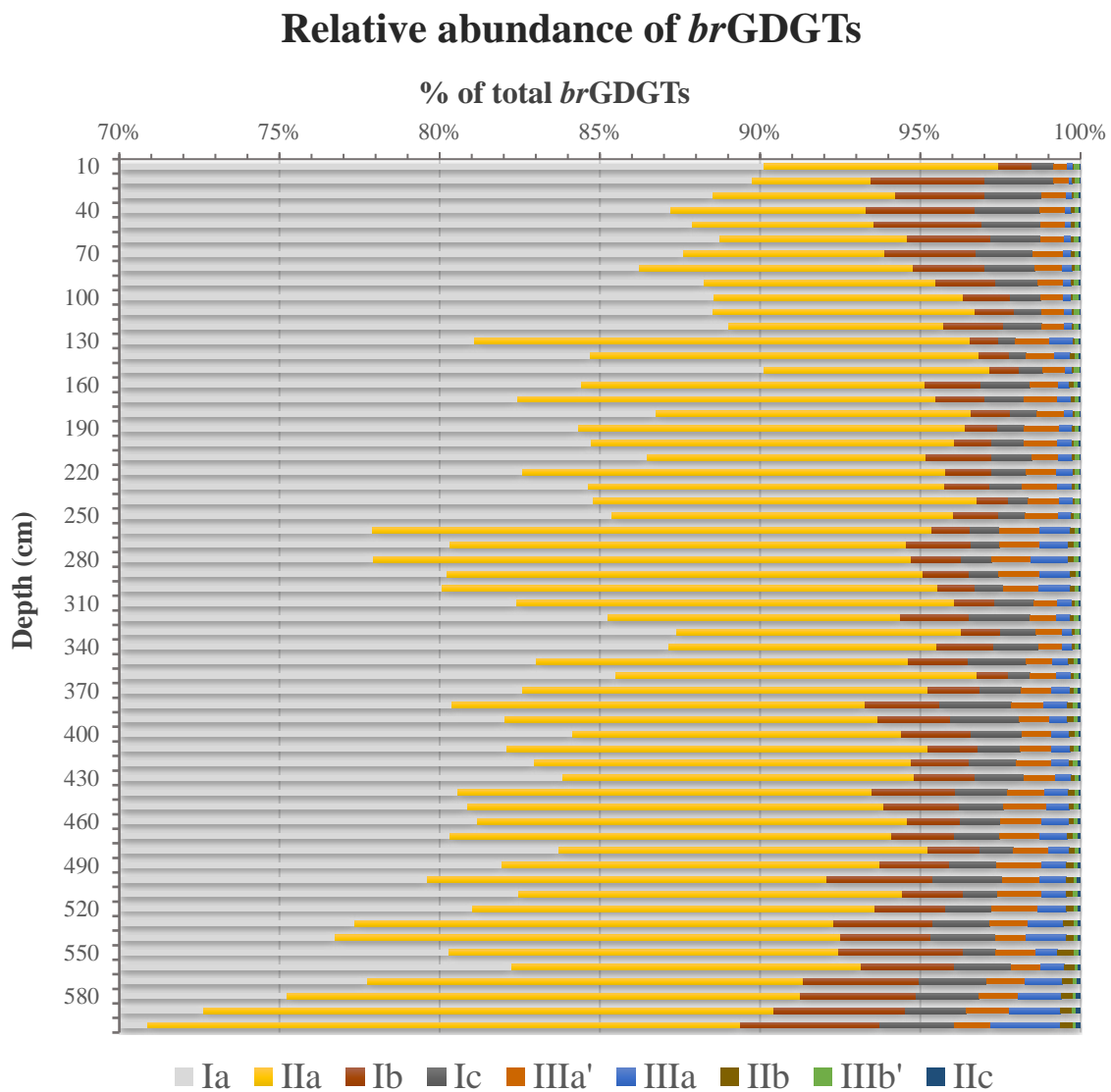


Figure 12. *BrGDGT* distribution with depth in peat core RP-1A-REPA, from Danau Padang, Sumatra. The relative abundance of *brGDGTs-Ia* is greater than 70 % in all samples.

existing records (Naafs *et al.* 2017a; De Jonge *et al.* 2014). Ia and IIIb' became scarcer with depth, whereas the remaining (quantified) *brGDGTs* showed the opposite trend.

The MBT'_{5ME} , CBT_{peat} , IR_{6ME} and IBT indices (Equations 1, 3, 5, and 6, respectively), as well as the ratio of *isoGDGT-0* to *brGDGTs* (%) were calculated both using the individual results yielded from the duplicate and triplicate analyses, and using their averages for each sample (Fig. 13, 14 & Tables A4-A7). The coefficients of variation (CV) between the different replicate analyses proved to be small, indicating high analytical precision. The mean CV for the MBT'_{5ME} index was only 0.007 %, while those for the CBT index and the ratio of *isoGDGT-0* to *brGDGTs* were 0.027 and 14.242 %, respectively. In spite of the larger scatter observed in the CV of the latter, the total standard deviation only accounts for 1.5 % of the total *isoGDGT-0* to *brGDGTs* ratio (%).

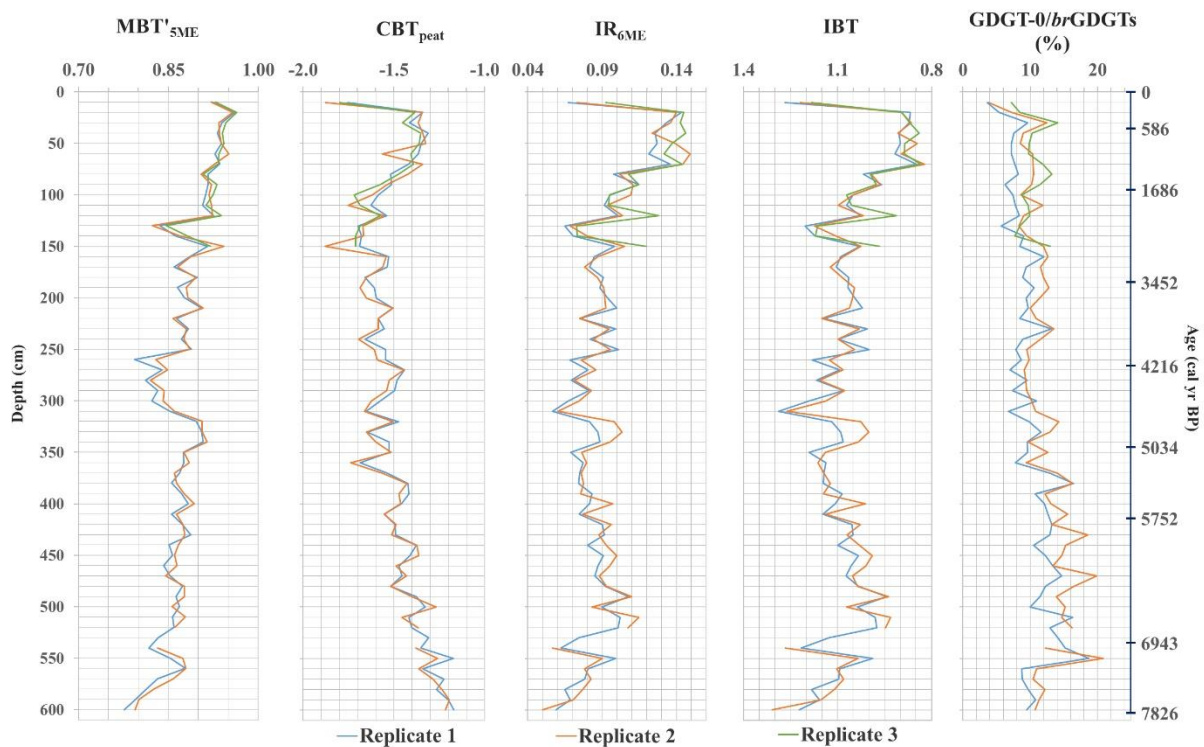


Figure 13. Comparison between the different replicate analyses applied to GDGT-derived indices for peat core RP-1A-REPA, from Danau Padang, Sumatra. The results from the first, second and third analyses (replicated) are represented by blue, orange, and green lines, respectively. The MBT'_{5me} , CBT_{peat} , IR_{6me} , and IBT indices were calculated according to De Jonge *et al.* 2014, Naafs *et al.* 2017a, Yang *et al.* 2015, and Ding *et al.* 2015, respectively.

The resultant MBT'_{5ME} index values decrease with depth (Fig. 14 & Table A4), indicating cooler MAATs in the past. The opposite trend was found for the CBT_{peat} index (Table A5), suggesting an increment in pH with increasing depth. The IR_{6ME} and IBT indices, which are commonly used as qualitative pH indicators, match the CBT trend relatively well from the top of the profile to 500 cm deep. Nevertheless, below that depth, unlike the CBT, the IR_{6ME} and IBT display a shift toward what would be interpreted as lower pH values.

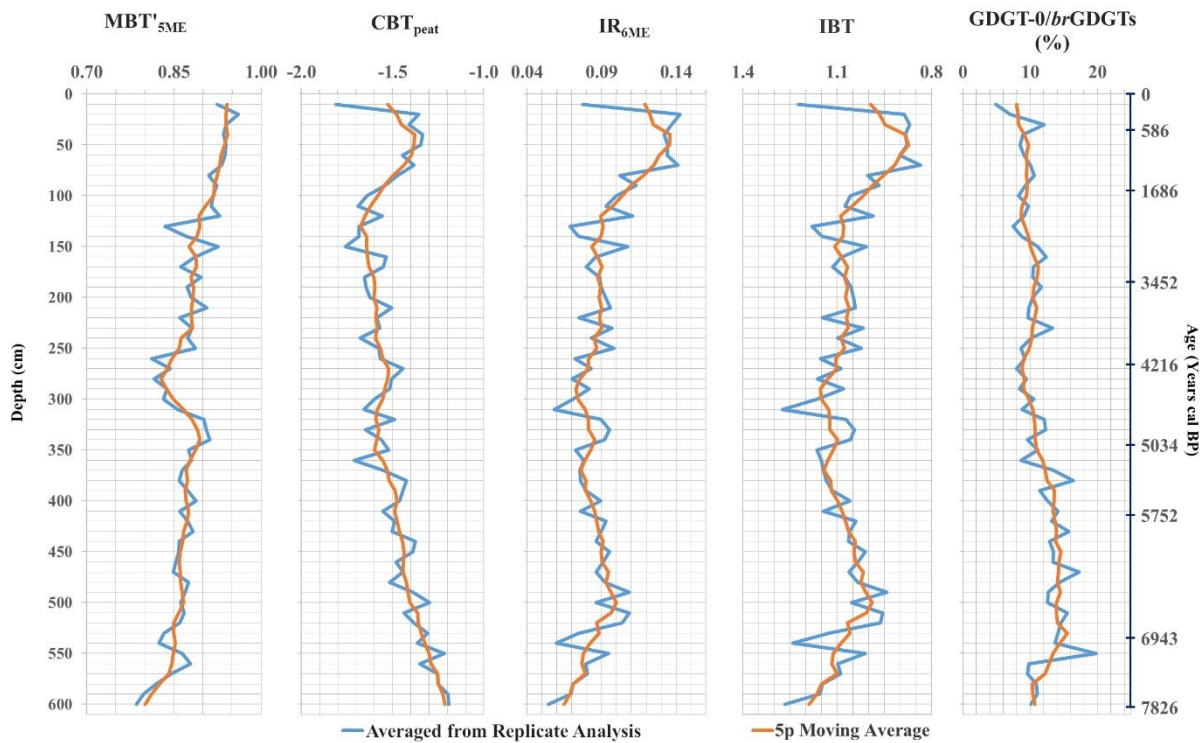


Figure 14. Different GDGT-derived indices for peat core RP-1A-REPA, from Danau Padang, Sumatra. The results were averaged from the replicate analyses. The MBT'_{5me} , CBT_{peat} , IR_{6me} , and IBT indices were calculated according to De Jonge et al. 2014, Naafs et al. 2017a, Yang et al. 2015, and Ding et al. 2015, respectively.

Peat-specific temperature and pH calibrations were calculated using Equations 2 and 4. The results show the highest temperature (27.08 °C) at a depth of 20 cm, whereas the lowest temperature (17.93 °C) was recorded at the bottom of the peat profile (Fig. 15). Two considerable troughs can be observed at 130 cm and especially between 250 and 320 cm deep, indicating relatively abrupt temperature drops, reaching 20.52 and 19.3 °C, respectively. On the other hand, as it is expected in peat, pH values remain on the acidic side for the entire profile, with the lowest pH (3.56) recorded at the very top sample, followed by a sharp increase (to about 4.7) from 20 to 70 cm deep, and a rapid shift toward more acidic conditions (pH 3.69) in the succeeding 80 cm of sediment. After that, from a depth of 160 cm until the bottom of the record, the general trend is toward higher pH values, peaking at a value of 5.1.

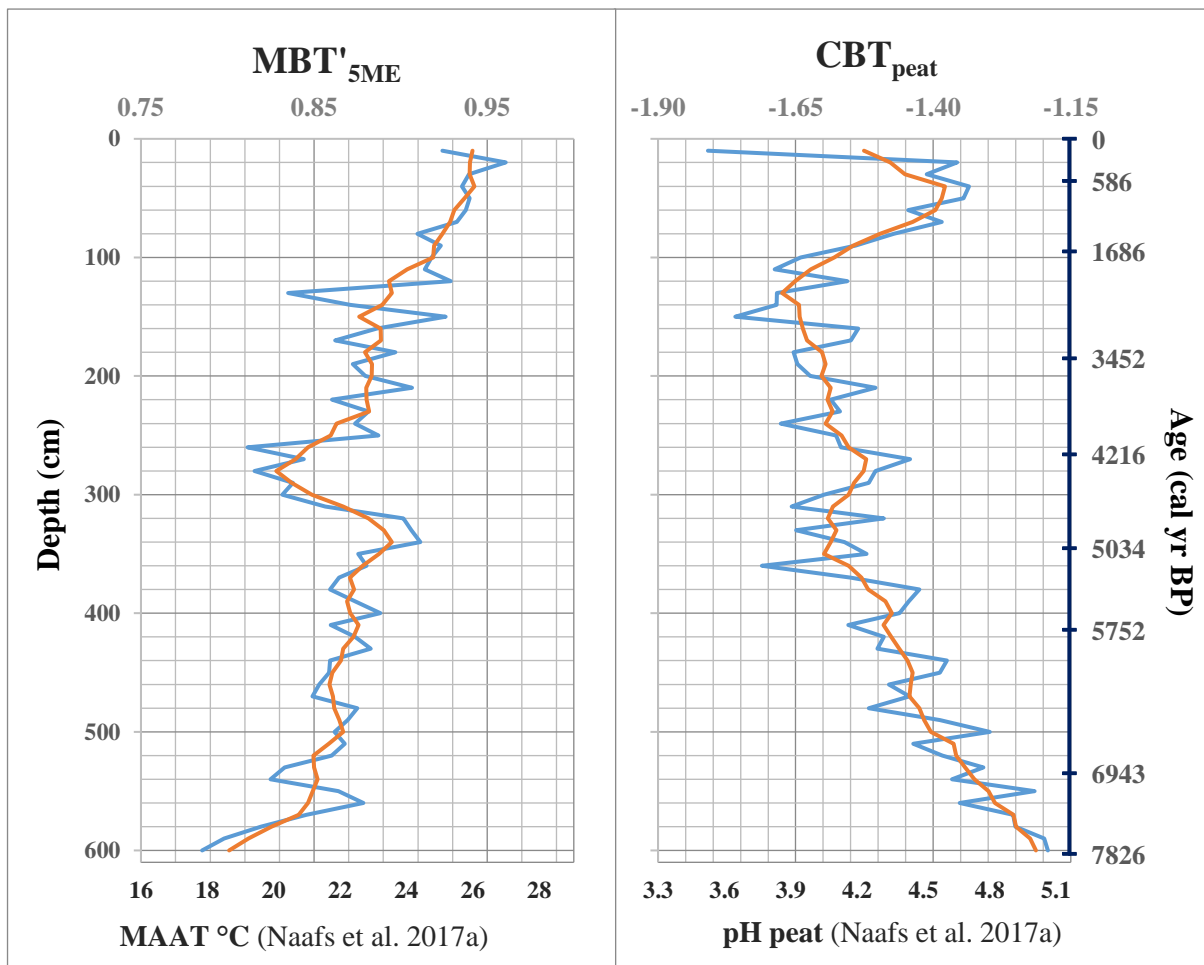


Figure 15. Mean annual atmospheric temperature and pH reconstructions from peat core RP-1A-REPA, Danau Padang, Sumatra. Calibrations from Naafs et al. 2017a.

4.3 Elemental Analysis (C, N, and their isotopes)

The elemental analysis showed that the mean carbon and nitrogen contents (dry weight) from the 60 samples are 53.9 and 1.1 %, respectively (Fig. 16 & B1). The carbon content remains relatively constant throughout the core, ranging between 43.3 and 55.41 %. The only anomaly is found at depths between 260 and 320 cm, where a sudden shift toward the lowest values is observed. Nitrogen contents remain between 0.6 and 1.8 % for the entire peat record, peaking at the top (1.8 %) and bottom (1.5 %) sections and showing two large troughs (0.7 and 0.6 %) at depths of 360 and 550 cm, respectively. C/N increments down the profile, where increasingly larger spikes were measured at 130, 360, and 550 cm deep, the latter of which peaks at a value of 98.6. This is followed by a sharp decrease to values below 40 in the bottom 40 cm of the record.

Carbon isotope ($\delta^{13}\text{C}$) values remain relatively constant throughout the profile, ranging from -27.54 to -29.78 ‰ at 130 and 420 cm deep, respectively (Fig. 16 & B1). Other significant enrichments are observed at depths of 290-310 (> -28.2 ‰), 490 (-28.08 ‰), and 560 (-28.45 ‰) cm, while additional depletions were recorded at 150 and 510-540 cm deep, showing values

of -29.3 and < -29.67 ‰, respectively. Nitrogen isotope ($\delta^{15}\text{N}$) values shift from roughly 0 ‰ at the top of the profile, to -3.92 ‰ at 180 cm deep, followed by a drift toward more positive values, peaking at a depth of 560 cm with almost 1.79 ‰. Within the latter trend, two large ^{15}N -depletion sections were recorded, with troughs at 310, 420, and 550 cm.

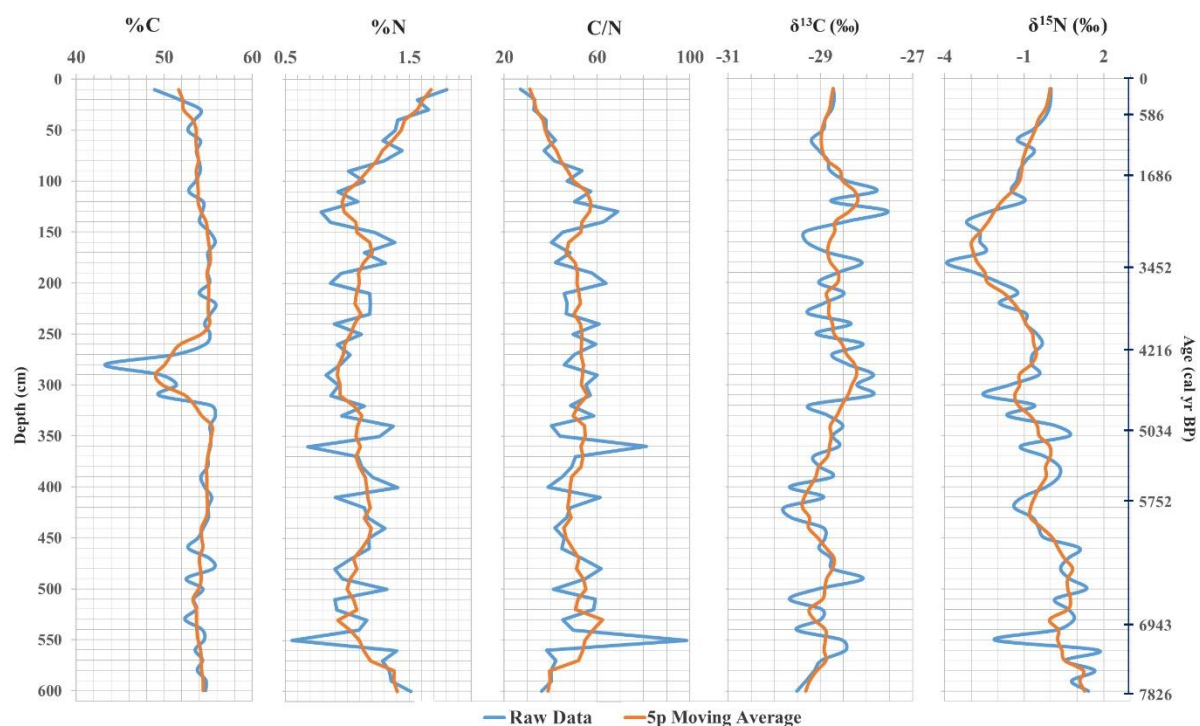


Figure 16. Carbon and nitrogen elemental and isotopic abundances in peat core RP-1A-REPA, Danau Padang, Sumatra. C and N content is expressed in % of dry weight. Their isotopic compositions are reported in the conventional delta-notation (δ ‰) relative to Vienna Pee Dee Belemnite (V-PDB) and standard atmospheric air, respectively.

4.4 XRF and Magnetic Susceptibility

Unfortunately, many of the XRF-scanner measurements display noticeable alignment errors, which were attributed to differences in the measurement dates (Fig. C1). This was particularly true for the Si record, hence it could not be used for normalization. Fortunately, the Ti measurements (at 30kV) appear to be consistent, and the Al record shows only one mismatch (90.2-168.8 cm deep). This error was corrected by calculating the difference between the average value of the twenty measurements (out of 3030) preceding and succeeding the mismatch (204.19 cps), and the mean value of the misaligned section itself (-389.77 cps). This difference (593.96 cps) was in turn added to each of the values of the mismatched section, which produced a more coherent record (Fig. C1). Thus, Al was the element chosen to for Ti-normalization (Ti/Al). Moreover, to minimize high-amplitude variability in order to facilitate the identification of trends, the $\log(\text{Ti}/\text{Al})$ was plotted against depth and age, as well as the 9-point moving average (Fig. 17 & C2). This curve was used to assess variations in the minerogenic component of the sediment. The general trend was a decrease in Ti/Al with

increasing depth, but large inputs were recorded at depths of roughly 170-200 cm, 265-305 cm, 490-498 cm, and 530-534 cm, the second of which is particularly notorious, both in terms of amplitude and length.

The magnetic susceptibility results show an average value of approximately -2.3, with the highest values (-1.2) being measured between 216.4 and 232.4 cm deep, and the lowest ones (-6.2) recorded at a depth of 536 cm (Fig 17). Three measurements (259.6, 365.6, and 541.2 cm deep), were removed from the record since they were identified as anomalous, given the fact that they were isolated and displayed abnormally high values.

4.5 Bulk Density and Carbon Accumulation Rates

It is important to note that the accuracy of some of the density measurements is less than ideal, given that when cutting the freeze-dried samples into rectangular prisms, they tended to crumble. This made it impossible to take measurements for three of the 60 samples (P240, P260, and P460), and hindered the precision of some others (Appendix D). Bulk density measurements show values that range from almost 0.2 to less than 0.1 g/cm³. This whole range can be observed in the top 110 cm of the profile, where the highest values were measured (10 cm deep) followed by a trend toward the lowest values. The remaining measurements are characterized by relatively high-amplitude variability, with notable peaks at depths of 200, 290, 390, and 550 cm. Notable troughs were calculated at 190, 270, 360, 490, 540, and 580 cm.

Carbon accumulation rates were calculated from the carbon content, the rate of vertical peat accretion, and the bulk density (according to Page *et al.* 2004). The results illustrate relatively slow (<50 g m⁻² yr⁻¹) carbon accumulation for the top 185 cm of the peat profile troughing at 110 cm deep with < 25 g m⁻² yr⁻¹ (Fig. 17 & Appendix D). This is followed by a large and abrupt shift toward faster accumulation rates that surpass 95 g m⁻² yr⁻¹ at a depth of 200 cm. These higher rates were maintained until the bottom end of the core, with particularly high C accumulation having taken place between 185 and 260 cm deep, and from 420 to 490 cm.

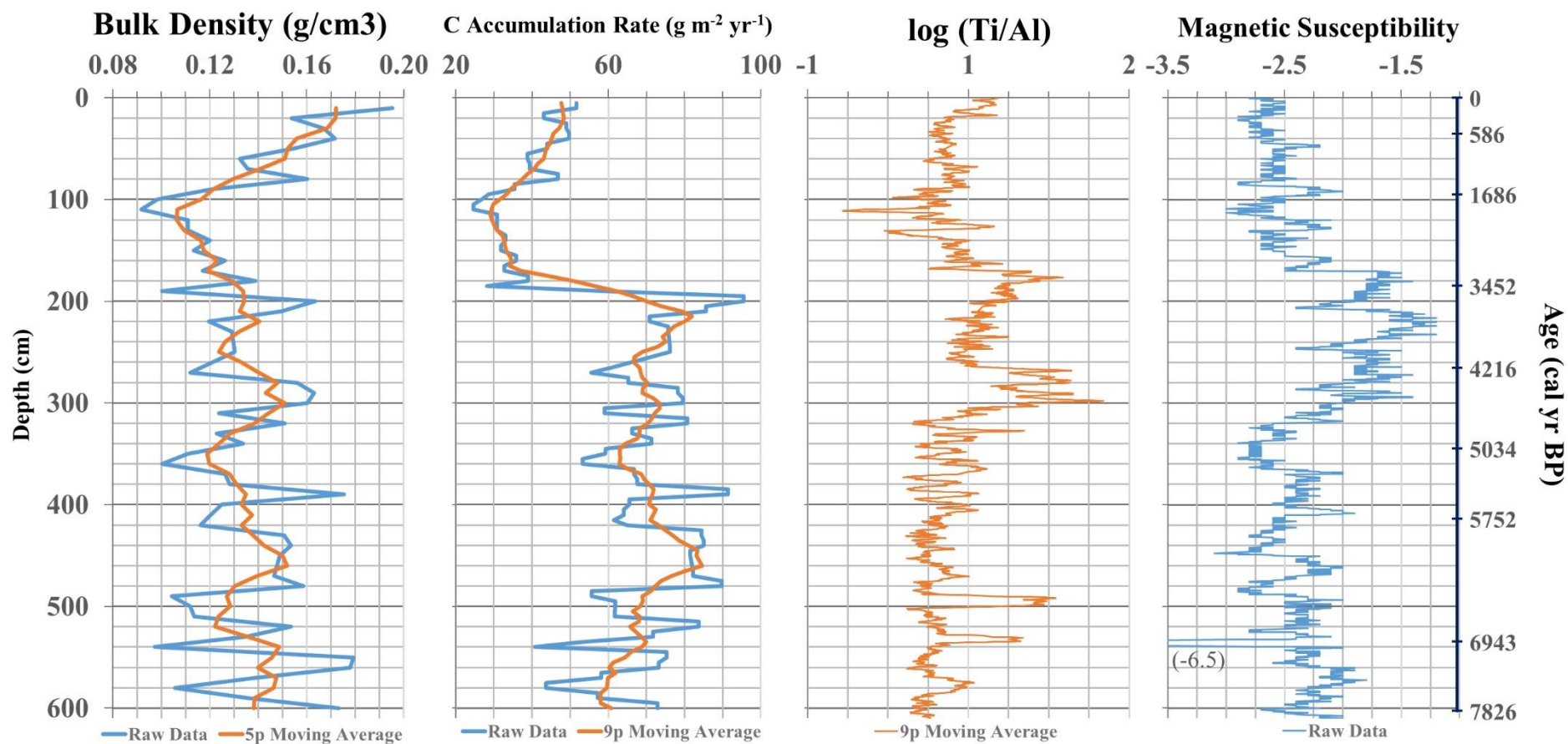


Figure 17. Bulk density measurements, carbon accumulation rates, $\log (Ti/Al)$, and magnetic susceptibility records for peat core RP-1A-REPA, Danau Padang, Sumatra. The bulk density, C accumulation rate, $\log (Ti/Al)$, and magnetic susceptibility records have 60, 120, 3030, and 1525 data points, respectively. C accumulation rates were calculated according to Page et al. 2004. Raw Ti and Al data can be found in Appendix C.

5. Discussion

5.1 *BrGDGTs*

Variations in the MBT'_{5ME} index are mostly dependent on the relative abundances of *brGDGTs* without cyclopentane moieties (Ia, IIa, IIIa), since their abundance curves match almost exactly the MBT'_{5ME} trend (Fig. A1). The recorded decrease in temperature with increasing depth is mainly attributed to a decline in the relative abundance of Ia with depth accompanied by a simultaneous increment in IIa, which are also the two most abundant *brGDGTs* throughout the entire peat profile. On the other hand, variations in the CBT_{peat} index appear to be driven mostly by changes in the relative abundance of Ib (Fig. A1).

5.2 *Temperature Reconstruction*

Most climate models and paleotemperature records show relatively small temperature variability over the last 8 kyr of the Holocene: up to 4 °C at high latitudes and less than 2 °C at low latitudes (Kaufman *et al.* 2020b). Although terrestrial records show a wider range of variability compared to SST records, in most cases this range does not surpass 3 °C (Kaufman *et al.* 2020a). In contrast, the temperatures derived from the Naafs *et al.* (2017a) peat-specific calibration for core RP-1A-REPA (Danau Padang) show a total fluctuation of over 9 °C. This is most likely an overly wide range that does not represent the actual temperatures that took place at this location since the mid-late Holocene. The first possible explanation for this broad temperature range could be that the quantification of the different *brGDGTs* was not performed correctly. However, each of the steps of the geochemical sample preparations were conducted in arbitrary order, to ensure the absence of biases caused by potential differences in the conditions of execution of each step (e.g., human error), which in turn could result in apparent but non-existing trends. The resultant *brGDGTs* indices show coherent trends and a relatively high level of consistency between adjacent samples. Besides, other indices such as the CBT_{peat} show values that match those expected for a tropical peatland (Naafs *et al.* 2017a), suggesting a relatively accurate quantification of at least those *brGDGTs* involved in the CBT_{peat} index (Equation 3). This leads to a possible second explanation, which is that the chromatographic peak integration of at least some of the *brGDGTs* was done incorrectly. It is unlikely that the error could come from the actual analysis of *brGDGTs*, since all the samples were analyzed a minimum of two times, producing very comparable results with very low CVs (Fig. 13 & Appendix A). The possibility that the peak integration could have been done inaccurately is plausible given its complexity (incomplete separation, coelution, and abundance of different isomers) added to a general lack of precise consensus on how to integrate them correctly. To test this possibility, different possible integrations were performed for those *brGDGTs* whose integration was dubious and whose incorrect integration could significantly affect the values of the MBT'_{5ME} index. The integration of the tetramethylated *brGDGTs* was unequivocal, and from the penta- and hexamethylated ones, peaks large enough to influence the MBT'_{5ME} index were only produced for m/z 1036 (IIa and IIa') and m/z 1050 (IIIa and IIIa'). Given that the peak for IIa' most likely coeluted with IIa (Fig. 10), and since the former must have been considerably smaller (as it did not produce any 'shoulder' peaks in the chromatogram), it is

difficult to estimate the peak area that corresponds to Ila'. Therefore, an alternative integration of Ila was performed, this time with a longer tail (Appendix E). Moreover, there is a great number of different peaks produced for m/z 1050 (Fig. 11), and for the majority of the profile, the first-occurring large peak (integrated as IIIa) is smaller in size than the second-occurring large peak (integrated as IIIa') (Fig. 11). Thus, there is a slight chance that the peak integrated as IIIa' could be in fact IIIa. Thus, the MBT'_{5ME} and CBT_{peat} indices were re-calculated using all four combinations of possible integrations for Ila and IIIa (Appendix E). The results (Fig. 18) show extremely similar values for all combinations, with an average CV of less than 0.5 %, which is equivalent to a standard deviation of roughly ± 0.2 °C if the calibration proposed by Naafs *et al.* (2017a) is applied. Hence, imprecisions in the integration of *brGDGTs* do not seem to be responsible for the wide range of temperatures recorded in the peat profile. This is further supported by the strong correlation between the MBT'_{5ME} and the $H-MBT_{acyclic}$ indices (Fig. 19), even more so considering that the integration of *H-brGDGTs* was quite unequivocal.

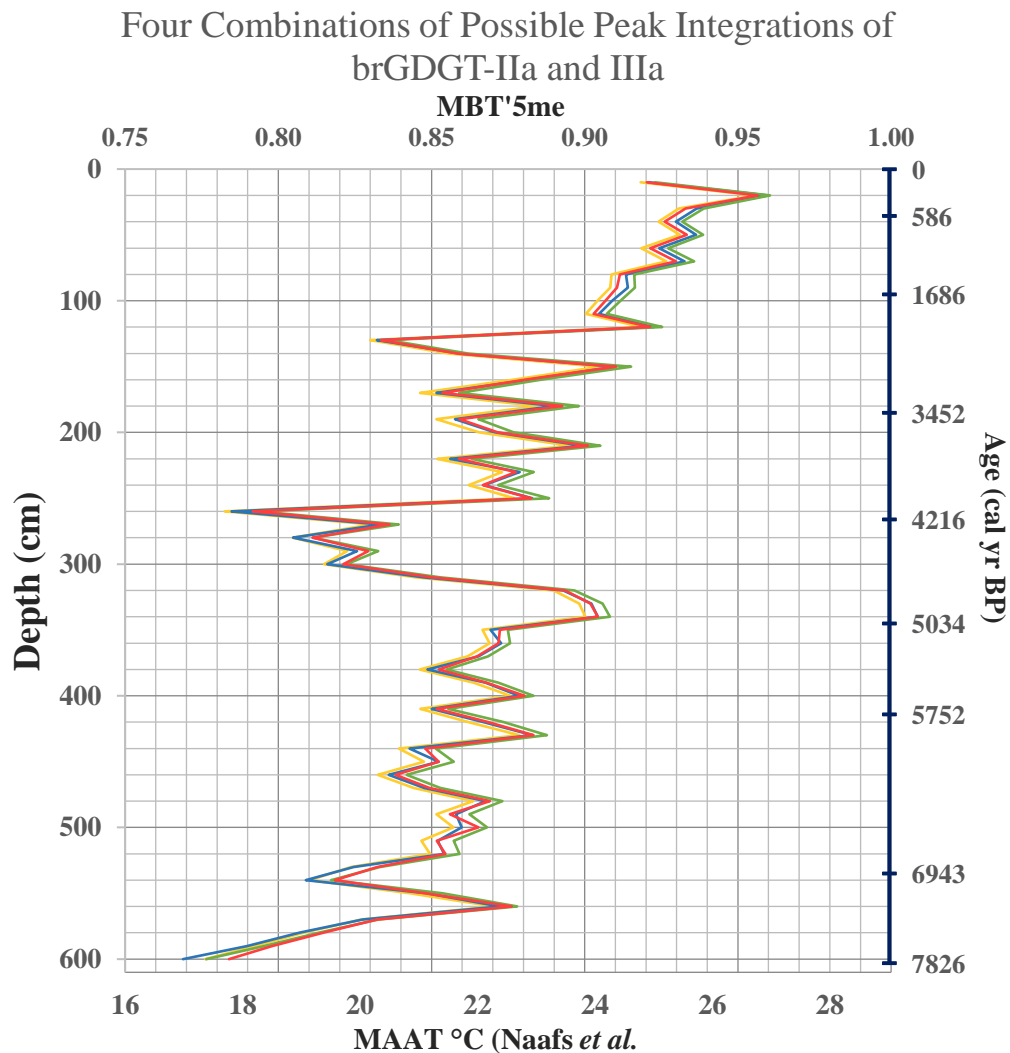


Figure 18. MBT'_{5me} index (De Jonge *et al.* 2014) and MAAT °C (Naafs *et al.* 2017a) calculated from four combinations of possible peak integrations of *brGDGTs*-Ila and -IIIa, from peat core RP-1A-REPA, Danau Padang, Sumatra. The yellow, red, blue, and green curves respectively represent the results when Ila (1) and IIIa (1), Ila (2) and IIIa (1), Ila (1) and IIIa (2), and Ila (2) IIIa (2) are used (see Appendix E for reference).

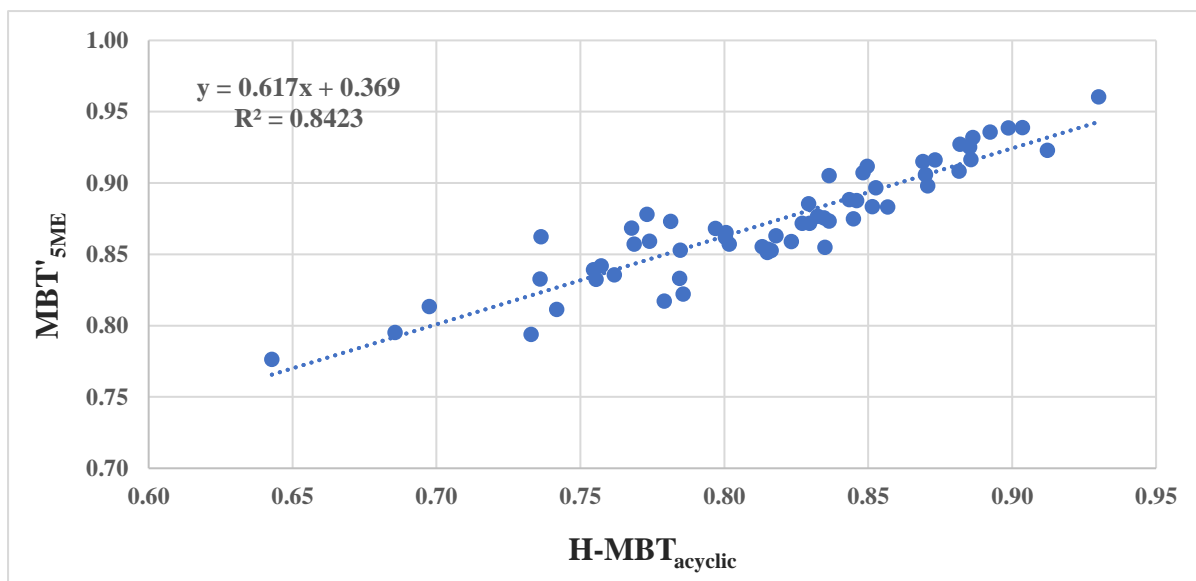


Figure 19. MBT'_{5ME} index (De Jonge *et al.* 2014) plotted against H-MBT_{acyclic} index (Naafs *et al.* 2018) for peat core RP-1A-REPA, Danau Padang, Sumatra. The plotted data shows a very strong correlation between the two indices.

The correlation between the distribution of *brGDGTs* and temperature appears to be different in lakes compared to peat (Naafs *et al.* 2019). This is probably because unlike in peat, *brGDGTs* are thought to be produced under aerobic conditions in lakes. Thus, if a lithological boundary between peat and lake sediments were not correctly identified, it could lead to wrong temperature reconstructions. This could be particularly dangerous in the case of core RP-1A-REPA, given that it was obtained from the edge of Lake Padang. Nevertheless, that does not seem to be the case here since the entire profile was confidently identified as peat.

It is also important to mention that the MBT'_{5ME} temperature proxy is sensitive to changes in peat type and its trophic status (Weijers *et al.* 2011). Moreover, there might be a seasonal bias (Schouten *et al.* 2013), as it has been found that high latitude- and/or high-altitude peatlands can record temperatures that differ from the MAAT due to insulation by snow cover during winter, or high solar irradiance during summer (Naafs *et al.* 2017a). Additionally, if winter temperatures are below 0 °C for a prolonged period, this can slow down bacterial growth, which can lead to a bias toward summer temperatures. However, a potential seasonal bias is irrelevant in this case, given that Danau Padang is located at near-equatorial latitudes, where temperatures remain well above freezing, and virtually constant throughout the year.

There is a possibility that models under-estimate the range of temperature variability at low latitudes, and that this range was in fact considerably larger on land compared to STT. Nonetheless, this seems unlikely.

An incorrect temperature calibration is the final and most likely explanation for the broad span of temperatures recorded in peat core RP-1A-REPA (Danau Padang). The presence of abundant isomers that are not included in *brGDGT*-based proxies (e.g., H-*brGDGTs*, 7-methyl, 5/6-methyl, etc.) suggests that calibrations could be improved if precise mathematical relations between these isomers and the different environmental parameters were established. In order

for that to happen, more research on these different isomers is needed. Improvements in the separation can be expected by the application of slower flow rates and the use of additional HPLC columns. Moreover, there is a potential difference between oxic and anoxic production of *brGDGTs* which is not accounted for in the current calibrations. The uneven geographical distribution of the soils and peats used for calibration suggests a potential need for a tropical peat-specific temperature calibration. Even though peat-specific calibrations have been implied to reconstruct temperatures from low-latitude peats more accurately (Naafs *et al.* 2017a), there is a possibility that *brGDGTs* distributions might vary between boreal and tropical peats, given their geographical, environmental, vegetation, and geochemical differences. Additionally, in the absence of cultures of *brGDGTs*-producing bacteria, incubation experiments at different temperatures could contribute to the improvement of temperature calibrations (Naafs *et al.* 2019).

It has been reported that the application of soil-based proxies to peats can greatly overestimate temperature and pH reconstructions compared to the instrumental measurements (Naafs *et al.* 2017a). However, in the case of peat core RP-1A-REPA (Danau Padang), the temperatures calculated from the soil calibrations (De Jonge *et al.* 2014; Naafs *et al.* 2017b) appear to be more realistic than those from the peat-specific one (Naafs *et al.* 2017a) (Fig. 20). Particularly the soil calibration proposed by Naafs *et al.* (2017b) produced temperature estimates from the top of the profile that are in accordance with current instrumental measurements (Fig. 5). Nevertheless, they still show an excessively wide range. Crampton-Flood *et al.* (2020) presented a calibration model based on Bayesian statistics that could be applied to both peats and mineral soils. After applying their BayMBT₀ model (using an average temperature value of 22 °C and a standard deviation of 10 as parameters) to the MBT'_{5ME} values from Danau Padang, temperatures between 25.72 and 17.55 °C were estimated. Once again, this span is too broad, and in this case, top-profile values are overestimated by almost 4 °C. Assuming that the MBT'_{5ME} curve for core RP-1A-REPA shows accurate trends and oscillations, it is possible to constrain temperatures within what would be a more 'probable' range for the last 8 kyr, where top-profile values match current temperatures. Given that terrestrial temperature variability tends to be higher than its marine counterpart (Kaufman *et al.* 2020a), a total temperature increase of 3 °C during this interval of the Holocene at the study site, although probably an overestimation, is still within the realm of possibility. Hence, values between 19 and 22 °C were used for a conjectured temperature calibration, which is nothing more than an educated guess (Fig. 20). The details of these different calibrations can be found in Appendix F.

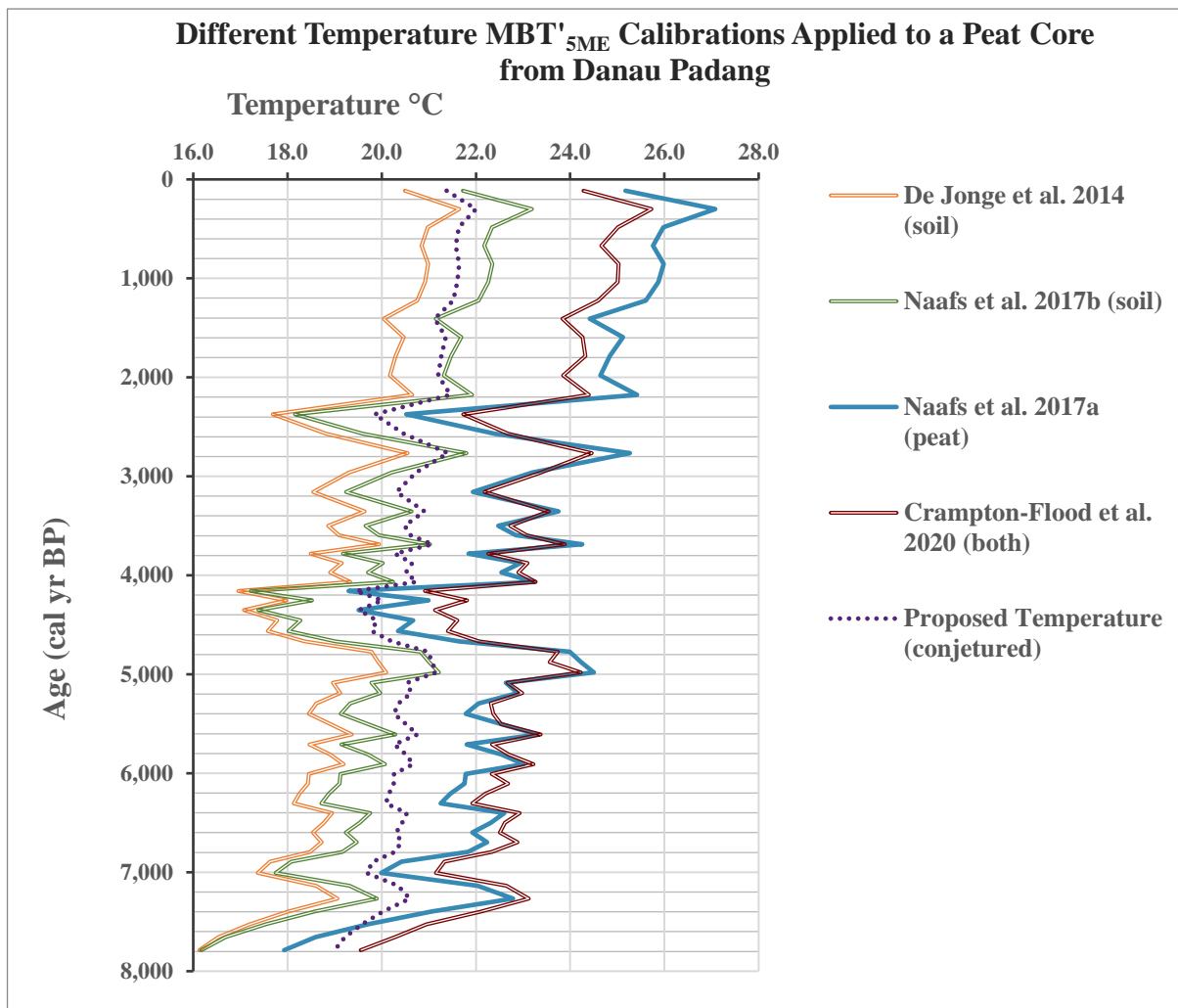


Figure 20. Different temperature MBT'5me calibrations applied to peat core RP-1A-REPA from Danau Padang, Sumatra. The proposed temperature estimates are represented by the dotted purple line. Details can be found in Appendix F.

It is noteworthy to point out that the error of the peat-specific calibration (Naaf *et al.* 2017a) is ± 4.7 °C, which calls for caution when reconstructing small temperature changes, such as those that seem to have taken place during the Holocene, particularly at nearly equatorial latitudes. *br*GDGTs-derived temperature reconstructions are better suited for larger-amplitude and longer-term variations, such as glacial-interglacial transitions (Naafs *et al.* 2017a). Moreover, *br*GDGT-based temperature reconstructions should ideally be compared with other temperature proxy records, but there is an important scarcity of temperature proxies that can be applied to peat, particularly those of quantitative nature (Naafs *et al.* 2019). One of the temperature proxies that could be used in peat comes from leaf waxes, since the carbon preference index (CPI) and the average chain length (ACL) of n-alkanes can be used to produce qualitative temperature signals (Naafs *et al.* 2019). Unfortunately, despite being analyzed, n-alkanes were not quantified for this thesis work due to time limitations. Nonetheless, C isotopic values can be affected by temperature changes, where higher $\delta^{13}\text{C}$ values in peatlands might be associated with lower temperatures (Hobbie *et al.* 2017). The fact that the two large negative temperature anomalies shown by the *br*GDGTs-based temperature proxy for Danau Padang (4-

5 and 2.2-2.8 kyr BP) coincide with large ^{13}C enrichment oscillations is encouraging. However, there is a multitude of other factors that can influence $\delta^{13}\text{C}$ values, which will be discussed further down in this text.

Kaufman *et al.* (2020a & b) presented a global compilation of 1,319 Holocene temperature proxy records from 679 different sites, marine and terrestrial. They aimed to minimize proxy biases by using a multi-proxy approach. According to this compilation, the majority of records show a peak in warmth around 7 ± 2 kyr, followed by a cooling trend until the onset of the Industrial Revolution, when the atmospheric concentration of greenhouse gases increased dramatically. However, the latter are thought to have increased not only after industrial times, but over the entire Holocene, which should have led to higher temperatures, thereby contradicting the recorded cooling trend. Thus, there is a juxtaposition between most temperature records, which suggest cooling during the second half of the Holocene, and climate models, which simulate a warming trend. This is called the “Holocene temperature conundrum” (Liu *et al.* 2014). This discrepancy could be due to a seasonal bias in temperature records, or due to a regional and seasonal climate sensitivity bias in climate models (Liu *et al.* 2014). Models base this prediction not only on the rise in atmospheric concentrations of greenhouse gases during this time interval, but also on the ongoing retreat of ice sheets. Hence, if climate records are correct, other factors, such as orbital insolation or the melt water resulting from the retreating ice sheets, must have been powerful enough to overcompensate for the warming. Nonetheless, orbital cycles do not appear to have had a significant impact on temperatures during this period (Liu *et al.* 2014). The global warming trend simulated by climate models suggests warming by approximately $0.5\text{ }^{\circ}\text{C}$ during the last 8 kyr (Liu *et al.* 2014). Conversely, temperature proxy records show a cooling trend that ranges from about $4\text{ }^{\circ}\text{C}$ at high latitudes in the Northern Hemisphere, to less than $0.5\text{ }^{\circ}\text{C}$ at low latitudes (Kaufman *et al.* 2020b). It is important to note that temperature variability was most likely lower at all latitudes in the Southern Hemisphere compared to the Northern Hemisphere. This is supported by the overwhelming majority of temperature records (Kaufman *et al.* 2020b).

A global cold interval that took place between 5 and 4 kyr ago has been widely suggested by marine and terrestrial records around the world (Kuhnert *et al.* 2014). This is coincidental with the record from Danau Padang, which shows a large temperature drop followed by a recovery during that period of time. Additionally, Griffiths *et al.* (2010) and Abram *et al.* (2009) independently reported a decrease of approximately $-2.5\text{ }^{\circ}\text{C}$ during this time interval, recorded in a speleothem from a cave on Flores (southern Indonesia) and in corals near the Mentawai Islands (less than 200 km from Danau Padang), respectively.

The climate of Danau Padang is widely influenced by the conditions in the eastern tropical Indian Ocean region (Niedermeyer *et al.* 2014). Different records have provided independent, and sometimes contradicting mid- and late-Holocene temperature reconstructions for this region (Seitawan *et al.* 2015). Some records (Mohtadi *et al.* 2010a & 2010b), including the one from Danau Padang, show a clear warming trend, while others show a cooling trend (Gibbons *et al.* 2014), or no apparent trend at all (Mohtadi *et al.* 2014; Xu *et al.* 2008). The different temporal resolutions could potentially account only for part of this discrepancy. Furthermore, there does not seem to be a clear geographic control that could explain it either (Seitawan *et al.*

2015). Two temperature records presented by Mohtadi *et al.* (2010a & 2010b) show remarkably similar curves to the core from Danau Padang (Fig. 21). They were both reconstructed from marine-sediment cores obtained from the Mentawai Basin (near west Sumatra). One (core GeoB10029-4) was recovered off the coast between Sumatra and Siberut, only about 250 km northwest of Danau Padang, while the other (core GeoB10038-4) was collected from a location roughly 500 km southeast of Danau Padang, which is an area normally affected by seasonal upwelling. Curiously, the temperature curve of the latter (core GeoB10038-4) resembles that of Danau Padang more than the former does, in spite of being recovered from a further distance and from a location influenced by upwelling. The two large negative temperature anomalies that were recorded at Danau Padang 5-4 kyr and 2.8-2.2 kyr BP, also appear in the GeoB10038-4 record, but shifted around 300 yr into the past. Conversely, the GeoB10029-4 profile also suggests the existence of these colder periods, only this time there is a discordance of over -500 yr (earlier) relative to the RP-1A-REPA record, making it difficult to draw a clear correlation. Nonetheless, misalignments could also be explained by the different temporal resolution of the three records, added to the generally larger uncertainty when dating marine cores (Fig. 21). According to most records, the start of modern ENSO periodicity in the tropical Pacific took place approximately 5 kyr BP (Gagan *et al.* 2004), with large intensifications in magnitude between 5-4 kyr and 3-2 kyr BP. During El Niño years, particularly strong easterly winds seem to be associated with the prolongation of upwelling into November and its expansion toward northern Sumatra (Susanto *et al.* 2001). Perhaps this could potentially explain why the two negative temperature anomalies are more apparent in the GeoB10038-4 and RP-1A-REPA records, compared to other records from locations further north.

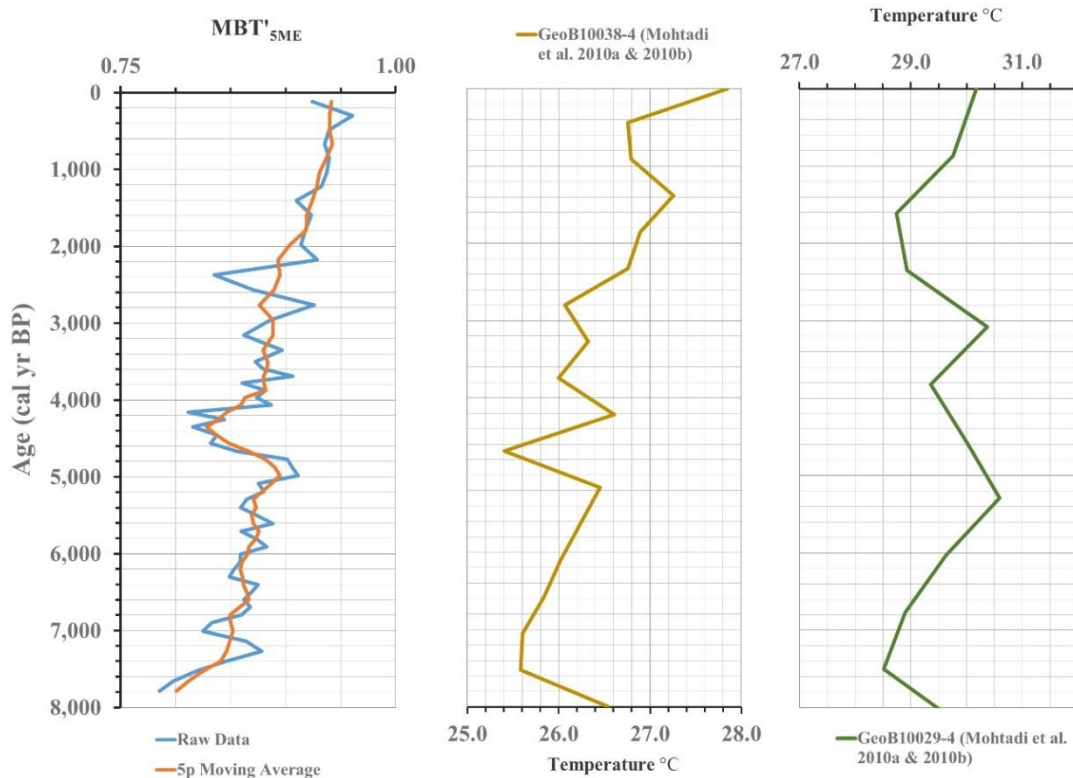


Figure 21. Comparison between the MBT'5me record (temperature) from peat core RP-1A-REPA, Danau Padang, Sumatra (left), and two marine records provided by Mohtadi *et al.* 2010a & 2010b. The record on the left has 60 data points, whereas the ones in the middle and right have 17 and 11, respectively.

5.3 pH Reconstruction

The distributions of *br*GDGTs are more strongly correlated with temperature than with pH in peats, as opposed to mineral soils (Naafs *et al.* 2017a). Nonetheless, the pH values calculated for Danau Padang fit the typical values in peatlands (pH 3-6). The IR_{6ME} and IBT indices, which can be used as qualitative pH indicators, show trends very similar to the CBT curve (Fig. 14). However, they disagree for the bottom 1 meter (~ 6.6-7.8 cal yr BP) of the peat profile. While the CBT indicates a relatively steady trend toward more acidic conditions during this time interval, the IR_{6ME} and IBT suggest otherwise. This is probably due to the influence of other environmental factors on the latter two indices.

5.4 Vegetation Reconstruction

Because changes in biomass type can influence C and N content in the sediment, as well as their isotopic compositions, it is important to first constrain the possible sources of organic matter in the peat. Pollen assemblages can provide information about changes in vegetation type (Chambers *et al.* 2012). Fortunately, Morley conducted a palynological study (1982) that concluded that tropical trees, which are C3 plants, had been the dominant vegetation type in the area surrounding Danau Padang during the roughly 8,000 yr covered in the present thesis work. This is supported by multiple other records including one from Danau di Atlas, which is also located on central Sumatra (Newsome & Flenley 1988). Interpreting the $\delta^{13}\text{C}$ values of peat sediments is highly complex due to the competing influence of climate, organism type, and atmospheric C isotopic values (Diefendorf & Freimuth 2017). Luckily, atmospheric $\delta^{13}\text{C}$ values have remained relatively constant for the time interval studied here, until the onset of industrial times (Hare *et al.* 2018). In plants, $\delta^{13}\text{C}$ values depend on a wide range of complex factors such as the photosynthetic pathway employed, fractionation during photosynthesis, water availability, water use efficiency, changes in the plant community, and more (Eglinton & Eglinton 2008; Diefendorf & Freimuth 2017). However, $\delta^{13}\text{C}$ data can be combined with $\delta^{15}\text{N}$ and C/N records to identify changes in biomass or vegetation communities. The most common use for $\delta^{13}\text{C}$ values is as a proxy for changes in the ratio of C3 (commonly forest, more depleted in ^{13}C) to C4 (mostly grasses, more enriched in ^{13}C) plant communities (Eglinton & Eglinton 2008). The $\delta^{13}\text{C}$ values recorded at Danau Padang remain stable throughout the profile, with small variations that oscillate around -29 ‰. This values fit very well within the expected range for C3 plants, and rules out any significant contribution from C4 plants ($\delta^{13}\text{C}$ ~ -15 ‰). However, the C isotopic values of algae, which can be present in peats under waterlogged conditions, and (especially) macrophytes, can sometimes reach these low values (Cloern *et al.* 2002; Ku *et al.* 2007). $\delta^{15}\text{N}$ values can help in this regard, since both algae and macrophytes tend to be slightly more enriched in ^{15}N (normally above 0 ‰) than C3 land plants (Cloern *et al.* 2002; Ku *et al.* 2007). Thus, the $\delta^{15}\text{N}$ values presented for Danau Padang (around -1 ‰), although not in a definitive way, fit better those of terrestrial C3 vegetation. Finally, woody land plants are rich in cellulose and lignin, and contain higher C/N than softer-tissue biome, such as macrophytes (Yamoah *et al.* 2021), herbaceous vegetation (e.g., grasses), algae, and microorganisms (Ku *et al.* 2007). The C to N ratio of aquatic algae does not usually surpass 20, so given that the lowest value recorded in the Danau Padang profile is 27.1, it can be

concluded with high certainty that algae did not contribute significantly to the composition of the peat. For a more accurate and detailed interpretation, the distribution of leaf wax compounds (such as n-alkane), as well as their C isotopic values could help distinguish between different plant functional types, such as C3 land plants and C3 macrophytes among others (Andrae *et al.* 2020; Eglinton & Eglinton 2008).

5.5 XRF Measurements

XRF measurements can be affected by changes in the water content, sediment grain size, and roughness of the sediment surface (Löwemark, *et al.* 2011). Moreover, the aging of the X-ray tube can also influence XRF measurements, which can lead to discrepancies when different sections of the core are measured at different times (Löwemark, *et al.* 2011). That could explain the mismatches (misalignments) observed in the XRF measurements for peat core RP-1A-REPA (Danau Padang), since they coincide with different measurement dates.

5.6 Precipitation and Input of Minerogenic Material

Hydrogen isotope ratios from leaf-waxes present in peat are usually used to reconstruct precipitation (Chambers *et al.* 2012). In the absence of a δD record for Danau Padang, it is extremely difficult to reconstruct peat hydrology. However, small qualitative indicators can be inferred from other geochemical signals. Higher decay rates are expected to take place under dry conditions compared to waterlogged ones (Chambers *et al.* 2012). C loss from microbial decomposition not only causes a lowering of the C/N (Kaislahti Tillman *et al.* 2010), but it also results in higher $\delta^{13}C$ values due to ^{13}C discrimination (Hobbie *et al.* 2017). Nonetheless, C/N values are not linked to degree of decomposition in the oxic acrotelm layer (Kaislahti Tillman *et al.* 2010). Furthermore, when the absence of C4 plants is certain, and if vegetation communities remain constant or are well constrained, it is possible to obtain a qualitative precipitation signal from $\delta^{13}C$. Water availability greatly influences the stomatal conductance of plants C3, which in turn affects C fractionation during photosynthesis (Diefendorf & Freimuth 2017). Nevertheless, this can be extremely intricate given that each plant species has a unique relation between water availability and fractionation (Diefendorf & Freimuth 2017). A decrease in $\delta^{13}C$ could be the result of an increase in precipitation that altered the structure of C3 forests (Kohn 2010; Russell *et al.* 2014; Amesbury *et al.* 2015), although this relationship remains contentious and should be used with extreme caution (Amesbury *et al.* 2015).

Aeolian dust tends to be enriched in Ti, so Ti can be used as an indicator for changes in wind regimes (Löwemark *et al.* 2011). Moreover, Ti/Al variations can be interpreted as qualitative changes in the minerogenic portion of the sediment (Russell *et al.* 2014), which should be (and generally are, in the case of core RP-1A-REPA) reflected in the density and magnetic susceptibility measurements (Xiao *et al.* 2017). Furthermore, since Al is relatively unaffected by weathering, increases in Ti/Al could also be interpreted as periods of increased chemical weathering induced by enhanced precipitation (Löwemark *et al.* 2011; Russel *et al.* 2014).

The ratio of *iso*GDGTs-0 to *br*GDGTs could potentially be used as a proxy for variations in the depth of the acrotelm-catotelm boundary, since *iso*GDGTs-0 is mainly produced by anaerobic archaea (probably methanogens) (Naafs *et al.* 2017). This in turn could be used as a signal for changes in the water table, given that waterlogged settings lead to a rise of the acrotelm-catotelm boundary, and consequently to wider-spread anoxic or suboxic conditions. Moreover, Dang *et al.* (2016) provided evidence that suggested the *br*GDGT distribution is considerably influenced by moisture in semi-arid and arid soils. The IR_{6ME} index shows higher values in mineral soils than in peats with similar pH, indicating that there is a negative correlation between the abundance of 6-methyl isomers and water content (Naafs *et al.* 2017a). Hence, differences between the CBT_{peat} and the IR_{6ME} can potentially be interpreted as qualitative changes in the water table. However, this relationship has not been established in peats, most likely because they are almost entirely water saturated. The analysis of testate amoebae, which was not performed for the present thesis work, can give useful information about changes in the water table (Chambers *et al.* 2012).

Tropical $\delta^{18}\text{O}$ speleothem records are excellent precipitation proxies since they reflect the O isotopic composition of rainfall water, although they can also be influenced by changes in temperature. During periods of stronger monsoons, highly fractionated (^{18}O depleted) water that has traveled long distances falls as precipitation (Ruddiman 2014). Conversely, when monsoons are weaker, not only is there a decrease in precipitation, but the rainfall is delivered from less fractionated (more ^{18}O -rich) water vapor, provided from more ‘local’ sources. Different rainfall reconstructions suggest abnormal patterns over Indonesia between 6 and 4 kyr ago (Kuhnert *et al.* 2014), as it is exemplified by the opposing trends shown in $\delta^{18}\text{O}$ speleothem-based records from Flores (Griffiths *et al.* 2010) and Borneo (Partin *et al.* 2007). However, precipitation over western Sumatra is derived predominately from the Indian Ocean, since the Barisan Mountains act as an orographic barrier, preventing moisture from the west Pacific from reaching the west coast (Niedermeyer *et al.* 2014). Hence, precipitation records from eastern Indonesia are most likely inaccurate when applied to western Sumatra. Niedermeyer *et al.* (2014) provided a record of precipitation for northwest Sumatra, which is therefore much more likely to coincide with rainfall patterns in Danau Padang. This record was obtained from a marine core (550 km northwest of Danau Padang), and it is based on the δD composition of terrestrial plant waxes. It shows three periods of increased precipitation: the highest precipitation rates were recorded between 8 and 6 kyr BP, the second most distinct period took place between 2 and 1 kyr ago, and finally a more moderate interval was shown between 4.5 and 2.5 kyr BP. This appears to be more in accordance with the record from Flores (Griffiths *et al.* 2010) than with the one from Borneo (Partin *et al.* 2007). These three periods of increased rainfall roughly coincide in age (but not in intensity) with three discernible positive trends in the GDGT-0/*br*GDGTs in the Danau Padang profile. The two most recent ones match intervals of increased ^{13}C depletion in the peat. However, since methanogenic activity should be directly proportional to C content near the top of the anoxic catotelm (Blodau *et al.* 2011), the apparent trough in methanogenic activity around 4.5 kyr BP (which splits the two peaks) could simply be a result of the significant decrease in C content observed in the profile at that time. The same can be said for the two most recent intervals of ^{13}C depletion (~ 4.3-2.4 and 2-0 kyr BP) which might in fact be a consequence of the presence of two clear ^{13}C maxima (~

2.4 and 4.4-4.6 kyr BP), that match periods of cooler conditions. Besides, these intervals of increased rainfall reported by Niedermeyer *et al.* (2014) are not reflected on the Ti/Al or the magnetic susceptibility curves, which show high values that only coincide with the more moderate one (~ 4.5-2.5 kyr BP). Therefore, it is unclear to what extent this record from northwest Sumatra (Niedermeyer *et al.* 2014) represents rainfall patterns in Danau Padang.

Niedermeyer *et al.* (2014) also suggested an intensification of the southeast monsoon in northwest Sumatra during the mid-Holocene, which is thought to have been accompanied by a norward migration of the ITCZ. However, this is not believed to have had an impact on precipitation in northwest Sumatra since precipitation patterns in this region today do not seem to be related to the position of the ITCZ. Furthermore, they reported that palynological studies in East Africa and northwest Sumatra, as well as opposite precipitation trends between the two regions, indicate that the current IOD precipitation gradient has very likely been persistent during the last 8 kyr, and that it has been the main precipitation modulator in this geographic area.

On the other hand, Wurtzel *et al.* (2018) provided a $\delta^{18}\text{O}$ speleothem record from the Tangga Cave, which is located in central west Sumatra, within the Barisan Mountains, about 200 km to the northwest of Danau Padang. This record appears to match the data from Danau Padang a lot better than any of the other precipitation records already described (Fig. 22), which is encouraging given its proximity to the study site. The Ti/Al curve parallels almost identically the $\delta^{18}\text{O}$ record from the Tangga Cave for the period between 5 kyr BP and the present. The magnetic susceptibility measurements also show a relatively good matching trend over this time interval, so do the bulk density measurements, particularly for the most recent 5 kyr. Differences among the bulk density, Ti/Al, and magnetic susceptibility curves can be due changes in the source of minerogenic material. On the other hand, C accumulation rates seem to better match the precipitation record from the Tangga Cave from 8 to 5 and from 1.5 to 0 kyr BP. C accumulation rates normally increase during periods of increased rainfall in peats due to an increase in vegetation density, and more widespread anoxic conditions, which in turn slow down decomposition. The only large discrepancy between the two profiles takes place around 3.5 kyr BP. However, this could easily be explained by the low resolution of the peat accretion rate record, which shows an unrealistically large shift caused by the presence of a radiocarbon measurement at this depth (185 cm). Thus, the C accumulation rate record also contributes to the relevance of the Tangga Cave record to the climate of Danau Padang. In addition, the $\delta^{13}\text{C}$ curve from Danau Padang also mimics to a certain extent the $\delta^{18}\text{O}$ record from the Tangga Cave, particularly for the periods 8-5 and 2-0 kyr BP. Nonetheless, care must be taken when comparing the records from Danau Padang with that from the Tangga Cave, given the distance that separates them, and due to the fact that they have different temporal resolutions, which can lead to alignment inaccuracies.

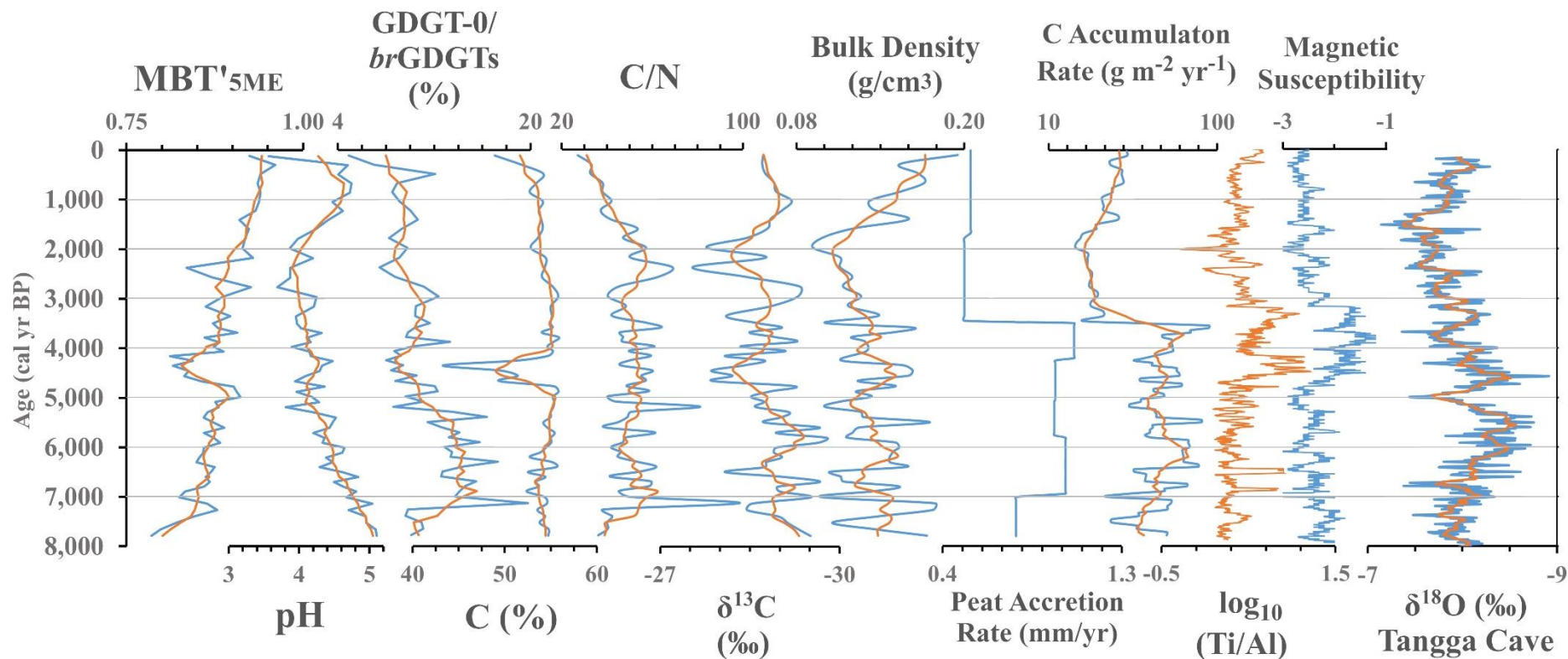


Figure 22. Compiled climate and environmental proxies from peat core RP-1A-REPA, Danau Padang, western central Sumatra, and *O* isotopic speleothem (precipitation) record from the Tangga Cave, western central Sumatra (Wurtzel et al. 2018). Blue lines represent raw data while orange lines are 5-point moving averages, with the exception of the five left-most plots, where the orange lines represent 21-p, 9-p, 9-p, and 9-p, moving averages, respectively from left to right. The three left-most curves are GDGT-based. MBT'5me was calculated according to De Jonge et al. 2014, and pH according to Naafs et al. 2017a.

5.7 Compiled Paleoclimatic and Paleoenvironmental Reconstruction

After combining all the geochemical proxies extracted from the peat profile collected from Danau Padang, together with the precipitation record from Tangga Cave (Wurtzel *et al.* 2018), it was possible to make some assumptions about the evolution of the climate and the environment over the last 8 kyr in Danau Padang (core RP-1A-REPA). Firstly, from Morley's palynological study (1982) together with the geochemical evidence provided in the present study ($\delta^{13}\text{C}$, $\delta^{15}\text{N}$, C/N) it was possible to conclude that the dominant vegetation type in Danau Padang's surrounding area since the mid-late Holocene has been C3 terrestrial plants, primarily tropical trees.

Temperatures appear to have increased relatively steadily between 7.8 and 5 kyr BP, as indicated by both the $\text{MBT}'_{5\text{ME}}$ and the $\text{H-MBT}_{\text{acyclic}}$ indices. This trend seems to have been accompanied also by a uniform acidification of the peatland (from 5 to 4.2 pH), as illustrated by the CBT_{peat} index. Moreover, the $\delta^{18}\text{O}$ values from the Tangga Cave record (Wurtzel *et al.* 2018) show a steady monsoon intensification until 5.4 kyr BP, followed by a sudden drop in precipitation that reaches a minimum within 400 yr (5 kyr BP). This pattern is echoed relatively well by the Ti/Al, magnetic susceptibility, and C accumulation rate records (to a certain extent also by the $\text{isoGDGTs-0/brGDGTs}$) for Danau Padang. However, no clear signal was obtained from the other proxies. The interval between 5 and 4 kyr BP appears to have experienced the most intense and simultaneous geochemical disturbance in the entire peat profile. This period is characterized by a large shift toward cooler conditions followed by a rapid recovery before the end of the millennium. This was seemingly accompanied by synchronous positive pH and $\delta^{13}\text{C}$ anomalies, the latter of which was likely a reflection of the cooling episode. More importantly, this was probably a period of intense rainfall as suggested by the $\delta^{18}\text{O}$ record from the Tangga Cave (decrease), which coincides with large inputs of minerogenic material, indicated by the higher Ti/Al, higher magnetic susceptibility, higher bulk density, and lower C content. Further support for this interpretation comes from the relatively high C accumulation rates estimated for this interval. Wind activity might have been intensified during this period as well. Interestingly, $\text{isoGDGTs-0/brGDGTs}$ values indicate a decrease in methanogenic activity during this episode. Nonetheless, this could be linked to the lower C content, assuming that not all of it was a consequence of the increased inputs in minerogenic material. This cold event has been widely suggested by marine and terrestrial records around the world (Kuhnert *et al.* 2014). The time that followed until the Industrial Revolution was characterized by relatively linear warming, with the exception of the period between ~ 2.8 and 2.2 kyr BP, which once again represents an interruption of the gradual warming trend. The relative ^{13}C enrichment recorded at this time is in agreement with the negative temperature anomaly. However, it is difficult to interpret the precipitation signals during this time. The trend toward more acidic conditions continued until about 2.8 kyr BP (pH < 3.7), after which the CBT_{peat} index shows increasingly higher values with decreasing depth until 300 yr BP, when pH values appear to have plummeted. Lastly, the different hydrology proxies display a high level of consensus for the time interval spanning the most recent 4 kyr. Within this interval, rainfall seems to have decreased steadily until about 2-1.5 kyr BP, when there was a shift toward more abundant precipitation. This is shown independently in the Tangga Cave $\delta^{18}\text{O}$, Ti/Al, magnetic susceptibility, C accumulation rates, bulk density, and $\delta^{13}\text{C}$ records.

6. Conclusions and Future Prospects

Chromatographic peat integration for peat core RP-1A-REPA (Danau Padang) proved to be more intricate for the penta- and hexamethylated, due to the incomplete separation of certain isomers (coelution), the presence of chromatographic peaks representing unknown isomers, and the absence of specific peaks. However, randomized sample preparation, replicate analysis, and the comparison of alternative chromatographic peak integrations support the accuracy of the GDGT-distribution estimates and their derived indices. Variations in the MBT'_{5ME} index are mostly dependent on the *br*GDGTs without cyclopentane moieties (Ia, IIa, IIIa), while variations in the CBT_{peat} index are controlled by Ib at Danau Padang. The pH values calculated for the study site fit the typical values in peatlands (pH 3-6). Temperatures derived from the peat-specific calibration by Naafs *et al.* (2017a) show a total fluctuation of over 9 °C. This is most likely an overly wide range that does not represent the actual temperatures that took place at the study site during the last 8 kyr. Nonetheless, it was concluded that imprecisions in the integration of *br*GDGTs were probably not responsible for the wide range of temperatures recorded in the peat profile. This is further supported by the strong correlation between the MBT'_{5ME} and the H-MBT_{acyclic} indices. Hence, an incorrect calibration is the most probable cause of this excessively wide temperature range. The presence of abundant isomers that are not included in *br*GDGT-based proxies suggests that calibrations could be improved if precise mathematical relations between these isomers and the different environmental parameters were established. Additionally, the uneven geographical distribution of the soils and peats used for calibration supports the need for a tropical peat-specific temperature calibration. It has been reported that the application of soil-based proxies to peats can greatly overestimate temperature and pH reconstructions. However, in the case of the peat core analyzed for this thesis work, the temperatures calculated from soil calibrations appear to be more realistic than those from the peat-specific one. Given that the error of the peat-specific calibration (Naaf *et al.* 2017a) is ± 4.7 °C, its accuracy when reconstructing small temperature changes remains questionable. However, assuming that the MBT'_{5ME} calculations for core RP-1A-REPA are correct, it was possible to constrain temperatures within a realistic range (~ 3 °C), where top-profile values match current temperatures. Furthermore, two temperature records from nearby areas presented by Mohtadi *et al.* (2010a & 2010b) show remarkably similar curves to the core from Danau Padang, supporting the validity of the latter. The record from Danau Padang supports climate models, which simulate warming during the second half of the Holocene, as opposed to most proxy records. It resembles records from further south more than those from further north. This could be explained by the large intensifications in magnitude of El Niño events that coincided with several cold intervals, the former of which can expand the reach of the upwelling that is normally characteristic of the coasts of southern Java and southwestern Sumatra, further north. Moreover, there is extensive evidence that a cold event took place between 5 and 4 kyr ago.

On another note, $\delta^{13}\text{C}$, $\delta^{15}\text{N}$, and C/N values suggest that C3 plants have been the dominant vegetation type in Danau Padang's surrounding area at least since the mid-late Holocene. This is supported by Morley's palynological study (1982) among other records. Because climate, vegetation, and soil processes affect C and N contents, as well as their stable isotopic values, in ways that are still poorly understood, their interpretation is complex. In the absence of a δD record for Danau Padang, it was difficult to reconstruct past hydrology. However, subtle

qualitative indicators could be inferred from other geochemical signals (Ti/Al, magnetic susceptibility, bulk density, $\delta^{13}\text{C}$, and *iso*GDGTs-0/*br*GDGTs). Additionally, Wurtzel *et al.* (2018) provided a $\delta^{18}\text{O}$ speleothem record from the Tangga Cave (~ 200 km to the northwest of Danau Padang) that matches the qualitative precipitation proxies from Danau Padang considerably well.

To conclude, not all proxies can be applied universally, due differences in species-assemblages, peat formation processes, topography, and geochemical conditions. Since similar proxies can respond to slightly different environmental factors, a multi-proxy approach is recommended for the more precise extraction of climatic and environmental signals. Thus, the analysis of leaf wax n-alkanes, as well as their compound specific stable isotopes, could provide more definite answers about changes in the vegetation community, precipitation patterns, and temperature. The temperature record produced in this thesis work shows great promise, being one of the first truly terrestrial temperature records from the IPWP.

7. References

- Abram, N. J., McGregor, H. V., Gagan, M. K., Hantoro, W. S. & Suwargadi, B. W., 2009: Oscillations in the southern extent of the Indo-Pacific Warm Pool during the mid-Holocene. *Quaternary Science Reviews*, vol 28, pp. 2794-2803.
- Amesbury, M. J., Charman, D. J., Newnham, R. M., Loader, N. J., Goodrich, J. P., Royles, J., Campbell, D. I., Roland, T. P. & Gallego-Sala, A., 2015: Carbon stable isotopes as a paleoclimate proxy in vascular plant dominated peatlands. *Geochimica et Cosmochimica Acta*, vol. 164, pp. 161-174.
- Ballantyne, A. P., Greenwood, D. R., Sinninghe Damsté, J. S., Csank, A. Z., Eberle, J. J. & Rycbyzinski, N., 2010: Significantly Warmer Arctic Surface Temperatures During the Pliocene Indicated by Multiple Independent Proxies. *Geology*, vol. 38, pp. 603–606
- Barber, K. E., 1981: *Peat Stratigraphy and Climatic Change - A Palaeoecological Test of the Theory of Cyclic Peat Bog Regeneration*. A. A. Balkema, Rotterdam.
- Becker, K. W., Lipp, J. S., Zhu, C., Liu, X. -L. & Hinrichs, K. U., 2013: An Improved Method for the Analysis of Archaeal and Bacterial Ether Core Lipids. *Organic Geochemistry*, vol. 61, pp. 34–44.
- Blodau, C. Siems, M. & Beer, J., 2011: Experimental burial inhibits methanogenesis and anaerobic decomposition in water-saturated peats. *Environmental Science & Technology*, vol. 45 (23), pp. 9984-9989.
- Braxmeier, H., [n.d.]: *Relief Map*. Image, Maps for Free. Produced by the OpenStreetMap Foundation using OpenStreetMap data. Web-page, <https://maps-for-free.com/>. Accessed 2021-07-06.
- Bronk Ramsey, C., 2008: Radiocarbon dating: Revolutions in understanding. *Archaeometry*, vol. 50(2), pp. 249–275.
- Chambers, F. M., Booth, K.R., De Vleeschouwer, F., Lamentowicz, M., Le Roux, G., Mauquoy, D., Nichols, J. E. & van Geel, B., 2012: Development and refinement of proxy-climate indicators from peats. *Quaternary International*, vol. 268, pp. 21-33.
- Chambers, F. M. & Charman, D. J., 2004: Holocene Environmental change – Contributions from the Peatland Achieve. *The Holocene*, vol. 12 (1), pp. 1-6.
- Chappe, B., Albrecht, P., Michaelis, W., 1982: Polar lipids of Archaeobacteria in sediments and petroleums. *Science*, vol. 217, pp. 65–66.
- Cloern, J. E., Canuel, E. A. & Harris, D., 2002: Stable carbon and nitrogen isotope composition of aquatic and terrestrial plants of the San Francisco Bay estuarine system. *Limnology and Oceanography*, vol. 47 (3), pp. 713-729.
- Crampton-Flood, E. D., Tierney, J. E., Peterse, F., Kirkels, F. M. S. A. & Damsté, J. S. S., 2020: BayMBT: A Bayesian calibration model for branched glycerol dialkyl glycerol tetraethers in soils and peats. *Geochimica et Cosmochimica Acta*, vol. 268, pp. 142-159.

- Dang, H., Jian, Z., Wang, Y., Mohtadi, M., Rosenthal, Y., Ye, L., Bassinot, F. & Kuhnt, E., 2020: Pacific Warm Pool Subsurface Heat Sequestration Modulated Walker Circulation and ENSO Activity during the Holocene. *Science Advances*, vol. 6 (42), pp. 1-8.
- Dang, X., Yang, H., Naafs, B. D. A., Pancost, R. D., Evershed, R. P. & Xie, S., 2016. Direct evidence of moisture control on the methylation of branched glycerol dialkyl glycerol tetraethers in semi-arid and arid soils. *Geochimica et Cosmochimica Acta*, vol. 189, pp. 24–36.
- Davies, M. A., Blewett, J., Naafs, B. D. A., Finkelstein, S. A., 2021: Ecohydrological Controls on Apparent Rates of Peat Carbon Accumulation in a Boreal Bog Record from the Hudson Bay Lowlands, Northern Ontario, Canada. *Quaternary Research*, vol. [n.k.], pp. 1-14.
- De Jonge, C., Hopmans, E., Stadnitskaia, A., Rijpstra, W. I. C., Hofland, R., Tegelaar, E. & Sinninghe Damsté, J. S., 2013: Identification of Novel Penta- and Hexamethylated Branched Glycerol Dialkyl, Glycerol Tetraethers in Peat using HPLC-MS, GC-MS and GC-SMB-MS. *Organic Geochemistry*, vol. 54, pp. 78-82.
- De Jonge, C., Hopmans, E. C., Zell, Kim, J., Schouten, S. & Sinninghe Damsté, J. S., 2014: Occurrence and Abundance of 6-methyl Branched Glycerol Dialkyl, Glycerol Tetraethers in Soils – Implications for Palaeoclimate Reconstruction. *Geochimica et Cosmochimica Acta*, vol. 141, pp. 97-112.
- Diefendorf, A. F. & Fremuth, E. J., 2017: Extracting the most from terrestrial plant-derived n-alkyl lipids and their carbon isotopes from the sedimentary record: A review. *Organic Geochemistry*, vol. 103, pp. 1-21.
- Ding, S., Schwab, V. F., Ueberschaar, N., Roth, V.-N., Lange, M., Xu, Y., Gleixner, G. & Pohnert, G., 2016: Identification of Novel 7-methyl and Cyclopentanyl Branched Glycerol Dialkyl Glycerol Tetraethers in Lake Sediments. *Organic Geochemistry*, vol. 102, pp. 52–58.
- Ding, S., Xu, Y., Wang, Y., He, Y., Hou, J., Chen, L. & He, J. S., 2015: Distribution of branched glycerol dialkyl glycerol tetraethers in surface soils of the Qinghai-Tibetan Plateau: implications of brGDGTs-based proxies in cold and dry regions. *Biogeosciences*, vol. 12(11), pp. 3141–3151.
- Duvel, J. P., 2012: Oceans and Air-Sea Interaction. In: Lau, W. K. & Waliser, D. E., *Intraseasonal Variability in the Atmosphere-Ocean Climate System*. (2nd edition) Springer, Heidelberg. pp. 527-528.
- Eglinton, T. I. & Eglinton, G., 2008: Molecular Proxies for Paleoclimatology. *Earth and Planetary Letters*, vol. 275, pp. 1-16.
- Gagan, M. K., Hendy, E. J., Haberle, S. G. & Hantoro, W. S., 2004: Post-glacial Evolution of the Indo-Pacific Warm Pool and El Niño-Southern Oscillation. *Quaternary International*, vol. 118-119, pp. 127-143.

- Gibbons, F. T., Oppo, D. W., Mohtadi, M., Rosenthal, Y., Cheng, J., Liu, Z. & Linsley, B. K., 2014: Deglacial $\delta^{18}\text{O}$ and hydrologic variability in the tropical Pacific and Indian Oceans. *Earth and Planetary Science Letters*, vol. 387, pp. 240–251.
- Google Earth, 1985: *Danau Padang*, Sumatra, 2°12'17''S, 101°31'36''E, elevation 3.3 km. 2D map. Web-page, <http://www.google.com/earth/index.html>. Accessed 2021-07-06.
- Google Earth, 2018: *Danau Padang*, Sumatra, 2°12'17''S, 101°31'36''E, elevation 3.3 km. 2D map. Web-page, <http://www.google.com/earth/index.html>. Accessed 2021-07-07.
- Goswami, B. N., 2012: South Asian Monsoon. In: Lau, W. K. & Waliser, D. E., *Intraseasonal Variability in the Atmosphere-Ocean Climate System*. (2nd edition) Springer, Heidelberg. pp. 41.
- Griffiths, M. L., Drysdale, R. N., Vonhof, H. B., Gagan, M. K., Zhao, J., Ayliffe, L. K., Hantoro, W. S., Hellstrom, J. C., Cartwright, I., Frisia, S. & Suwargadi, B. W., 2010: Younger Dryas–Holocene Temperature and Rainfall History of Southern Indonesia from $\delta^{18}\text{O}$ in Speleothem Calcite and Fluid Inclusions. *Earth and Planetary Science Letters*, vol. 295 (1-2), pp. 30–36.
- Hare, V. J., Loftus, E., Jeffrey, A. & Bronk Ramsey, C., 2018: Atmospheric CO₂ effect on stable isotope composition of terrestrial fossil archives. *Nature Communications*, vol. 9, article 252.
- Hobbie, A. E., Chen, J., Hanson, P. J., Iversen, C. M., McFarlane, K. J., Thorp, N. R. & Hofmockel, K. S., 2017: Long-term Carbon and Nitrogen Dynamics at SPRUCE Revealed through Stable Isotopes in Peat Profiles. *Biogeosciences*, vol. 14, pp. 2481–2494.
- Hogg, A. G., Heaton, T. J., Hua, Q., Palmer, J. G., Turney, C. S. M., Southon, J., Bayliss, A., Blackwell, P. G., Boswijk, G., Bronk Ramsey, C., Pearson, C., Petchey, F., Reimer, P., Reimer, R. & Wacker, L., 2020: SHCal20 Southern Hemisphere Calibration, 0–55,000 Years cal BP. *Radiocarbon*, vol. 62(4), pp. 759–778.
- Hopmans, E. C., Schouten, S., Pancost, R. D., van der Meer, M. T. J., Sinninghe Damsté, J. S., 2000: Analysis of Intact Tetraether Lipids in Archaeal Cell Material and Sediments by High Performance Liquid Chromatography/Atmospheric Pressure Chemical Ionization Mass Spectrometry. *Rapid Communications in Mass Spectrometry*, vol. 14, pp. 585–589.
- Hopmans, E. C., Schouten, S. & Sinninghe Damsté, J. S., 2016: The Effect of Improved Chromatography on GDGT-based Paleoproxies. *Organic Geochemistry*, vol. 93, pp. 1–6.
- Hopmans, E. C., Weijers, J. W. H., Schefuss, E., Herfort, L., Sinninghe Damsté, J. S. & Schouten, S., 2004: A Novel Proxy for Terrestrial Organic Matter in Sediments Based on Branched and Isoprenoid Tetraether Lipids. *Earth and Planetary Science Letters*, vol. 24, pp. 107–116.
- Huguet, A., Francez, A., Jusselme, M. D., Fosse, C. & Derenne, S., 2014: A Climatic Chamber Experiment to test the Short-Term Effect of Increasing Temperature on Branched GDGT Distribution in Sphagnum Peat. *Organic Geochemistry*, vol. 73, pp. 109–112.

- IITM [2019]: *Warm Pool Expansion Wraps MJO*. Centre for Climate Change Research, Indian Institute of Tropical Meteorology (IITM). Web-page, <https://www.climate.rocksea.org/research/warm-pool-expansion-warps-mjo/>. Accessed, 2021-06-21.
- Immirzi, C. P., Maltby, E. & Clymo, R. S., 1992: *The global status of peatlands and their role in carbon cycling*. A report for friends of the earth by the wetland ecosystems research group, University of Exeter. Report No. 11, Friends of the Earth. London, pp. 145.
- Joosten, H., 2016: Changing Paradigms in the History of Tropical Peatland Research. In: Osaki, M. & Tsuji, N. *Tropical Peatland Ecosystems*. Springer Japan, Tokyo. pp. 33-45.
- Joosten, H. & Clarke, D., 2002: *Wise Use of Mires and Peatlands – Backgrounds and Principles, Including a Framework for Decision-Making*. International Mire Conservation Group/International Peat Society, Jyväskylä.
- Kaislahti Tillam, P., Holzkämper, S., Kuhry, P., Sannel, A. B. K., Loader, N. J & Robertson, I., 2010: Stable carbon and oxygen isotopes in Sphagnum fuscum peat from subarctic Canada: Implications for paleoclimate studies. *Chemical Geology*, vol. 270, pp. 216-226.
- Kaufman, D., McKay, N., Routson, C., Erb, M., Davis, B., Heiri, O., Jaccard, S., Tierney, J., Dätwyler, C., Axford, Y., Brüssel, T., Cartapanis, O. *et al.* 2020a: A global database of Holocene paleotemperature records. *Scientific Data* 7, article 115.
- Kaufman, D., McKay, N., Routson, C., Erb, M., Dätwyler, C., Sommer, P. S., Heiri, O. & Davis, B., 2020b: Holocene global mean surface temperature, a multi-method reconstruction approach. *Scientific Data* 7, article 201.
- Knappy C. S., Nunn C. E. M., Morgan H. W. & Keely B. J., 2011: The major lipid cores of the archaeon *Ignisphaera aggregans*: implications for the phylogeny and biosynthesis of glycerol monoalkyl glycerol tetraether isoprenoid lipids. *Extremophiles*, vol. 15(4), pp. 517–528.
- Kohn, M. J., 2010: Carbon isotope compositions of terrestrial C3 plants as indicators of (paleo)ecology and (paleo)climate. *Proceedings of the National Academy of Sciences of the USA*, vol. 107 (46), 19691–19695.
- Ku, H., Chen, Y., Chan, P., Liu, H. & Lin, C., 2007: Paleo-environmental evolution as revealed by analysis of organic carbon and nitrogen: A case of coastal Taipei Basin in Northern Taiwan. *Geochemical Journal*, vol. 41, pp. 111-120.
- Kuhnert, H., Kuhlmann, H., Mohtadi, M., Meggers, Baumann, K. & Pätzold, J., 2014: Holocene Tropical Western Indian Ocean Sea Surface Temperatures in Covariation with climatic Changes in the Indonesian Region. *Paleoceanography*, vol. 29, pp. 423-437.
- Lappalainen, E., 1996: *Global peat resources*. International Peat Society, Jyväskylä.
- Liu, Z., Zhu, J., Rosenthal, Y., Zhang, X., Otto-Bliesner, B. L., Timmermann, A., Smith, R.S., Lohmann, G., Zheng, W. & Elison Timm, O., 2014: The Holocene temperature conundrum. *PNAS of USA*, vol. 111 (34).

- Löwemark, L., Chen, H., Yang, T., Kylander, M., Yu, E., Hsu, Y., Lee, T., Song, S. & Jarvis, S., 2011: Normalizing XRF-scanner data: A cautionary note on the interpretation of high-resolution records from organic-rich lakes. *Journal of Asian Earth Sciences*, vol. 40, pp. 1250-1256.
- Mohtadi, M., Steinke, S., Lückge, A., Groenveld, J. & Hathorne, E. C., 2010a: Glacial to Holocene Surface Hydrography of the tropical Eastern Indian Ocean. *Earth and Planetary Science Letters*, vol. 292, pp. 89-97.
- Mohtadi, M., Lückge, A., Steinke, S., Groenveld, J. & Hebbeln, D., 2010b: Late Pleistocene surface and thermocline conditions of the eastern tropical Indian Ocean. *Quaternary Science Reviews*, vol. 29, pp. 887-896.
- Morley, R. J., 1982: A Palaeoecological Interpretation of a 10,000 Year Pollen record from Danau Padang, Central Sumatra, Indonesia. *Journal of Biogeography*, vol. 9 (2), pp. 151-190.
- Naafs, B. D. A., Gallego-Sala, A. V., Inglis, G. N. & Pancost, R. D., 2017b: Refining the Global Branched Glycerol Dialkyl Glycerol Tetraether (brGDGT) Soil Temperature Calibration. *Organic Geochemistry*, vol. 106, pp. 48-56.
- Naafs, B. D. A., Inglis, G.N., Blewett, J., McClymont, E.L., Lauretano, V., Xie, S., Evershed, R. P. & Pancost, R. D., 2019: The Potential of Biomarker Proxies to Trace Climate, Vegetation, and Biogeochemical processes in Peat - A Review. *Global and Planetary Science*, vol. 179, pp. 57-79.
- Naafs, B. D. A., Inglis, G. N., Zheng, Y., Amesbury, M. J., Biester, H., Bindler, R., Blewett, J., Burrows, M. A., del Castillo Torres, D., Chambers, F. M., Cohen, A. D., Evershed, R. P., Feakins, S. J., Gałka, M., Gallego-Sala, A., Gandois, L., Gray, D. M., Hatcher, P. G., Honorio Coronado, E. N., Hughes, P. D. M., Huguet, A., Könönen, M., Laggoun-Défarge, F., Lähteenoja, O., Lamentowicz, M., Marchant, R., McClymont, E., Pontevedra-Pombal, X., Ponton, C., Pourmand, A., Rizzuti, A. M., Rochefort, L., Schellekens, J., De Vleeschouwer, F. & Pancost, R. D., 2017a: Introducing Global Peat-specific Temperature and pH Calibrations based on brGDGT Bacterial Lipids. *Geochimica et Cosmochimica Acta*, vol. 208, pp. 285-301.
- Naafs, B. D. A., McComrick, D., Inglis, G. N. & Pancost, R. D., 2018: Archaeal and Bacterial H-GDGTs Are Bundant in Peat and their Relative Abundance is Positively Correlated with Temperature. *Geochimica et Cosmochimica Acta*, vol. 227, pp. 156-160.
- Newsome J, Flenley J. R., 1988: Late Quaternary vegetational history of the central highlands of Sumatra. II. Palaeopalynology and vegetational history. *Journal of Biogeography*, vol. 15 (4), pp. 555–578.
- Niedermeyer, E. M., Sessions, A. I., Feakins, S. J. & Mohtadi, M., 2014: Hydroclimate of the Western Indo-Pacific Warm pool during the Past 24,000 years. *PNAS of USA*, vol. 111 (26), pp. 9402-9406.

- NOAA, 2021: *Global Monthly Mean CO₂*, Global Monitoring Laboratory, National Oceanic and Atmospheric Administration (NOAA). Web-page, <https://gml.noaa.gov/ccgg/trends/global.html#global>. Accessed, 2021-07-06.
- Osaki, M., 2016: Preface. In: Osaki, M. & Tsuji, N. *Tropical Peatland Ecosystems*. Springer Japan, Tokyo.
- Osaki, M., Nursyamsi, D., Noor, M., Wahyunto & Segah, H., 2016: Peatland in Indonesia. In: Osaki, M. & Tsuji, N., *Tropical Peatland Ecosystems*. Springer Japan, Tokyo. pp. 49-57.
- Page, S., Rieley, J. & Banks, C., 2011: Global and regional importance of the tropical peatland carbon pool. *Global Change Biology*, vol 17, pp. 798–818.
- Page, S., Weiss, D., Wüst, R. A. J. & Riley, J., 2004: A Record of Late Pleistocene and Holocene Carbon Accumulation and Climate Change from an Equatorial Peat Bog (Kalimantan, Indonesia): Implications for Past, Present and Future Carbon Dynamics. *Journal of Quaternary Science*, vol. 19 (7), pp. 625-635.
- Page, S., Wüst, R. & Banks, C., 2010: Past and present carbon accumulation and loss in Southeast Asian peatlands. *PAGES News*, vol. 18 (1), pp. 25-27.
- Partin, J. W., Cobb, K. M., Adkins, J. F., Clark, B. & Fernandez, D. P., 2007: Millennial-scale trends in west Pacific warm pool hydrology since the Last Glacial Maximum. *Nature* vol. 449, 4pp. 52–455.
- Peterse, F., Nicol, G. W., Schouten, S. & Sinninghe Damsté, J. S., 2010: Influence of Soil pH on the Abundance and Distribution of Core and Intact Polar Lipid-Derived Branched GDGTs in Soil. *Organic Geochemistry*, vol. 41, pp. 1171–1175.
- Peterse, F., van der Meer, J., Schouten, S., Weijers, J. W. H., Fierer, N., Jackson, R. B., Kim, J.-H. & Sinninghe Damsté, J. S., 2012: Revised Calibration of the MBT–CBT Paleotemperature Proxy Based on Branched Tetraether Membrane Lipids in Surface Soils. *Geochimica et Cosmochimica Acta*, vol. 96, pp. 215–229.
- Potonié, H., 1909: Die Tropen-Sumpfflachmoor-Natur der Moore des produktiven Carbons. Nebst der Vegetationsschilderung eines rezenten tropischen Wald-Sumpfflachmoores durch Dr. S.H. Koorders. *Jahrbuch der Königlich Preussischen Geologischen Landesanstalt*, vol. 30, pp. 389–443.
- Raflus, R. U., Iskarni, P. & Legaya, N., 2018: Mitigation Policy of Flood Disaster in Sungai Penuh Town Province of Jambi, Indonesia. *Sumatra Journal of Disaster, Geography and Geography Education*, vol. 2 (1), pp. 8-15.
- Rattray, J. E. & Smittenberg, R. H., 2020: Separation of Branched and Isoprenoid Glycerol Dialkyl Glycerol Tetraether (GDGT) Isomers in Peat Soils and Marine Sediments Using Reverse Phase Chromatography. *Frontiers in Marine Science*, vol. 7, article 539601.
- Rieley, J. & Page, S., 2016: Tropical Peatland of the World. In: Osaki, M. & Tsuji, N. *Tropical Peatland Ecosystems*. Springer Japan, Tokyo. pp. 3-15.

- Rouessac F, Rouessac A. 2007: *Chemical Analysis – Modern Instrumentation Methods and Techniques*. (2nd edition) John Wiley & Sons, Ltd, West Sussex, pp. 3-372.
- Roxy, M. K., Dasgupta, P., McPhaden, M. J., Suematsu, T., Zhang, C. & Kim, D., 2019: Twofold Expansion of the Indo-Pacific Warm Pool Warps the MJO Life Cycle. *Nature*, vol. 575, pp. 647–651.
- Ruddiman, W. F., 2014: *Earth's climate – Past and Future*. (3rd edition) W. H. Freeman and Company, New York, pp. 60-65, 415-416.
- Russell, J. M., Vogel, H., Konecky, B. L., Bijaksana, S., Hunag, Y., Melles, M., Wattrus, N., Costa, K. & King, J. W., 2014: Glacial forcing of central Indonesian hydroclimate since 60,000 y B.P. *Proceedings of the National Academy of Sciences of the United States of America*, vol. 111 (14), pp. 5100-5105.
- Sadalmelik, 2007: *Topographic Map of Sumatra*. Image, Wikipedia. Web-page, https://commons.wikimedia.org/wiki/File:Sumatra_Topography.png. Accessed 2021-07-06.
- Schouten, S., Hopmans, E. C. & Sinninghe Damsté, J. S., 2013: The Organic Geochemistry of Glycerol Dialkyl Glycerol Tetraether Lipids – A Review. *Organic Geochemistry*, vol. 54, pp. 19-61.
- Setiawan, R. Y., Mohtadi, M., Southon, J., Groeneveld, J., Steinke, S. & Hebbeln, D., 2015: The Consequences of Opening the Sunda Strait on the Hydrography of the Eastern Tropical Indian Ocean. *Paleoceanography*, vol. 30 (10), pp. 1358– 1372.
- Sinninghe Damsté, J. S., Hopmans, E. C., Pancost, R. D., Schouten, S. & Geenevasen, J. A. J., 2000: Newly discovered non-isoprenoid glycerol dialkyl glycerol tetraether lipids in sediments. *Chemical Communications* (17), pp. 1683–1684.
- Sprintall, J., Wijffels, S., Molcard, R. & Jaya, I., 2010: Direct Evidence of the South Java Current System in Ombai Strait. *Dynamics of Atmospheres and Oceans*, vol. 50, pp. 140-156.
- Stuiver, M. & Polach, H. A., 1977: Discussion Reporting of ¹⁴C Data. *Radiocarbon*, vol. 19(3), pp. 355–363.
- Susanto, R. D., Gordon, A. L & Zheng, Q., 2001: Upwelling along the coasts of Java and Sumatra and its Relation to ENSO. *Geophysical Research Letters*, vol. 28 (8), pp. 1599-1602.
- Takada, M., Shimada, S. & Takahashi, H., 2016: Tropical Peat Formation. In: Osaki, M. & Tsuji, N. *Tropical Peatland Ecosystems*. Springer Japan, Tokyo. pp. 127-133.
- United Nations, Economic and Social Commission for Asia and the Pacific. *ESCAP Population Data Sheet 2019*.

- Weatherspark, [2017]: *Average Weather at Depati Parbo Airport*. Web-page, <https://weatherspark.com/y/149090/Average-Weather-at-Depati-Parbo-Airport-Indonesia-Year-Round>. Accessed, 2021-06-22.
- Weber, Y., de Jonge, C., Rijpstra, W. I. C., Hopmans, E. C., Stadnitskaia, A., Schubert, C. J., Lehmann, M. F., Sinninghe Damsté, J. S., Niemann, H., 2015: Identification and Carbon Isotope Composition of a Novel Branched GDGT Isomer in Lake Sediments - Evidence for Lacustrine brGDGT Production? *Geochimica et Cosmochimica Acta*, vol. 154, pp. 118–129.
- Weijers, J. W. H., Schouten, S., van den Donker, J. C., Hopmans, E. C. & Sinninghe Damsté, J. S., 2007: Environmental Controls on Bacterial Tetraether Membrane Lipid Distribution in Soils. *Geochimica et Cosmochimica Acta*, vol. 71, pp. 703–713.
- Weijers, J. W. H., Steinmann, P., Hopmans, E. C., Schouten, S. & Sinninghe Damsté, J. S., 2011: Bacterial Tetraether Membrane Lipids in Peat and Coal - Testing the MBT-CBT Temperature Proxy for Climate Reconstruction. *Organic Geochemistry*, Vol. 42, pp. 477–486.
- Weijers, J. W. H., Wiesenberg, G. L. B., Bol, R., Hopmans, E. C., Pancost & R. D., 2010: Carbon Isotopic Composition of Branched Tetraether Membrane Lipids in Soils Suggest a Rapid Turnover and a Heterotrophic Lifestyle of their Source Organism(s). *Biogeosciences*, vol. 7, pp. 2959–2973.
- Weiss, D., Shotyk, W., Rieley, J., Page, S., Gloor, M., Reese, S. & Martinez-Cortizas, A., 2002: The Geochemistry of Major and Selected Trace Elements in a Forested Peat Bog, Kalimantan, SE Asia, and its Implications for Past Atmospheric Dust Deposition. *Geochimica et Cosmochimica Acta*, vol. 66 (13), pp. 2307-2323.
- Wheeler, M. C. & McBride, J. L., 2012: Australian Monsoon. In: Lau, W. K. & Waliser, D. E., *Intraseasonal Variability in the Atmosphere-Ocean Climate System*. (2nd edition) Springer, Heidelberg. pp. 147-190.
- Xiao, H., Cheng, S., Mao, X., Huang, T, Hu, Z. & Liu, X., 2017: Characteristics of peat humification, magnetic susceptibility and trace elements of Hani peatland, northeastern China: paleoclimatic implications. *Atmospheric Science Letters*, vol. 18, pp. 140-150.
- Xu, J., Holbourn, A., Kuhnt, W., Jian, Z. & Kawamura, H., 2008: Changes in the thermocline structure of the Indonesian outflow during Terminations I and II. *Earth and Planetary Science Letters*, vol. 273, pp. 152–162.
- Yamoah, K. A., Chabangborn, A., Chawchai, S., Fritz, S., Löwemark, L., Kaboth, S., Reimer, P., Smittenberg, R. H., Wohlfarth, B., 2021: A muted El-Niño-like condition during late-MIS-3. *Quaternary Science Reviews*, vol. 254, 106782.
- Yang, H., Lü, X., Ding, W., Lei, Y., Dang, X. & Xie, S., 2015: The 6-methyl Branched Tetraethers Significantly Affect the Performance of the Methylation Index (MBT0) in Soils from an Altitudinal Transect at Mount Shennongjia. *Organic Geochemistry*, vol. 82, pp. 42–53.

Appendix A. GDGT Results

Table A1. Chromatographic peak-integrated areas from the first LC-MS analysis (run 1) of peat core RP-1A-REPA from Danau Padang, Sumatra, Indonesia.

Depth (cm)	Sample Name	Area isoGDGT-0 m/z 1302	Area IIIa, m/z 1050	Area IIIa', m/z 1050	Area IIIb, m/z 1048	Area IIa, m/z 1036	Area IIb, m/z 1034	Area IIc, m/z 1032	Area Ia, m/z 1022	Area Ib, m/z 1020	Area Ic, m/z 1018
10	P10	18817354	703011	2124090	739973	38609594	300795	119395	464622819	6465830	4081537
20	P20	25170520	442834	2437101	654310	17544892	328418	195246	421861660	17333800	10648629
30	P30	72852364	1297085	6041676	1024681	43670496	771555	257507	671997037	20708401	12789821
40	P40	76160795	2147386	8332901	1477487	64589888	1027230	434221	874557482	36529663	21611297
50	P50	57452102	1388623	5990183	1082133	46122811	814727	359199	702830303	26807814	15630332
60	P60	72506374	2177888	8555449	1432522	68543387	1242137	417096	873107396	30843985	18817868
70	P70	81881949	2614970	9382825	1259093	63391795	1193560	409209	938604020	27599868	17720862
80	P80	91049659	3046794	8701718	1304681	87703968	1130105	389110	969499124	22451403	15877171
90	P90	32426649	1365134	4658749	923122	41021592	547543	219428	455927388	10129145	6708008
100	P100	16990644	527990	1750445	350365	19126104	187653	87599	199622105	3752672	2380355
110	P110	18819938	715790	1870414	370257	21310318	180411	101182	212130515	3489266	2526228
120	P120	46208872	1412340	3789829	801013	38869288	502228	215649	489916506	10985135	6547722
130	P130	37559658	4978667	6717046	788635	102303049	529250	230010	540010951	5756861	3679324
140	P140	56801777	3268599	5706075	815080	81465957	1059291	228455	527576689	6114397	3524951
150	P150	75999207	2234656	6981316	1249415	72300592	716368	265017	795566254	10082566	8337320
160	P160	94637914	2618820	7098374	1120388	84567894	1064808	557517	660814693	13930110	11868414
170	P170	130079926	6229021	14943017	2118209	183669458	1727331	646100	1132375062	21639645	17439395
180	P180	127477234	3677887	12310964	2111090	139420930	1255536	396702	1246712653	16978294	11935757
190	P190	94588571	3788242	10127829	1459122	114304713	840451	345207	747372515	10430914	8472741
200	P200	48566649	2521208	5622177	897056	59834863	499433	179385	436886948	6537414	5152676
210	P210	89893379	4017649	8201746	1469908	82075977	834487	309329	803134868	18695350	10340093
220	P220	124719457	7043655	14215110	2000147	191656052	1330660	409669	1227826939	21400644	14564311
230	P230	124484405	4434019	10688933	1339300	103605130	975215	323783	805450880	13893091	8920384
240	P240	79335564	3740729	8897878	1157613	107882846	831358	211777	751052798	9163597	5922638
250	P250	50261881	2750979	6986843	957218	66965420	639900	183641	546595727	9906149	5159524
260	P260	91180273	11062406	13970860	1716744	200777519	1581292	497446	800664529	13394866	9796987
270	P270	47659883	6126767	8613377	901405	100717561	1388396	368009	547280035	13673650	6202085
280	P280	102326746	13212669	13384866	1446384	183200761	2586800	712570	830948217	17834376	9816520
290	P290	69518459	9014630	12708891	998315	144191862	1661085	468262	750158119	14467100	8038634
300	P300	108763972	9941554	11146516	1419633	162847371	1477030	505824	786693631	12980580	8802168
310	P310	82396814	5358197	9049407	1611214	170515661	1354842	463376	998139532	15691254	15196694
320	P320	66988242	2852202	5210861	971967	65669853	753658	493032	576908424	15629473	12972258
330	P330	59314923	1569483	3814932	720566	45373348	453163	169414	445204982	6841386	5427685
340	P340	58853267	1812727	4556459	888018	53270541	651366	281343	533527952	12376789	8747389
350	P350	83310256	4185710	6779978	1167127	100860188	1490718	728476	719025083	16236396	15008725
360	P360	35352844	2088717	4011705	637215	52986257	435416	212930	384594100	4615579	2936943
370	P370	100316105	3949330	7144850	1049735	95655035	1009221	523382	644400504	13471943	9591860

380	P380	118073015	5032743	7209786	1033627	95826726	1630486	618307	575368735	16712527	15558651
390	P390	84844825	4536049	8030638	1053971	93237131	1583318	650734	644608598	18810707	16451363
400	P400	114127039	5229126	8329621	1322451	101348419	1629653	573725	787493439	21140539	14184083
410	P410	75113071	3427188	5982538	868281	80496891	727871	377839	486169296	9197469	7759546
420	P420	84600708	3326073	6958193	975581	75344204	1043217	419416	531716981	11639721	9538729
430	P430	107520807	4056694	8071755	1216237	86708476	967984	510716	698907127	16445993	13116265
440	P440	97075563	6855425	10605095	1208991	126358059	2110200	536338	739592070	23992631	14812523
450	P450	103387281	6037153	10814401	1049247	110606182	1526791	489067	682382301	18611687	11581877
460	P460	68983648	4721916	6908077	760156	74162564	933007	382578	411532703	8689583	6752551
470	P470	97465738	5279519	8003116	974046	89280755	1310933	588931	537090958	12814220	9162594
480	P480	65613852	3662201	6119881	702458	62348369	913868	296958	448240412	8624229	5613935
490	P490	38161258	2543746	4983426	438594	41243699	876960	318794	269694180	7351509	4896406
500	P500	55236740	4719704	6464379	656150	65607997	1331536	609475	446354099	16520294	12615005
510	P510	54605629	2713256	4827204	514429	43324421	703237	277369	271684599	6646386	3936088
520	P520	66959263	4662849	7407981	647629	65376988	1488804	366871	420648629	10552788	7279729
530	P530	139713988	10910476	11878282	1261140	147915196	3129167	870143	764642302	30362914	17599101
540	P540	129063684	10421997	9093705	1080497	139336401	2425495	909453	643130578	23739572	17674302
550	P550	32550075	1349195	2463234	290320	22552626	1035087	90160	136737138	7288251	1890626
560	P560	78160140	6614908	8398230	1068103	97590492	3159682	673699	735774892	26625606	14769758
570	P570	52464189	7354550	7659386	692178	88169555	2262248	674833	453896557	22894273	12746027
580	P580	45136065	6285140	5476428	488627	77208714	1701744	642177	348171632	16283797	9480754
590	P590	88734834	13800649	11200807	966019	147037035	3296618	1178280	593120342	32959431	16091098
600	P600	136861028	32062111	18564001	1369220	278005034	6847333	1827576	1009768933	64121685	33298477

Table A2. Chromatographic peak-integrated areas from the second LC-MS analysis (run 2) of peat core RP-IA-REPA from Danau Padang, Sumatra, Indonesia.

Depth (cm)	Sample Name	Area isoGDGT-0 m/z 1302	Area IIIa, m/z 1050	Area IIIa', m/z 1050	Area IIIb, m/z 1048	Area IIa, m/z 1036	Area IIb, m/z 1034	Area IIc, m/z 1032	Area Ia, m/z 1022	Area Ib, m/z 1020	Area Ic, m/z 1018
10	P10	17558869	817248	2131112	680619	34506807	154901	76471	410580028	3649497	2634096
20	P20	25718231	440505	1868840	581522	14267522	267646	78930	318987382	12958986	7851218
30	P30	75765322	1133826	5287646	896981	37624086	445224	159020	529723670	18759788	11835174
40	P40	78962758	1538675	6937330	1125154	54491727	799648	266983	769338033	29855815	17566961
50	P50	54793748	1427625	5503168	866593	37097271	610247	217698	563161999	22336595	11035795
60	P60	3351183	46831	196705	80784	1502828	17006	15945	29548382	634540	419381
70	P70	88058196	2297752	8889088	1250367	56763426	911215	271397	732369229	26329702	15315883
80	P80	99855484	2586851	8945259	1155270	85407834	915952	264824	809880852	23984995	15675281
90	P90	53573600	1256788	4324755	701458	38503243	474888	146097	462391480	9787696	7017653
100	P100	20290611	560798	1700154	678696	18544244	172378	87194	208978965	3628540	2371319
110	P110	2493148	36586	128758	38938	1573922	15250	3110	18806563	216846	150683
120	P120	54536657	1465518	4347083	970776	43801312	432119	196195	532504611	11377276	7335288
130	P130	54098102	5059539	7565522	783343	107790872	553195	207783	520546311	5433354	3585332
140	P140	59140842	2827577	6187364	780086	76075182	1098036	200818	525309292	5748400	3434265

150	P150	7305466	85242	323805	85005	3354231	24966	16402	56333795	441599	292136
160	P160	105311370	2731735	7568938	1305181	88605893	1131278	489356	703000203	14081567	12586483
170	P170	172639665	6075029	14889719	2048453	191360632	1569387	555030	1240928807	23009525	17403600
180	P180	167936521	3580974	11768791	1976190	139710455	1154288	356741	1213416478	17469891	11912715
190	P190	122606008	3575256	10172537	1282063	109531749	846598	294020	819518759	8145398	6903812
200	P200	61996840	2165723	5563238	830391	60474566	415518	173603	463104884	5769766	5497680
210	P210	96814136	3994972	7575952	1402248	83243359	797651	247025	838208753	20605857	13171661
220	P220	149435038	6813406	13592162	2040966	184835843	1143295	312048	1128576444	19511776	15785181
230	P230	140169563	4645460	11399648	1532994	117564529	898559	307426	876863409	13656850	11117864
240	P240	123759506	4345197	10481210	1694250	126990674	769061	286439	915917714	9915290	5986939
250	P250	71826739	2761533	7602522	1426352	81819946	666156	224445	646370167	9799229	6346797
260	P260	140864665	11992643	17798557	1909556	226401721	1590221	425735	1139752010	15888237	12288419
270	P270	74994830	7233249	10039859	1489112	113909085	1474771	410882	666924390	16895439	7495452
280	P280	122646014	13991179	16046246	1880913	217021431	2211688	691886	1032676822	19306341	12753725
290	P290	99686876	9701245	13472329	1215973	151159050	1438886	511521	850398568	14349347	9966316
300	P300	125650536	11583500	13930275	1611400	179655444	1684961	578176	1000568598	12722113	10554982
310	P310	155489655	6124880	10837319	1940646	191548684	1585641	448299	1193919724	17904952	17002353
320	P320	113430807	3818876	6832921	1177733	68566657	841984	383174	681896482	15952344	14867931
330	P330	73541833	1636247	5199837	866241	50433716	453415	145413	497272176	6588002	6367220
340	P340	76025664	2254161	6080874	942548	63373685	695605	323844	689226392	12272281	10577221
350	P350	124116649	4934279	8589902	1347812	113426108	1449678	678959	815649110	18453840	18485807
360	P360	53276476	2330022	4390695	1182192	61503664	446231	224231	487038875	5257618	4082530
370	P370	121255340	5406504	8459543	1346360	112481070	1131266	513746	711501915	13054994	11754820
380	P380	137018832	6491571	8356886	1162104	104591922	1428160	713629	677654015	19660814	19338528
390	P390	121356601	5700791	8594582	1436779	114446926	1770931	732524	821143492	21434965	21697121
400	P400	140030608	5781082	10839105	1314050	105275789	1619750	541053	907669680	22533410	17272262
410	P410	105237551	3859220	6525872	1043185	86042671	700312	301065	556836425	10818254	8916074
420	P420	90598744	3592561	7875589	1183533	80192310	906688	462918	568126148	12457805	9853248
430	P430	171210737	4389478	9352172	1355113	105471006	926651	308322	768315168	16754162	13514158
440	P440	167026238	7547347	13197734	1516140	133753319	1864000	557404	890409702	28553198	18043126
450	P450	125250030	5979402	11827348	1165047	109441630	1398001	467973	687623121	21533337	11595717
460	P460	81263504	4559531	7845647	712221	75622046	1044890	354596	501708002	9981192	6948268
470	P470	128989858	5609081	8601179	931774	91425914	1313177	500150	517208744	12866957	9368866
480	P480	90347942	3162563	6041831	773832	62463913	828346	288199	459618719	9074976	5633238
490	P490	54142560	2899565	5346685	490689	43431155	839177	282841	322079900	8451854	5496797
500	P500	79085582	4210357	6159119	558172	68322719	1186703	487774	410586704	18741697	10795159
510	P510	52561263	2574349	4926356	634559	39409116	644679	252961	299999709	6398098	3412321
520	P520	73461177	3751681	6849721	596712	56797779	1020106	334911	366781045	10568884	6601031
530	P530										
540	P540	105655215	10897873	7642227	956964	129987143	1705719	625673	670174098	24491493	16678661
550	P550	37469791	1055624	1972093	232720	20307409	800121	92315	146963008	6502746	1607151
560	P560	93952825	6561975	7925783	845295	93682808	2429440	574032	707969898	24776658	15918156
570	P570	68920180	7220872	7435433	859478	82304325	2008423	688930	523657517	22347504	13369937
580	P580	56588852	6162161	6010535	623400	71445637	1570381	572308	351078925	17310489	8751712

590	P590	99480376	13036151	11792317	1269003	154785669	3005450	1155404	639426435	36718914	15852484
600	P600	164103608	32179891	14939676	1403597	271793628	5665877	2230983	1102387562	65156988	36209880

Table A3. Chromatographic peak-integrated areas from the third LC-MS analysis (run 3) of peat core RP-IA-REPA from Danau Padang, Sumatra, Indonesia.

Depth (cm)	Sample Name	Area isoGDGT-0 m/z 1302	Area IIIa, m/z 1050	Area IIIa', m/z 1050	Area IIIb, m/z 1048	Area IIa, m/z 1036	Area IIb, m/z 1034	Area IIc, m/z 1032	Area Ia, m/z 1022	Area Ib, m/z 1020	Area Ic, m/z 1018
10	P10	40648203	838949	2613094	1478905	39043157	214456	113204	510305163	5913638	3783464
20	P20	46738751	483343	2459417	883399	18832772	297644	130281	499522775	18608544	10624742
30	P30	114155799	1190070	5790902	1481334	41650781	670425	285784	725271672	20594433	13044754
40	P40	103312938	1539961	8455888	1782371	56869682	1125125	247865	881422701	32296195	19108283
50	P50	79379344	1408198	5872035	1433982	43727900	712027	252906	714292901	26499298	14944064
60	P60	109342584	2193432	9246400	1758257	69020641	1002293	310286	988969439	31407829	16106325
70	P70	121726197	2469719	9576685	1701653	63061038	1259763	337370	898911040	28196663	18711069
80	P80	129400403	2874684	8896037	1884236	85210880	978843	273990	843655241	21337995	15479796
90	P90	63934911	1365299	3954368	982418	36147961	464323	151001	497156455	9793263	7236440
100	P100	18416200	463590	1328946	328483	15169443	134658	75514	189613603	2445286	1738370
110	P110	23516206	596101	1827180	361441	20130251	173063	82780	215138981	2863106	1960772
120	P120	46019478	1063414	3423948	742507	26864521	338415	123752	418809893	8146240	5193714
130	P130	57717448	4442346	7100731	1116495	99217948	505423	181005	563398397	6158522	3389181
140	P140	49714988	2813276	5044688	927934	71861732	927630	181799	552920362	6234883	3113775
150	P150	121117410	2144782	7872263	2155969	70658664	803285	217947	834174277	8963753	6935425

Table A4. MBT'5me index (De Jonge et al. 2014) calculated for the three analytical replications (Run 1, 2, and 3, respectively) of peat core RP-IA-REPA from Danau Padang, Sumatra, Indonesia. SD=standard deviation, CV=coefficient of variation).

Depth (cm)	Sample Name	MBT'5me Run 1	MBT'5me Run 2	MBT'5me Run 3	Average MBT'5me	SD MBT'5me	CV (%) MBT'5me
10	P10	0.92	0.92	0.93	0.92	0.0036	0.39
20	P20	0.96	0.96	0.96	0.96	0.0032	0.34
30	P30	0.94	0.93	0.95	0.94	0.0056	0.59
40	P40	0.93	0.93	0.94	0.94	0.0040	0.43
50	P50	0.94	0.94	0.94	0.94	0.0024	0.25
60	P60	0.93	0.95	0.93	0.94	0.0121	1.29
70	P70	0.94	0.93	0.93	0.93	0.0041	0.44
80	P80	0.92	0.91	0.91	0.91	0.0058	0.63

90	P90	0.92	0.92	0.93	0.92	0.0073	0.80
100	P100	0.91	0.92	0.92	0.92	0.0064	0.70
110	P110	0.91	0.92	0.91	0.91	0.0073	0.80
120	P120	0.93	0.92	0.94	0.93	0.0082	0.89
130	P130	0.84	0.82	0.85	0.83	0.0113	1.35
140	P140	0.86	0.87	0.88	0.87	0.0097	1.11
150	P150	0.92	0.94	0.92	0.93	0.0146	1.58
160	P160	0.89	0.89		0.89	0.0011	0.12
170	P170	0.86	0.87		0.86	0.0044	0.51
180	P180	0.90	0.90		0.90	0.0017	0.19
190	P190	0.87	0.88		0.87	0.0101	1.16
200	P200	0.88	0.88		0.88	0.0040	0.45
210	P210	0.91	0.91		0.91	0.0021	0.23
220	P220	0.86	0.86		0.86	0.0038	0.44
230	P230	0.88	0.88		0.88	0.0027	0.30
240	P240	0.87	0.88		0.87	0.0027	0.31
250	P250	0.89	0.89		0.89	0.0019	0.21
260	P260	0.79	0.83		0.81	0.0251	3.09
270	P270	0.84	0.85		0.84	0.0068	0.81
280	P280	0.81	0.82		0.82	0.0061	0.74
290	P290	0.83	0.84		0.84	0.0074	0.88
300	P300	0.82	0.84		0.83	0.0133	1.60
310	P310	0.85	0.86		0.86	0.0053	0.62
320	P320	0.90	0.91		0.90	0.0069	0.76
330	P330	0.91	0.91		0.91	0.0004	0.05
340	P340	0.91	0.91		0.91	0.0043	0.48
350	P350	0.87	0.88		0.88	0.0009	0.10
360	P360	0.88	0.88		0.88	0.0067	0.76
370	P370	0.87	0.86		0.86	0.0057	0.66
380	P380	0.85	0.86		0.86	0.0061	0.71
390	P390	0.87	0.88		0.87	0.0028	0.32
400	P400	0.88	0.89		0.89	0.0071	0.80
410	P410	0.86	0.86		0.86	0.0059	0.69
420	P420	0.87	0.87		0.87	0.0004	0.04
430	P430	0.89	0.88		0.88	0.0069	0.78
440	P440	0.85	0.87		0.86	0.0110	1.29
450	P450	0.86	0.86		0.86	0.0020	0.23
460	P460	0.84	0.86		0.85	0.0157	1.84
470	P470	0.85	0.85		0.85	0.0055	0.64
480	P480	0.87	0.88		0.87	0.0025	0.29
490	P490	0.86	0.88		0.87	0.0098	1.13
500	P500	0.87	0.86		0.86	0.0087	1.01
510	P510	0.86	0.88		0.87	0.0150	1.73
520	P520	0.86	0.86		0.86	0.0014	0.17

530	P530	0.83			0.83		
540	P540	0.82	0.83		0.82	0.0107	1.30
550	P550	0.85	0.87		0.86	0.0148	1.71
560	P560	0.88	0.88		0.88	0.0006	0.07
570	P570	0.83	0.86		0.85	0.0183	2.17
580	P580	0.81	0.83		0.82	0.0086	1.05
590	P590	0.80	0.80		0.80	0.0040	0.50
600	P600	0.78	0.79		0.79	0.0126	1.60
Mean					0.88	0.0068	0.78

Table A5. CBTpeat index (Naafs et al. 2017a) calculated for the three analytical replications (Run 1, 2, and 3, respectively) of peat core RP-1A-REPA from Danau Padang, Sumatra, Indonesia. SD=standard deviation, CV=coefficient of variation).

Depth (cm)	Sample Name	CBTpeat Run 1	CBTpeat Run 2	CBTpeat Run 3	Average CBTpeat	SD CBT	CV (%) CBT
10	P10	-1.75	-1.88	-1.80	-1.81	0.0618	3.42
20	P20	-1.34	-1.34	-1.39	-1.36	0.0249	1.84
30	P30	-1.42	-1.37	-1.45	-1.41	0.0439	3.11
40	P40	-1.31	-1.34	-1.35	-1.33	0.0204	1.53
50	P50	-1.35	-1.33	-1.36	-1.34	0.0181	1.35
60	P60	-1.37	-1.56	-1.41	-1.45	0.1049	7.26
70	P70	-1.42	-1.34	-1.39	-1.38	0.0405	2.92
80	P80	-1.52	-1.42	-1.47	-1.47	0.0464	3.16
90	P90	-1.51	-1.54	-1.58	-1.54	0.0321	2.08
100	P100	-1.59	-1.62	-1.72	-1.64	0.0702	4.28
110	P110	-1.63	-1.75	-1.69	-1.69	0.0634	3.75
120	P120	-1.54	-1.55	-1.57	-1.56	0.0170	1.10
130	P130	-1.70	-1.67	-1.69	-1.68	0.0137	0.82
140	P140	-1.68	-1.67	-1.71	-1.68	0.0234	1.39
150	P150	-1.69	-1.88	-1.71	-1.76	0.1035	5.88
160	P160	-1.53	-1.54		-1.54	0.0090	0.59
170	P170	-1.54	-1.56		-1.55	0.0167	1.08
180	P180	-1.66	-1.65		-1.65	0.0059	0.36
190	P190	-1.61	-1.69		-1.65	0.0568	3.45
200	P200	-1.60	-1.65		-1.62	0.0388	2.39
210	P210	-1.51	-1.50		-1.51	0.0013	0.08
220	P220	-1.59	-1.59		-1.59	0.0005	0.03
230	P230	-1.55	-1.59		-1.57	0.0228	1.45
240	P240	-1.66	-1.69		-1.68	0.0247	1.47
250	P250	-1.55	-1.61		-1.58	0.0432	2.74
260	P260	-1.54	-1.59		-1.57	0.0339	2.17
270	P270	-1.44	-1.44		-1.44	0.0012	0.08
280	P280	-1.48	-1.53		-1.50	0.0312	2.07

290	P290	-1.50	-1.54		-1.52	0.0302	1.99
300	P300	-1.57	-1.62		-1.60	0.0354	2.22
310	P310	-1.65	-1.66		-1.66	0.0061	0.37
320	P320	-1.48	-1.50		-1.49	0.0202	1.36
330	P330	-1.65	-1.65		-1.65	0.0040	0.24
340	P340	-1.52	-1.60		-1.56	0.0518	3.32
350	P350	-1.53	-1.52		-1.52	0.0078	0.51
360	P360	-1.69	-1.74		-1.71	0.0361	2.11
370	P370	-1.54	-1.56		-1.55	0.0192	1.24
380	P380	-1.42	-1.43		-1.43	0.0037	0.26
390	P390	-1.42	-1.47		-1.44	0.0384	2.66
400	P400	-1.46	-1.46		-1.46	0.0039	0.26
410	P410	-1.55	-1.55		-1.55	0.0000	0.00
420	P420	-1.49	-1.49		-1.49	0.0038	0.26
430	P430	-1.49	-1.51		-1.50	0.0145	0.97
440	P440	-1.38	-1.37		-1.38	0.0016	0.11
450	P450	-1.41	-1.36		-1.39	0.0341	2.46
460	P460	-1.47	-1.49		-1.48	0.0118	0.80
470	P470	-1.46	-1.43		-1.44	0.0175	1.21
480	P480	-1.52	-1.52		-1.52	0.0009	0.06
490	P490	-1.38	-1.40		-1.39	0.0181	1.30
500	P500	-1.33	-1.27		-1.30	0.0422	3.25
510	P510	-1.42	-1.46		-1.44	0.0279	1.94
520	P520	-1.40	-1.37		-1.38	0.0261	1.88
530	P530	-1.31			-1.31		
540	P540	-1.35	-1.38		-1.37	0.0196	1.43
550	P550	-1.17	-1.26		-1.22	0.0607	4.99
560	P560	-1.34	-1.36		-1.35	0.0137	1.02
570	P570	-1.22	-1.29		-1.25	0.0435	3.46
580	P580	-1.26	-1.24		-1.25	0.0203	1.62
590	P590	-1.20	-1.20		-1.20	0.0042	0.35
600	P600	-1.17	-1.21		-1.19	0.0327	2.75
Mean					-1.49	0.0275	1.83

Table A6. Ratio of isoGDGTs-0 to brGDGTs calculated for the three analytical replications (Run 1, 2, and 3, respectively) of peat core RP-1A-REPA from Danau Padang, Sumatra, Indonesia. SD=standard deviation, CV=coefficient of variation).

Depth (cm)	Sample Name	GDGT-0/brGDGTs Run 1	GDGT-0/brGDGTs Run 2	GDGT-0/brGDGTs Run 3	Average GDGT-0/brGDGTs	SD GDGT-0/brGDGTs	CV (%) GDGT-0/brGDGTs
10	P10	3.63	3.86	7.20	4.90	1.999	40.82
20	P20	5.34	7.20	8.47	7.00	1.574	22.49

30	P30	9.60	12.51	14.09	12.07	2.277	18.87
40	P40	7.54	8.95	10.30	8.93	1.383	15.49
50	P50	7.17	8.53	9.81	8.50	1.319	15.51
60	P60	7.21	10.32	9.76	9.10	1.657	18.21
70	P70	7.71	10.43	11.88	10.01	2.120	21.18
80	P80	8.20	10.52	13.20	10.64	2.499	23.49
90	P90	6.22	10.21	11.47	9.30	2.744	29.50
100	P100	7.46	8.57	8.72	8.25	0.688	8.34
110	P110	7.75	11.89	9.67	9.77	2.069	21.17
120	P120	8.36	9.05	9.90	9.10	0.775	8.51
130	P130	5.65	8.30	8.42	7.46	1.568	21.02
140	P140	9.02	9.51	7.72	8.75	0.927	10.59
150	P150	8.47	11.98	12.97	11.14	2.367	21.25
160	P160	12.08	12.67		12.37	0.416	3.36
170	P170	9.42	11.53		10.47	1.489	14.21
180	P180	8.88	11.98		10.43	2.192	21.00
190	P190	10.54	12.77		11.66	1.573	13.50
200	P200	9.37	11.40		10.39	1.431	13.78
210	P210	9.68	9.99		9.83	0.221	2.25
220	P220	8.42	10.89		9.66	1.741	18.03
230	P230	13.11	13.50		13.31	0.279	2.10
240	P240	8.93	11.50		10.21	1.819	17.81
250	P250	7.85	9.49		8.67	1.157	13.35
260	P260	8.66	9.86		9.26	0.855	9.23
270	P270	6.95	9.08		8.02	1.503	18.75
280	P280	9.54	9.32		9.43	0.155	1.65
290	P290	7.38	9.47		8.43	1.479	17.55
300	P300	10.92	10.19		10.56	0.517	4.89
310	P310	6.77	10.79		8.78	2.842	32.38
320	P320	9.83	14.28		12.05	3.147	26.10
330	P330	11.64	12.93		12.28	0.909	7.40
340	P340	9.55	9.68		9.61	0.087	0.91
350	P350	9.63	12.63		11.13	2.121	19.07
360	P360	7.81	9.41		8.61	1.126	13.08
370	P370	12.91	14.01		13.46	0.773	5.74
380	P380	16.42	16.32		16.37	0.070	0.43
390	P390	10.75	12.17		11.46	1.003	8.75
400	P400	12.13	13.05		12.59	0.656	5.21
410	P410	12.62	15.59		14.11	2.097	14.87
420	P420	13.20	13.23		13.22	0.024	0.18
430	P430	12.95	18.60		15.78	3.994	25.31
440	P440	10.48	15.25		12.86	3.369	26.19
450	P450	12.26	14.72		13.49	1.736	12.87
460	P460	13.40	13.35		13.37	0.036	0.27

470	P470	14.67	19.91		17.29	3.708	21.45
480	P480	12.23	16.49		14.36	3.013	20.98
490	P490	11.48	13.91		12.69	1.714	13.51
500	P500	9.95	15.18		12.57	3.694	29.39
510	P510	16.32	14.67		15.49	1.164	7.51
520	P520	12.92	16.21		14.56	2.326	15.98
530	P530	14.13			14.13		
540	P540	15.22	12.24		13.73	2.109	15.36
550	P550	18.74	20.87		19.81	1.507	7.61
560	P560	8.74	10.92		9.83	1.541	15.69
570	P570	8.80	10.44		9.62	1.164	12.10
580	P580	9.69	12.21		10.95	1.780	16.25
590	P590	10.83	11.34		11.08	0.365	3.30
600	P600	9.47	10.71		10.09	0.881	8.73
Mean					11.22	1.555	14.24

Table A7. IR6me (Yang et al. 2015) and IBT (Ding et al. 2015) indices calculated for the three analytical replications (Run 1, 2, and 3, respectively) of peat core RP-1A-REPA from Danau Padang, Sumatra, Indonesia.

Depth (cm)	Sample Name	IR6me Run 1	IR6me Run 2	IR6me Run 3	Average IR6me	IBT Run 1	IBT Run 2	IBT Run 3	Average IBT
10	P10	0.07	0.07	0.09	0.08	1.27	1.22	1.18	1.22
20	P20	0.14	0.14	0.14	0.14	0.87	0.90	0.90	0.89
30	P30	0.13	0.14	0.14	0.14	0.87	0.87	0.87	0.87
40	P40	0.13	0.12	0.15	0.13	0.90	0.91	0.84	0.88
50	P50	0.13	0.14	0.14	0.13	0.90	0.85	0.89	0.88
60	P60	0.12	0.15	0.13	0.13	0.92	0.90	0.89	0.90
70	P70	0.14	0.14	0.14	0.14	0.85	0.82	0.84	0.83
80	P80	0.10	0.10	0.11	0.10	1.02	0.99	1.00	1.00
90	P90	0.11	0.11	0.11	0.11	0.96	0.96	0.98	0.97
100	P100	0.10	0.11	0.09	0.10	1.05	1.05	1.07	1.06
110	P110	0.09	0.09	0.09	0.09	1.07	1.10	1.05	1.07
120	P120	0.10	0.10	0.13	0.11	1.03	1.02	0.91	0.99
130	P130	0.06	0.07	0.07	0.07	1.20	1.17	1.16	1.18
140	P140	0.07	0.08	0.07	0.07	1.17	1.11	1.17	1.15
150	P150	0.10	0.11	0.12	0.11	1.03	1.03	0.97	1.01
160	P160	0.08	0.09		0.09	1.09	1.08		1.09
170	P170	0.08	0.08		0.08	1.10	1.12		1.11
180	P180	0.09	0.09		0.09	1.07	1.09		1.08
190	P190	0.09	0.09		0.09	1.07	1.05		1.06
200	P200	0.09	0.09		0.09	1.04	1.05		1.05
210	P210	0.10	0.09		0.10	1.02	1.06		1.04
220	P220	0.07	0.07		0.07	1.15	1.15		1.15

230	P230	0.10	0.09		0.10	1.00	1.03		1.02
240	P240	0.08	0.08		0.08	1.10	1.10		1.10
250	P250	0.10	0.10		0.10	1.00	1.05		1.02
260	P260	0.07	0.08		0.07	1.18	1.13		1.15
270	P270	0.08	0.09		0.08	1.09	1.08		1.09
280	P280	0.07	0.07		0.07	1.17	1.16		1.16
290	P290	0.08	0.08		0.08	1.08	1.08		1.08
300	P300	0.07	0.07		0.07	1.19	1.14		1.16
310	P310	0.06	0.06		0.06	1.29	1.26		1.27
320	P320	0.08	0.10		0.09	1.12	1.03		1.07
330	P330	0.09	0.10		0.10	1.09	1.00		1.05
340	P340	0.09	0.10		0.09	1.08	1.03		1.06
350	P350	0.07	0.08		0.07	1.19	1.14		1.16
360	P360	0.08	0.08		0.08	1.14	1.16		1.15
370	P370	0.07	0.08		0.08	1.14	1.14		1.14
380	P380	0.07	0.08		0.08	1.15	1.12		1.13
390	P390	0.08	0.08		0.08	1.09	1.15		1.12
400	P400	0.08	0.10		0.09	1.11	1.01		1.06
410	P410	0.07	0.08		0.08	1.15	1.14		1.14
420	P420	0.09	0.10		0.09	1.05	1.03		1.04
430	P430	0.09	0.09		0.09	1.05	1.07		1.06
440	P440	0.08	0.09		0.09	1.10	1.03		1.06
450	P450	0.09	0.10		0.10	1.03	0.99		1.01
460	P460	0.09	0.09		0.09	1.06	1.01		1.03
470	P470	0.09	0.09		0.09	1.07	1.05		1.06
480	P480	0.09	0.09		0.09	1.03	1.04		1.03
490	P490	0.11	0.11		0.11	0.94	0.94		0.94
500	P500	0.09	0.08		0.09	1.04	1.07		1.05
510	P510	0.10	0.11		0.11	0.98	0.93		0.95
520	P520	0.10	0.11		0.10	0.98	0.95		0.96
530	P530	0.07			0.07	1.13			1.13
540	P540	0.06	0.06		0.06	1.22	1.27		1.24
550	P550	0.10	0.09		0.09	0.99	1.03		1.01
560	P560	0.08	0.08		0.08	1.09	1.10		1.10
570	P570	0.08	0.08		0.08	1.10	1.08		1.09
580	P580	0.06	0.08		0.07	1.18	1.11		1.15
590	P590	0.07	0.07		0.07	1.16	1.15		1.16
600	P600	0.06	0.05		0.05	1.22	1.31		1.27
Mean					0.09				1.07

Table A8. Relative abundances (averaged from replicate analysis) of brGDGTs in peat core RP-1A-REPA from Danau Padang, Sumatra, Indonesia.

Depth (cm)	Sample Name	IIIa (%)	IIIa' (%)	IIIb' (%)	IIa (%)	IIb (%)	IIc (%)	Ia (%)	Ib (%)	Ic (%)
10	P10	0.155	0.447	0.185	7.319	0.043	0.020	90.119	1.033	0.679
20	P20	0.102	0.495	0.154	3.709	0.066	0.029	89.759	3.559	2.127
30	P30	0.168	0.795	0.155	5.703	0.086	0.032	88.521	2.790	1.750
40	P40	0.180	0.818	0.150	6.080	0.101	0.033	87.219	3.407	2.012
50	P50	0.190	0.777	0.149	5.646	0.095	0.037	87.901	3.366	1.839
60	P60	0.186	0.761	0.183	5.870	0.088	0.039	88.729	2.609	1.534
70	P70	0.253	0.957	0.144	6.282	0.114	0.035	87.621	2.823	1.770
80	P80	0.280	0.878	0.144	8.531	0.099	0.030	86.242	2.242	1.554
90	P90	0.249	0.809	0.162	7.231	0.093	0.032	88.261	1.855	1.308
100	P100	0.229	0.705	0.199	7.803	0.073	0.037	88.551	1.446	0.956
110	P110	0.238	0.712	0.162	8.189	0.073	0.030	88.524	1.216	0.855
120	P120	0.242	0.715	0.155	6.693	0.078	0.033	89.034	1.876	1.173
130	P130	0.724	1.069	0.134	15.467	0.079	0.031	81.096	0.866	0.533
140	P140	0.470	0.895	0.133	12.111	0.163	0.032	84.710	0.955	0.532
150	P150	0.206	0.717	0.170	7.041	0.069	0.027	90.118	0.936	0.717
160	P160	0.331	0.908	0.150	10.724	0.136	0.065	84.436	1.736	1.514
170	P170	0.428	1.038	0.145	13.039	0.115	0.042	82.429	1.552	1.212
180	P180	0.256	0.849	0.144	9.843	0.085	0.027	86.740	1.215	0.841
190	P190	0.397	1.094	0.148	12.074	0.091	0.035	84.324	1.005	0.832
200	P200	0.442	1.054	0.163	11.332	0.086	0.033	84.725	1.161	1.003
210	P210	0.422	0.832	0.151	8.711	0.086	0.029	86.462	2.069	1.236
220	P220	0.486	0.975	0.142	13.206	0.087	0.025	82.579	1.434	1.067
230	P230	0.457	1.112	0.144	11.118	0.095	0.032	84.647	1.389	1.005
240	P240	0.412	0.987	0.144	11.968	0.082	0.025	84.794	0.976	0.611
250	P250	0.397	1.048	0.169	10.635	0.094	0.029	85.385	1.421	0.822
260	P260	0.945	1.286	0.148	17.456	0.131	0.039	77.908	1.192	0.895
270	P270	0.885	1.236	0.156	14.245	0.191	0.052	80.309	2.021	0.906
280	P280	1.147	1.233	0.139	16.778	0.205	0.059	77.934	1.564	0.942
290	P290	0.940	1.315	0.111	14.839	0.157	0.049	80.240	1.450	0.900
300	P300	0.969	1.125	0.137	15.463	0.142	0.049	80.078	1.168	0.870
310	P310	0.433	0.748	0.133	13.648	0.111	0.035	82.413	1.266	1.214
320	P320	0.450	0.812	0.145	9.134	0.108	0.060	85.251	2.151	1.888
330	P330	0.298	0.831	0.147	8.884	0.084	0.029	87.384	1.250	1.092
340	P340	0.291	0.757	0.132	8.356	0.097	0.043	87.156	1.785	1.383
350	P350	0.493	0.829	0.136	11.596	0.160	0.077	83.026	1.877	1.807
360	P360	0.436	0.831	0.175	11.283	0.087	0.043	85.485	0.974	0.685
370	P370	0.566	0.949	0.145	12.654	0.130	0.063	82.574	1.621	1.296
380	P380	0.737	0.999	0.141	12.894	0.198	0.086	80.378	2.333	2.234
390	P390	0.573	0.940	0.139	11.649	0.189	0.078	82.034	2.267	2.131
400	P400	0.547	0.948	0.131	10.290	0.162	0.056	84.134	2.173	1.558

410	P410	0.574	0.986	0.150	13.137	0.113	0.054	82.099	1.574	1.312
420	P420	0.522	1.118	0.163	11.734	0.148	0.067	82.968	1.818	1.464
430	P430	0.483	0.994	0.147	10.953	0.109	0.048	83.842	1.901	1.524
440	P440	0.715	1.175	0.134	12.927	0.199	0.054	80.573	2.599	1.623
450	P450	0.709	1.336	0.131	12.989	0.173	0.056	80.868	2.369	1.368
460	P460	0.833	1.315	0.132	13.413	0.176	0.066	81.173	1.664	1.226
470	P470	0.830	1.266	0.145	13.774	0.200	0.083	80.332	1.957	1.413
480	P480	0.630	1.122	0.136	11.511	0.161	0.054	83.718	1.632	1.037
490	P490	0.755	1.436	0.129	11.783	0.240	0.084	81.939	2.191	1.443
500	P500	0.829	1.174	0.113	12.468	0.234	0.102	79.621	3.287	2.173
510	P510	0.765	1.409	0.165	11.974	0.195	0.077	82.465	1.886	1.064
520	P520	0.864	1.470	0.128	12.570	0.256	0.072	81.026	2.184	1.430
530	P530	1.104	1.202	0.128	14.963	0.317	0.088	77.348	3.071	1.780
540	P540	1.246	0.979	0.119	15.747	0.242	0.090	76.750	2.819	2.008
550	P550	0.682	1.258	0.148	12.148	0.521	0.052	80.290	3.909	0.992
560	P560	0.751	0.930	0.109	10.896	0.318	0.071	82.248	2.927	1.750
570	P570	1.164	1.206	0.123	13.629	0.342	0.109	77.734	3.613	2.082
580	P580	1.339	1.236	0.120	15.996	0.352	0.131	75.249	3.615	1.962
590	P590	1.585	1.356	0.131	17.794	0.372	0.138	72.635	4.104	1.885
600	P600	2.159	1.130	0.093	18.485	0.422	0.136	70.899	4.344	2.333
Mean		0.603	1.006	0.144	11.406	0.159	0.054	83.217	2.058	1.353

Relative Abundances of *br*GDGTs

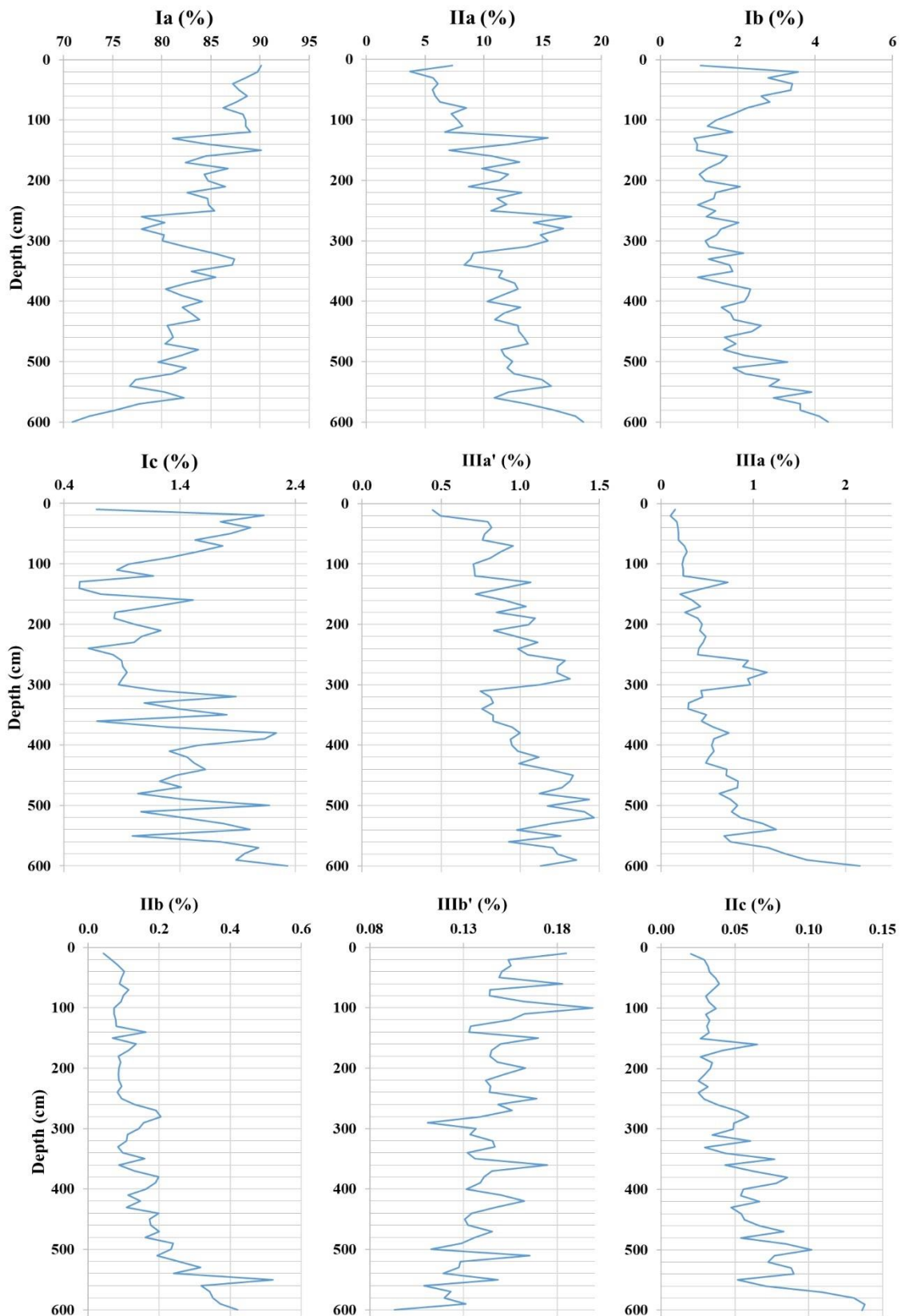


Figure A1. Relative abundances (%) of the different *br*GDGTs identified in peat core RP-1A-REPA, from Danau Padang, Sumatra, Indonesia.

Table A9. Chromatographic peak-integrated areas from the first LC-MS analysis, relative abundances (averaged from replicate analysis) of H-brGDGTs, ratio of H-brGDGTs to regular-brGDGTs, and H-MBTacyclic (Naafs et al. 2018) from peat core RP-1A-REPA, from Danau Padang, Sumatra, Indonesia.

Depth (cm)	Sample Name	Area H-1020 (H-Ia)	Area H-1034 (H-IIa)	Area H-1048 (H-IIIa)	Relative Abundance H-1020 (H-Ia) (%)	Relative Abundance H-1034 (H-IIa) (%)	Relative Abundance H-1048 (H-IIIa) (%)	H-brGDGTs/Regular brGDGTs (%)	H-MBTacyclic
10	P10	46117878	4266965	167179	91.23	8.44	0.33	10.03	0.91
20	P20	60692294	4331706	237376	93.00	6.64	0.36	14.84	0.93
30	P30	82577990	8393275	420028	90.36	9.18	0.46	12.75	0.90
40	P40	107290704	13163425	594561	88.63	10.87	0.49	12.86	0.89
50	P50	81320098	8705606	466919	89.86	9.62	0.52	12.06	0.90
60	P60	90486844	11480965	640319	88.19	11.19	0.62	10.87	0.88
70	P70	107579707	12427723	555229	89.23	10.31	0.46	12.00	0.89
80	P80	92540408	12840191	591767	87.33	12.12	0.56	10.00	0.87
90	P90	47728958	5860420	297882	88.57	10.88	0.55	10.81	0.89
100	P100	14829895	2512647	112424	84.96	14.40	0.64	7.96	0.85
110	P110	16368720	2807157	122310	84.82	14.55	0.63	8.24	0.85
120	P120	42225536	5203275	269207	88.53	10.91	0.56	9.00	0.89
130	P130	40598823	12056185	640264	76.18	22.62	1.20	8.23	0.76
140	P140	35129549	8098918	660587	80.04	18.45	1.51	7.17	0.80
150	P150	74358548	10778372	435787	86.90	12.60	0.51	9.83	0.87
160	P160	62315799	12232438	594860	82.93	16.28	0.79	10.05	0.83
170	P170	107457554	21934166	1137703	82.32	16.80	0.87	9.87	0.82
180	P180	101409459	14319621	740419	87.07	12.29	0.64	8.38	0.87
190	P190	52898280	12517078	659733	80.06	18.94	1.00	7.63	0.80
200	P200	45887877	8801703	435984	83.24	15.97	0.79	11.04	0.83
210	P210	61328854	11516338	476406	83.64	15.71	0.65	8.25	0.84
220	P220	91585767	19472158	908798	81.80	17.39	0.81	7.85	0.82
230	P230	76071862	12534686	744583	85.14	14.03	0.83	9.78	0.85
240	P240	55844460	11077837	598397	82.71	16.41	0.89	7.83	0.83
250	P250	47119370	8321962	422804	84.35	14.90	0.76	9.06	0.84
260	P260	57127043	18447896	2377223	73.28	23.67	3.05	7.70	0.73
270	P270	49033277	14964453	988420	75.45	23.03	1.52	9.93	0.75
280	P280	57258487	18456153	1473135	74.18	23.91	1.91	7.51	0.74
290	P290	51670762	17362101	1176485	73.60	24.73	1.68	7.77	0.74
300	P300	60877560	15564772	1043267	78.57	20.09	1.35	8.08	0.79
310	P310	67353540	14499216	661832	81.63	17.57	0.80	7.03	0.82
320	P320	71508276	11912884	447524	85.26	14.20	0.53	12.99	0.85
330	P330	46342639	6667596	261636	86.99	12.52	0.49	10.82	0.87
340	P340	46436724	6033776	208300	88.15	11.45	0.40	8.95	0.88
350	P350	63072213	10993663	588379	84.49	14.73	0.79	9.06	0.84
360	P360	43520830	8287202	335514	83.46	15.89	0.64	11.86	0.83
370	P370	53116910	15342267	723920	76.78	22.18	1.05	9.30	0.77
380	P380	80251923	15004344	857550	83.50	15.61	0.89	14.21	0.83
390	P390	78878659	15450703	753663	82.96	16.25	0.79	12.81	0.83

400	P400	90657619	14379399	774204	85.68	13.59	0.73	11.83	0.86
410	P410	58098392	12676977	676466	81.31	17.74	0.95	12.53	0.81
420	P420	61584285	11467673	575417	83.64	15.58	0.78	12.06	0.84
430	P430	73861436	12823870	624886	84.60	14.69	0.72	11.06	0.85
440	P440	85423846	18311861	1083454	81.50	17.47	1.03	12.01	0.81
450	P450	77241685	17873812	1228580	80.17	18.55	1.28	12.06	0.80
460	P460	38817966	11687018	757090	75.72	22.80	1.48	10.45	0.76
470	P470	48920019	12528250	896997	78.47	20.09	1.44	9.87	0.78
480	P480	52337638	13481429	1165781	78.13	20.13	1.74	13.03	0.78
490	P490	26369354	8640878	801031	73.63	24.13	2.24	11.42	0.74
500	P500	35844587	8632448	500723	79.69	19.19	1.11	8.71	0.80
510	P510	28909563	8187515	513743	76.87	21.77	1.37	11.84	0.77
520	P520	59751726	16179091	1261787	77.41	20.96	1.63	15.73	0.77
530	P530	63266852	16020605	1357924	78.45	19.87	1.68	8.73	0.78
540	P540	52576492	13871471	1037581	77.91	20.55	1.54	8.51	0.78
550	P550	18675290	3963739	272141	81.51	17.30	1.19	14.26	0.82
560	P560	55718663	15062765	1286141	77.31	20.90	1.78	8.58	0.77
570	P570	40249696	12171798	856401	75.55	22.85	1.61	9.70	0.76
580	P580	24067050	9515971	918702	69.76	27.58	2.66	7.99	0.70
590	P590	60535448	25348410	2403870	68.57	28.71	2.72	11.71	0.69
600	P600	58331640	28705139	3711740	64.28	31.63	4.09	6.88	0.64
Mean					81.66	17.22	1.12	10.22	0.82

Appendix B. Elemental Analysis Results (C, N, $\delta^{13}\text{C}$, and $\delta^{15}\text{N}$)

Table B1. C and N elemental and isotopic composition of peat core RP-1A-REPA, from Danau Padang, Sumatra, Indonesia.

Depth (cm)	Sample Name	C (%) Dry Weight	N (%) Dry Weight	C/N	$\delta^{13}\text{C}$ (‰) VPDB	$\delta^{15}\text{N}$ (‰) Standard Air
10	P10	48.92	1.80	27.1	-28.72	0.006
20	P20	51.82	1.57	33.1	-28.71	-0.003
30	P30	54.19	1.66	32.7	-28.75	-0.071
40	P40	53.46	1.41	38.0	-28.90	-0.28
50	P50	52.72	1.39	38.1	-28.94	-0.668
60	P60	54.13	1.29	42.0	-29.20	-1.261
70	P70	53.68	1.44	37.2	-29.04	-0.625
80	P80	53.98	1.30	41.7	-28.84	-0.925
90	P90	54.11	1.01	53.5	-28.80	-1.181
100	P100	53.57	1.14	47.2	-28.45	-1.272
110	P110	52.83	0.92	57.3	-27.78	-1.485
120	P120	54.44	1.08	50.2	-28.77	-0.984
130	P130	54.34	0.79	68.8	-27.54	-2.263
140	P140	54.06	0.86	62.7	-28.43	-3.165
150	P150	55.23	1.22	45.2	-29.33	-2.686
160	P160	55.80	1.38	40.4	-29.30	-2.665
170	P170	55.00	1.14	48.4	-28.86	-2.473
180	P180	55.11	1.31	42.2	-28.10	-3.917
190	P190	54.96	0.95	57.7	-28.61	-2.875
200	P200	55.16	0.86	63.8	-29.04	-1.923
210	P210	54.02	1.18	45.8	-28.49	-1.242
220	P220	55.86	1.18	47.2	-28.92	-1.933
230	P230	55.30	1.18	46.8	-29.27	-0.943
240	P240	54.63	0.90	60.9	-28.34	-0.952
250	P250	55.24	1.11	49.7	-29.09	-0.533
260	P260	54.69	0.92	59.5	-28.08	-0.318
270	P270	51.32	1.02	50.2	-28.75	-0.68
280	P280	43.30	0.94	45.9	-28.40	-0.713
290	P290	49.64	0.83	60.0	-27.85	-0.437
300	P300	51.42	0.93	55.2	-28.21	-1.526
310	P310	49.40	0.87	57.0	-27.88	-2.537
320	P320	55.34	1.14	48.6	-29.25	-0.615
330	P330	55.84	0.95	58.5	-28.84	-1.643
340	P340	55.24	1.37	40.3	-28.52	0.166
350	P350	55.36	1.26	43.9	-28.74	0.703
360	P360	55.28	0.68	81.2	-28.59	-1.133
370	P370	54.99	1.08	50.7	-29.15	-0.239

380	P380	54.96	1.12	49.1	-29.02	0.316
390	P390	54.20	1.20	45.0	-28.74	0.303
400	P400	54.61	1.41	38.8	-29.67	-0.17
410	P410	55.41	0.90	61.2	-28.93	-1.064
420	P420	55.01	1.14	48.3	-29.78	-1.381
430	P430	55.04	1.17	47.0	-29.64	-0.683
440	P440	54.48	1.30	41.8	-28.94	-0.46
450	P450	53.88	1.17	45.9	-28.90	-0.231
460	P460	52.74	1.18	44.9	-29.03	1.083
470	P470	55.14	1.03	53.4	-28.77	0.655
480	P480	55.63	0.90	61.8	-28.75	0.369
490	P490	52.54	0.96	54.7	-28.08	0.713
500	P500	54.41	1.32	41.2	-29.06	1.344
510	P510	53.37	0.90	59.3	-29.67	0.153
520	P520	53.68	0.92	58.6	-28.97	0.667
530	P530	52.37	1.16	45.2	-29.00	0.872
540	P540	54.31	1.09	49.6	-29.52	0.239
550	P550	54.58	0.55	98.6	-28.53	-2.11
560	P560	53.54	1.40	38.3	-28.45	1.787
570	P570	54.39	1.28	42.3	-28.98	0.55
580	P580	53.79	1.34	40.1	-29.13	1.659
590	P590	54.76	1.36	40.4	-29.31	0.785
600	P600	54.73	1.52	36.1	-29.51	1.42
Mean		53.87	1.14	49.50	-28.81	-0.64

Appendix C. XRF Results

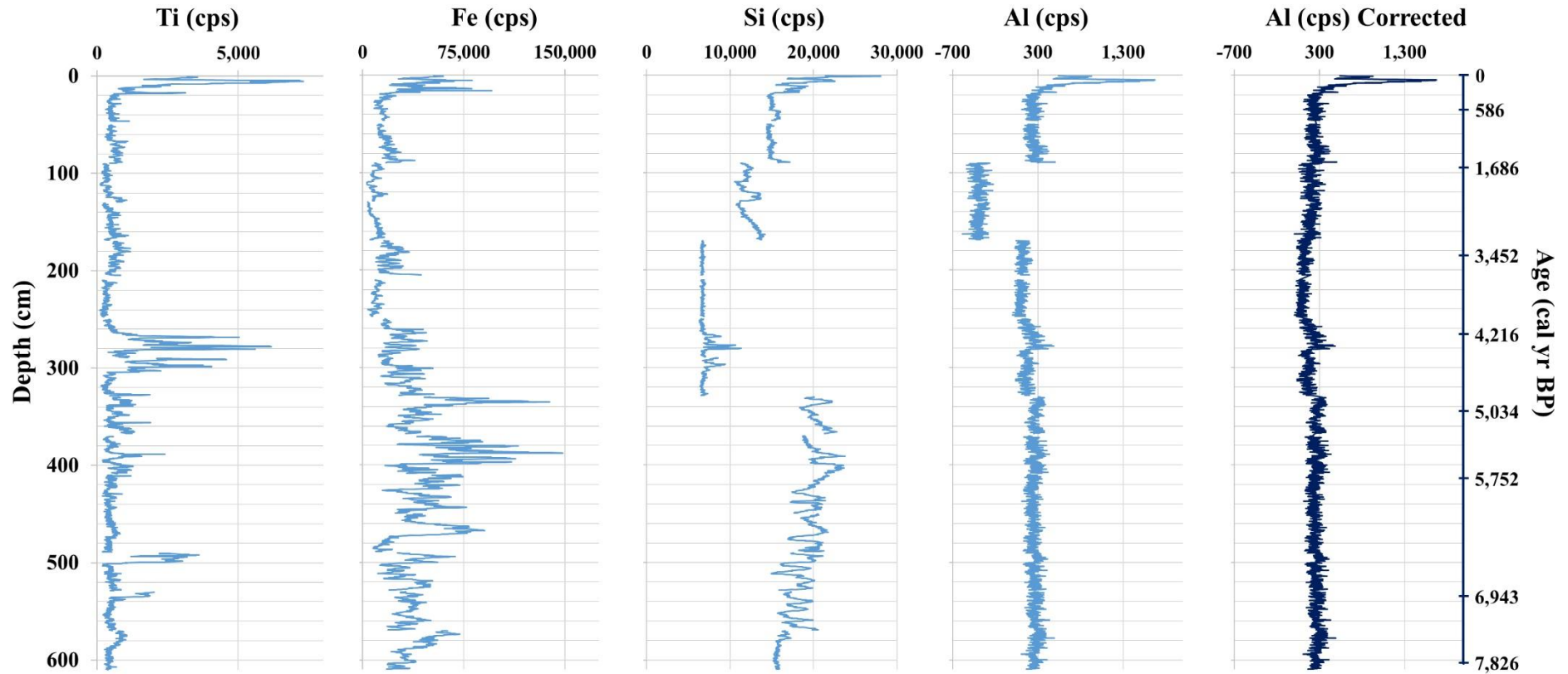


Figure C1. Results from the XRF analysis of peat core RP-1A-REPA, from Danau Padang, Sumatra, Indonesia. Ti, Fe, Si, and Al were considered the most relevant elements. The results are expressed in counts per second (cps). The misalignment was corrected for Al by calculating the difference between the average value of the twenty measurements (out of 3030) preceding and succeeding the mismatch (204.19 cps), and the mean value of the misaligned section itself (-389.77 cps). This difference (593.96 cps) was in turn added to each of the values of the mismatched section, which produced a more coherent record.

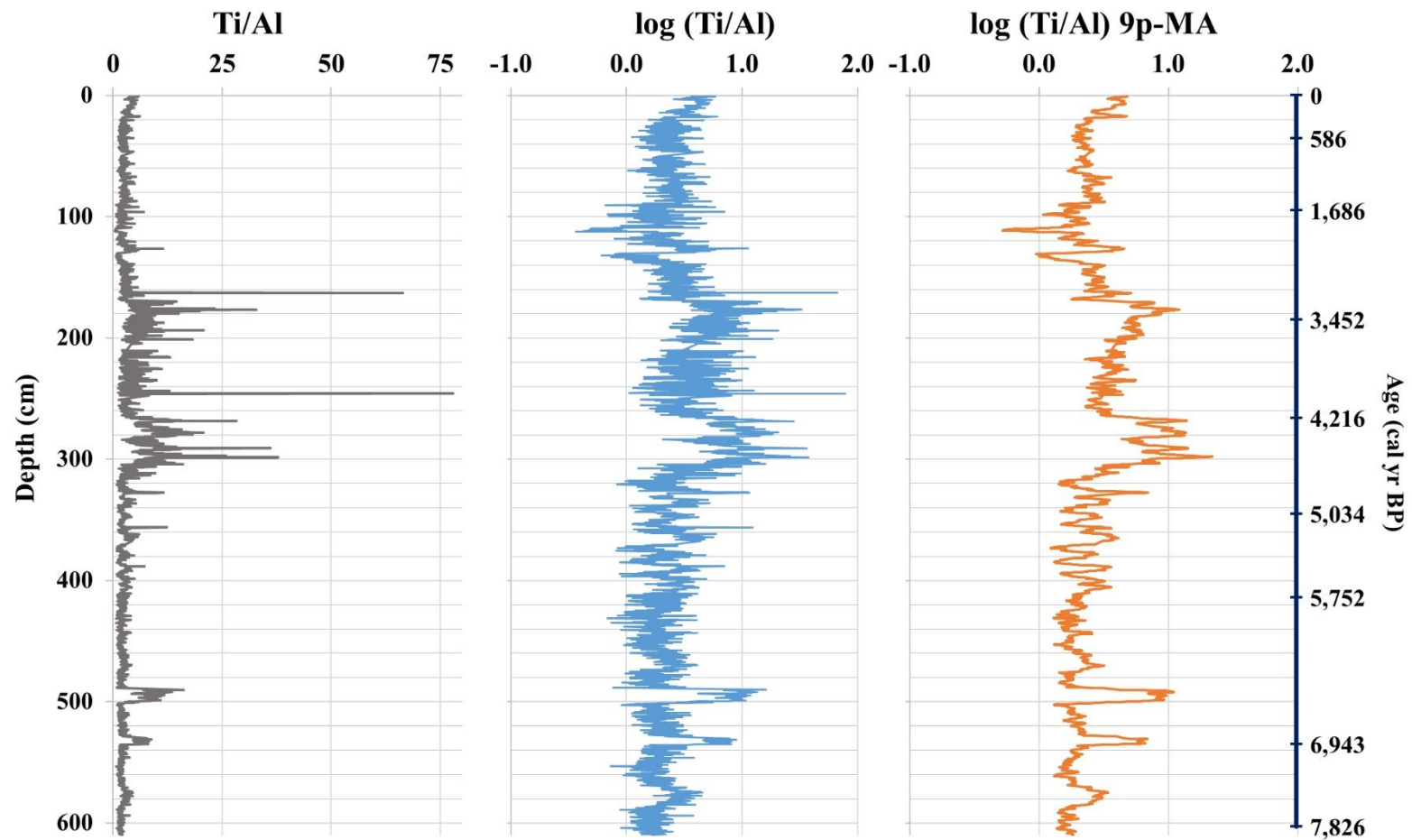


Figure C2. Results from the XRF analysis of peat core RP-1A-REPA, from Danau Padang, Sumatra, Indonesia. The graph on the left shows raw values for the ratio of Ti to Al, the middle one represents the \log_{10} of this ratio, and the curve on the right is a 9-point moving average (out of 3030) of the \log (Ti/Al).

Appendix D. Density Measurements and Carbon Accumulation Rate Calculations

Table D1. Density measurements and C accumulation rate estimates for peat core RP-1A-REPA, from Danau Padang, Sumatra, Indonesia. After freeze-drying the samples, the 60 samples were cut into rectangular prisms, they were weighted, and their dimensions were measured for density calculations. The accuracy of the measurements was estimated according to how evenly cut the rectangular prisms were. C accumulation rates were calculated from the peat accretion rates, the C content, and the density measurements, according to Page et al. 2004.

Depth (cm)	Sample Name	Volume (cm ³)	Weight (g)	Density (g/cm ³)	Measurement Accuracy	C Accumulation Rate (g/m ² *yr)
10	P10	0.768	0.15	0.195	low	51.69
20	P20	0.78	0.12	0.154	low	43.13
30	P30	2.277	0.38	0.167	low	48.93
40	P40	0.99	0.17	0.172	medium/low	49.67
50	P50	0.324	0.05	0.154	Low	44.01
60	P60	1.89	0.25	0.132	low	38.73
70	P70	1.4	0.19	0.136	high	39.41
80	P80	1.872	0.3	0.160	medium/high	46.80
90	P90	1.404	0.17	0.121	medium/high	35.44
100	P100	1.421	0.14	0.099	low	28.55
110	P110	1.2	0.11	0.092	medium	24.68
120	P120	1.08	0.12	0.111	low	30.83
130	P130	1.53	0.17	0.111	medium/low	30.77
140	P140	1.584	0.19	0.120	low	33.05
150	P150	2.295	0.26	0.113	medium/high	31.89
160	P160	1.584	0.2	0.126	high	35.91
170	P170	1.71	0.2	0.117	high	32.78
180	P180	1.008	0.14	0.139	low	39.01
190	P190	1.296	0.13	0.100	low	28.10
200	P200	1.53	0.25	0.163	medium	95.54
210	P210	2.475	0.37	0.149	high	85.59
220	P220	2.592	0.31	0.120	medium	70.81
230	P230	1.782	0.23	0.129	high	75.66
240	P240					
250	P250	1.152	0.15	0.130	medium/low	76.23
260	P260					
270	P270	2.772	0.31	0.112	high	55.42
280	P280	1.857	0.29	0.156	medium/high	65.29
290	P290	2.268	0.37	0.163	medium/low	78.20
300	P300	1.872	0.3	0.160	medium	79.57
310	P310	2.1	0.26	0.124	medium/low	59.07
320	P320	1.92	0.29	0.151	medium	80.71
330	P330	2.28	0.28	0.123	medium/high	66.22
340	P340	1.87	0.25	0.134	medium/low	71.31

350	P350	1.08	0.12	0.111	medium	59.40
360	P360	1.296	0.13	0.100	low	53.28
370	P370	1.9	0.24	0.126	medium/high	66.74
380	P380	2.42	0.31	0.128	medium	67.65
390	P390	1.539	0.27	0.175	high	91.36
400	P400	2.64	0.33	0.125	high	65.59
410	P410	2.662	0.32	0.120	high	64.01
420	P420	1.98	0.23	0.116	high	61.40
430	P430	1.26	0.19	0.151	low	84.38
440	P440	1.368	0.21	0.154	low	85.01
450	P450	1.68	0.25	0.149	medium/low	81.50
460	P460					
470	P470	1.296	0.19	0.147	medium/high	82.17
480	P480	0.882	0.14	0.159	medium/low	89.77
490	P490	0.576	0.06	0.104	low	55.63
500	P500	2.772	0.31	0.112	medium/high	61.85
510	P510	1.76	0.2	0.114	medium/low	61.65
520	P520	1.89	0.29	0.153	medium/high	83.73
530	P530	2.002	0.27	0.135	medium	71.80
540	P540	1.54	0.15	0.097	medium/low	53.77
550	P550	0.558	0.1	0.179	Low	75.25
560	P560	1.35	0.24	0.178	high	73.23
570	P570	0.648	0.09	0.139	medium	58.11
580	P580	1.8	0.19	0.106	high	43.68
590	P590	1.62	0.22	0.136	high	57.21
600	P600	1.5	0.26	0.173	medium	72.98

Appendix E. Alternative Chromatographic Peak Integrations

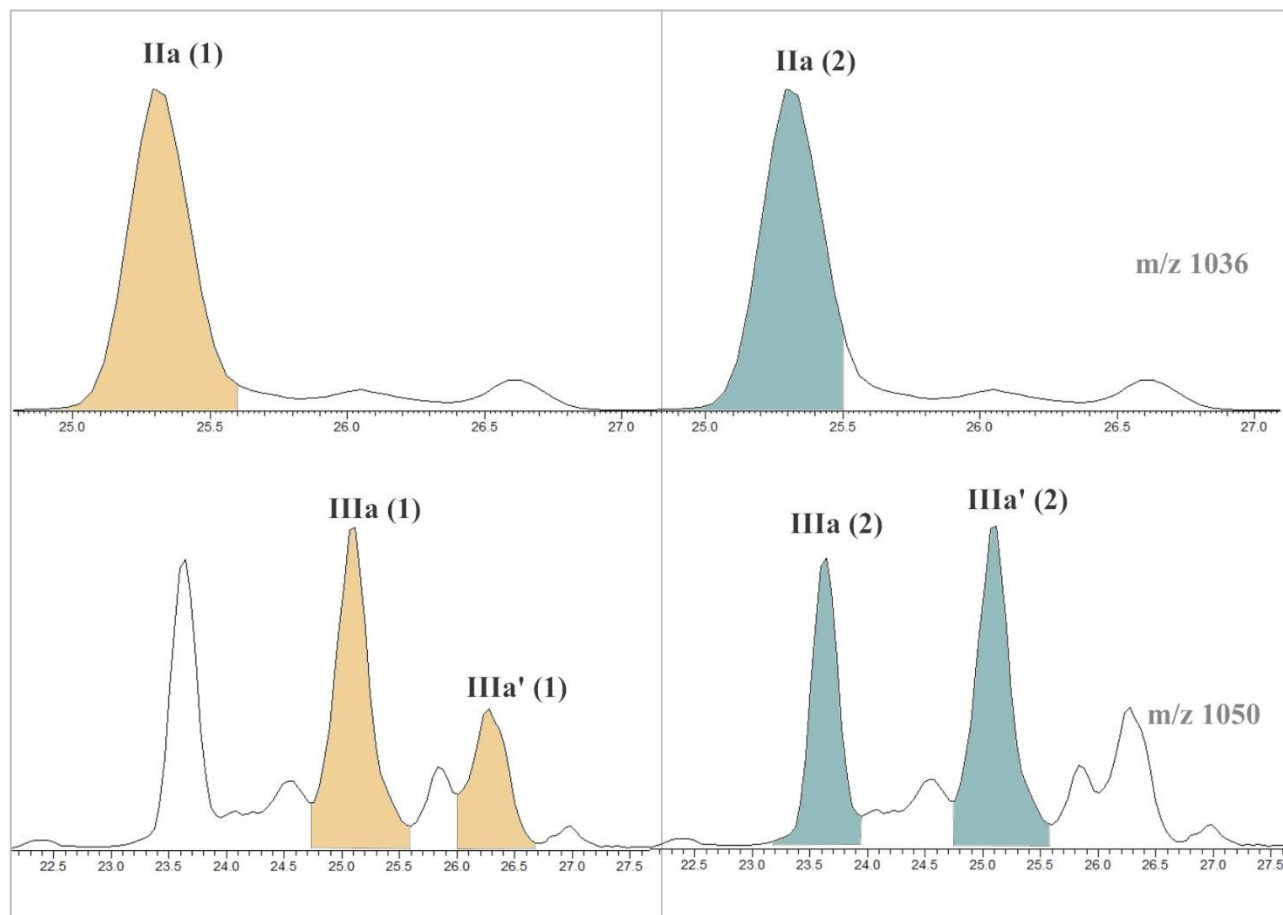


Figure E1. Alternative chromatographic peak integrations for peat core RP-1A-REPA, from Danau Padang, Sumatra, Indonesia. BrGDGTs-IIa, -IIIa, and -IIIa' were the ones whose integration was contentious and that at the same time could have an impact on brGDGT-based proxies. IIa (2), IIIa (2) and IIIa' (2) were considered the most suitable integrations.

Table E1. Chromatographic peak areas of alternative integrations for peat core RP-1A-REPA (first LC-MS run), from Danau Padang, Sumatra, Indonesia. BrGDGTs-IIa, -IIIa, and -IIIa' were the ones whose integration was contentious and that at the same time could have an impact on brGDGT-based proxies. IIa (2), IIIa (2) and IIIa' (2) were considered the most suitable integrations.

Depth (cm)	Sample Name	Area IIIa (1)	Area IIIa (2)	Area IIIa' (1)	Area IIIa' (2)	Area IIa (1)	Area IIa (2)
10	P10	2124090	703011	1459484	2124090	39769638	38609594
20	P20	2437101	442834	1455737	2437101	17914486	17544892
30	P30	6041676	1297085	3065499	6041676	45482174	43670496
40	P40	8332901	2147386	3653587	8332901	66842257	64589888
50	P50	5990183	1388623	2864373	5990183	48078679	46122811
60	P60	8555449	2177888	3847242	8555449	71730478	68543387
70	P70	9382825	2614970	3829913	9382825	66874605	63391795
80	P80	8701718	3046794	3836951	8701718	90983330	87703968
90	P90	4658749	1365134	2479975	4658749	42276634	41021592
100	P100	1750445	527990	1096202	1750445	19796359	19126104
110	P110	1870414	715790	892263	1870414	21985347	21310318
120	P120	3789829	1412340	2235788	3789829	40478306	38869288
130	P130	6717046	4978667	3267277	6717046	105051152	102303049
140	P140	5706075	3268599	2753220	5706075	83523008	81465957
150	P150	6981316	2234656	4369459	6981316	77526352	72300592
160	P160	7098374	2618820	4771479	7098374	88068651	84567894
170	P170	14943017	6229021	6650072	14943017	195531385	183669458
180	P180	12310964	3677887	6020627	12310964	152423744	139420930
190	P190	10127829	3788242	3981751	10127829	122178783	114304713
200	P200	5622177	2521208	4295070	5622177	63388312	59834863
210	P210	8201746	4017649	3461389	8201746	88000779	82075977
220	P220	14215110	7043655	6831854	14215110	203686127	191656052
230	P230	10688933	4434019	4657887	10688933	108534526	103605130
240	P240	8897878	3740729	6284000	8897878	112542513	107882846
250	P250	6986843	2750979	3367537	6986843	70960403	66965420
260	P260	13970860	11062406	5373951	13970860	212890697	200777519
270	P270	8613377	6126767	2971144	8613377	105479117	100717561
280	P280	13384866	13212669	4019198	13384866	191747712	183200761
290	P290	12708891	9014630	3776649	12708891	152015889	144191862
300	P300	11146516	9941554	4971102	11146516	170473312	162847371
310	P310	9049407	5358197	5639160	9049407	178244791	170515661
320	P320	5210861	2852202	2789509	5210861	68483332	65669853
330	P330	3814932	1569483	2727226	3814932	47412072	45373348
340	P340	4556459	1812727	3158864	4556459	56005498	53270541
350	P350	6779978	4185710	3588918	6779978	106463196	100860188
360	P360	4011705	2088717	2593440	4011705	54484684	52986257
370	P370	7144850	3949330	3683670	7144850	98449341	95655035
380	P380	7209786	5032743	3055333	7209786	101040853	95826726

390	P390	8030638	4536049	3250747	8030638	97022808	93237131
400	P400	8329621	5229126	4523827	8329621	106256061	101348419
410	P410	5982538	3427188	4246983	5982538	84254464	80496891
420	P420	6958193	3326073	4173150	6958193	80116559	75344204
430	P430	8071755	4056694	4323694	8071755	91023750	86708476
440	P440	10605095	6855425	4703399	10605095	135646902	126358059
450	P450	10814401	6037153	4399290	10814401	115407623	110606182
460	P460	6908077	4721916	2933137	6908077	77692107	74162564
470	P470	8003116	5279519	3880095	8003116	93298223	89280755
480	P480	6119881	3662201	3184434	6119881	65733463	62348369
490	P490	4983426	2543746	1614285	4983426	42933888	41243699
500	P500	6464379	4719704	2616447	6464379	70838104	65607997
510	P510	4827204	2713256	1885456	4827204	45321516	43324421
520	P520	7407981	4662849	2748283	7407981	68382125	65376988
530	P530	11878282	10910476	4062371	11878282	157985767	147915196
540	P540	9093705	10421997	3592379	9093705	147913595	139336401
550	P550	2463234	1349195	1489417	2463234	23586847	22552626
560	P560	8398230	6614908	3062881	8398230	103489995	97590492
570	P570	7659386	7354550	2633195	7659386	91797414	88169555
580	P580	5476428	6285140	1605764	5476428	80883280	77208714
590	P590	11200807	13800649	3027798	11200807	152672666	147037035
600	P600	18564001	32062111	4849712	18564001	292080884	278005034

Table E2. MBT'5me index (De Jonge et al. 2014) and MAAT °C (Naafs et al. 2017a) calculated for the alternative chromatographic peak integrations (see Fig. E1 and Table E1) for peat core RP-1A-REPA (first LC-MS run), from Danau Padang, Sumatra, Indonesia. BrGDGTs-IIa, -IIIa, and -IIIa' were the ones whose integration was contentious and that at the same time could have had an impact on br-GDGT-based proxies. SD=standard deviation, CV=coefficient of variation).

Sample Name	MBT'5me IIIa (1) & IIa (1)	MAAT IIIa (1) & IIa (1)	MBT'5me IIIa (2) & IIa (1)	MAAT IIIa (2) & IIa (1)	MBT'5me IIIa (2) & IIa (2)	MAAT IIIa (2) & IIa (2)	MBT'5me IIIa (1) & IIa (2)	MAAT IIIa (1) & IIa (2)	SD MBT 5'me	SD MAAT	CV (%)
P10	0.92	24.86	0.92	25.00	0.92	25.10	0.92	24.97	0.0019	0.099	0.205
P20	0.96	26.82	0.96	27.03	0.96	27.07	0.96	26.86	0.0024	0.125	0.249
P30	0.93	25.51	0.94	25.82	0.94	25.94	0.93	25.63	0.0036	0.189	0.388
P40	0.92	25.17	0.93	25.47	0.93	25.57	0.93	25.28	0.0035	0.183	0.378
P50	0.93	25.53	0.94	25.81	0.94	25.93	0.93	25.65	0.0034	0.177	0.362
P60	0.92	24.87	0.92	25.18	0.93	25.33	0.92	25.03	0.0038	0.198	0.412
P70	0.93	25.30	0.93	25.61	0.94	25.78	0.93	25.46	0.0039	0.202	0.416
P80	0.91	24.37	0.91	24.61	0.92	24.75	0.91	24.51	0.0031	0.163	0.342
P90	0.91	24.35	0.91	24.65	0.92	24.77	0.91	24.46	0.0036	0.187	0.393
P100	0.90	24.13	0.91	24.38	0.91	24.52	0.91	24.27	0.0032	0.168	0.355
P110	0.90	23.93	0.90	24.16	0.91	24.29	0.90	24.06	0.0029	0.151	0.320
P120	0.92	24.88	0.92	25.09	0.93	25.23	0.92	25.02	0.0028	0.145	0.301
P130	0.83	20.26	0.83	20.37	0.84	20.56	0.83	20.44	0.0024	0.124	0.285
P140	0.86	21.61	0.86	21.78	0.86	21.93	0.86	21.75	0.0025	0.132	0.294
P150	0.90	24.17	0.91	24.42	0.92	24.70	0.91	24.45	0.0041	0.216	0.456
P160	0.88	22.68	0.88	22.95	0.89	23.15	0.88	22.89	0.0037	0.194	0.421
P170	0.85	21.11	0.85	21.39	0.86	21.77	0.85	21.49	0.0053	0.275	0.618
P180	0.88	23.11	0.89	23.39	0.90	23.81	0.89	23.53	0.0056	0.293	0.630
P190	0.85	21.39	0.86	21.70	0.87	22.10	0.86	21.78	0.0056	0.293	0.654
P200	0.87	22.11	0.87	22.39	0.88	22.70	0.87	22.43	0.0046	0.240	0.529
P210	0.90	23.67	0.90	23.88	0.91	24.18	0.90	23.96	0.0041	0.213	0.453
P220	0.85	21.40	0.86	21.62	0.86	21.99	0.86	21.77	0.0047	0.245	0.549
P230	0.87	22.50	0.88	22.80	0.88	23.05	0.88	22.74	0.0043	0.223	0.487

P240	0.86	21.94	0.87	22.20	0.87	22.44	0.87	22.17	0.0039	0.205	0.454
P250	0.88	22.71	0.88	23.02	0.89	23.31	0.88	23.00	0.0047	0.243	0.528
P260	0.78	17.78	0.78	17.90	0.79	18.37	0.79	18.26	0.0054	0.283	0.688
P270	0.83	20.28	0.83	20.44	0.84	20.74	0.84	20.58	0.0038	0.199	0.457
P280	0.80	18.94	0.80	18.94	0.81	19.28	0.81	19.28	0.0038	0.196	0.464
P290	0.82	19.86	0.83	20.03	0.83	20.40	0.83	20.22	0.0044	0.231	0.535
P300	0.81	19.47	0.82	19.52	0.82	19.86	0.82	19.80	0.0037	0.193	0.451
P310	0.84	21.03	0.85	21.16	0.85	21.45	0.85	21.31	0.0035	0.181	0.408
P320	0.89	23.38	0.89	23.54	0.90	23.74	0.89	23.58	0.0028	0.146	0.313
P330	0.90	23.82	0.90	24.03	0.91	24.22	0.90	24.01	0.0031	0.162	0.345
P340	0.90	23.92	0.90	24.13	0.91	24.34	0.90	24.13	0.0033	0.172	0.365
P350	0.87	22.17	0.87	22.31	0.87	22.60	0.87	22.47	0.0036	0.188	0.414
P360	0.87	22.29	0.87	22.49	0.88	22.64	0.87	22.44	0.0027	0.142	0.313
P370	0.86	21.91	0.87	22.10	0.87	22.26	0.86	22.08	0.0027	0.143	0.318
P380	0.85	21.10	0.85	21.24	0.85	21.56	0.85	21.42	0.0039	0.203	0.457
P390	0.86	22.02	0.87	22.22	0.87	22.44	0.87	22.24	0.0033	0.172	0.380
P400	0.88	22.64	0.88	22.80	0.88	23.04	0.88	22.88	0.0032	0.164	0.358
P410	0.85	21.11	0.85	21.30	0.86	21.59	0.85	21.39	0.0038	0.197	0.444
P420	0.86	21.93	0.87	22.18	0.87	22.52	0.87	22.26	0.0047	0.246	0.543
P430	0.88	22.80	0.88	23.02	0.89	23.27	0.88	23.04	0.0036	0.190	0.413
P440	0.84	20.75	0.84	20.93	0.85	21.38	0.85	21.19	0.0053	0.277	0.628
P450	0.85	21.17	0.85	21.42	0.86	21.68	0.85	21.43	0.0040	0.208	0.468
P460	0.83	20.39	0.84	20.58	0.84	20.88	0.84	20.69	0.0039	0.205	0.470
P470	0.84	21.00	0.85	21.18	0.85	21.45	0.85	21.27	0.0036	0.188	0.425
P480	0.86	22.01	0.87	22.22	0.87	22.51	0.87	22.30	0.0039	0.205	0.453
P490	0.85	21.39	0.86	21.72	0.86	21.95	0.86	21.62	0.0045	0.233	0.521
P500	0.86	21.68	0.86	21.82	0.87	22.25	0.87	22.10	0.0050	0.260	0.577
P510	0.85	21.13	0.85	21.41	0.86	21.68	0.85	21.39	0.0043	0.225	0.507
P520	0.85	21.28	0.85	21.52	0.86	21.78	0.85	21.54	0.0039	0.204	0.458

P530	0.82	19.93	0.82	19.98	0.83	20.42	0.83	20.38	0.0049	0.257	0.595
P540	0.81	19.23	0.81	19.16	0.82	19.59	0.82	19.66	0.0048	0.253	0.596
P550	0.84	20.94	0.85	21.22	0.85	21.49	0.85	21.20	0.0043	0.226	0.510
P560	0.87	22.37	0.87	22.46	0.88	22.76	0.88	22.67	0.0035	0.183	0.400
P570	0.83	20.10	0.83	20.13	0.83	20.39	0.83	20.37	0.0030	0.154	0.356
P580	0.81	19.13	0.81	19.05	0.81	19.39	0.81	19.46	0.0038	0.199	0.471
P590	0.79	18.29	0.79	18.16	0.80	18.45	0.80	18.58	0.0035	0.183	0.443
P600	0.78	17.45	0.77	17.07	0.78	17.47	0.78	17.85	0.0061	0.320	0.790

Table E3. CBTpeat index and pH (Naafs et al. 2017a) calculated for the alternative chromatographic peak integrations (see Fig. E1 and Table E1) for peat core RP-1A-REPA (first LC-MS run), from Danau Padang, Sumatra, Indonesia. BrGDGTs-IIa, -IIIa, and -IIIa' were the ones whose integration was contentious and that at the same time could have had an impact on br-GDGT-based proxies. SD=standard deviation, CV=coefficient of variation).

Sample Name	CBTpeat IIIa (1) & IIa (1)	pH IIIa (1) & IIa (1)	CBTpeat IIIa (2) & IIa (1)	pH IIIa (2) & IIa (1)	CBTpeat IIIa (2) & IIa (2)	pH IIIa (2) & IIa (2)	CBTpeat IIIa (1) & IIa (2)	pH IIIa (1) & IIa (2)	SD CBTpeat	SD pH	CV (%)
P10	-1.79	3.61	-1.75	3.70	-1.75	3.70	-1.79	3.62	0.020	0.050	1.14
P20	-1.36	4.67	-1.34	4.73	-1.34	4.73	-1.36	4.67	0.014	0.034	1.01
P30	-1.47	4.41	-1.42	4.54	-1.42	4.54	-1.47	4.41	0.030	0.076	2.10
P40	-1.36	4.68	-1.31	4.80	-1.31	4.80	-1.36	4.68	0.029	0.071	2.14
P50	-1.39	4.60	-1.35	4.71	-1.35	4.71	-1.39	4.60	0.026	0.065	1.90
P60	-1.42	4.52	-1.37	4.67	-1.37	4.67	-1.42	4.53	0.033	0.081	2.33
P70	-1.49	4.35	-1.42	4.53	-1.42	4.53	-1.49	4.36	0.041	0.102	2.82
P80	-1.59	4.11	-1.52	4.29	-1.52	4.29	-1.59	4.11	0.042	0.105	2.72
P90	-1.58	4.13	-1.51	4.30	-1.51	4.31	-1.58	4.13	0.040	0.100	2.59
P100	-1.64	3.98	-1.59	4.12	-1.59	4.12	-1.64	3.98	0.032	0.080	1.98
P110	-1.71	3.80	-1.63	4.02	-1.63	4.02	-1.71	3.81	0.050	0.124	2.99
P120	-1.59	4.11	-1.54	4.23	-1.54	4.23	-1.59	4.11	0.028	0.070	1.79

P130	-1.83	3.50	-1.70	3.84	-1.70	3.84	-1.83	3.51	0.078	0.194	4.42
P140	-1.79	3.60	-1.68	3.89	-1.68	3.89	-1.79	3.61	0.066	0.165	3.82
P150	-1.76	3.68	-1.69	3.86	-1.69	3.86	-1.76	3.69	0.041	0.103	2.39
P160	-1.58	4.13	-1.53	4.26	-1.53	4.26	-1.58	4.13	0.029	0.073	1.89
P170	-1.65	3.96	-1.54	4.23	-1.54	4.24	-1.65	3.97	0.063	0.156	3.94
P180	-1.76	3.68	-1.66	3.93	-1.66	3.94	-1.76	3.69	0.059	0.148	3.47
P190	-1.76	3.69	-1.61	4.06	-1.61	4.07	-1.76	3.69	0.087	0.216	5.15
P200	-1.65	3.96	-1.60	4.09	-1.60	4.10	-1.65	3.97	0.029	0.073	1.81
P210	-1.59	4.11	-1.51	4.31	-1.51	4.32	-1.59	4.11	0.048	0.120	3.11
P220	-1.69	3.86	-1.59	4.11	-1.59	4.12	-1.69	3.87	0.057	0.142	3.49
P230	-1.68	3.90	-1.56	4.20	-1.55	4.20	-1.67	3.90	0.069	0.172	4.29
P240	-1.73	3.76	-1.66	3.93	-1.66	3.94	-1.73	3.77	0.039	0.097	2.29
P250	-1.65	3.96	-1.55	4.21	-1.55	4.22	-1.65	3.96	0.060	0.149	3.73
P260	-1.70	3.83	-1.55	4.21	-1.54	4.23	-1.70	3.84	0.089	0.222	5.49
P270	-1.56	4.17	-1.44	4.47	-1.44	4.48	-1.56	4.18	0.069	0.172	4.61
P280	-1.63	4.02	-1.49	4.37	-1.48	4.38	-1.62	4.03	0.081	0.203	5.24
P290	-1.66	3.93	-1.50	4.34	-1.50	4.35	-1.66	3.94	0.094	0.234	5.95
P300	-1.70	3.84	-1.58	4.14	-1.57	4.15	-1.69	3.85	0.070	0.173	4.25
P310	-1.72	3.79	-1.66	3.95	-1.65	3.95	-1.72	3.80	0.036	0.089	2.13
P320	-1.53	4.26	-1.48	4.39	-1.48	4.40	-1.53	4.26	0.031	0.077	2.05
P330	-1.69	3.85	-1.65	3.97	-1.65	3.97	-1.69	3.85	0.027	0.067	1.62
P340	-1.56	4.17	-1.53	4.27	-1.52	4.27	-1.56	4.18	0.022	0.055	1.42
P350	-1.59	4.11	-1.53	4.26	-1.53	4.27	-1.59	4.11	0.036	0.089	2.30
P360	-1.76	3.68	-1.69	3.87	-1.69	3.87	-1.76	3.68	0.044	0.109	2.54
P370	-1.62	4.05	-1.54	4.24	-1.54	4.24	-1.61	4.05	0.045	0.112	2.84
P380	-1.50	4.32	-1.43	4.52	-1.42	4.53	-1.50	4.33	0.045	0.113	3.10
P390	-1.50	4.33	-1.42	4.54	-1.42	4.54	-1.50	4.34	0.047	0.118	3.25
P400	-1.52	4.29	-1.46	4.43	-1.46	4.44	-1.52	4.29	0.034	0.084	2.26
P410	-1.61	4.06	-1.56	4.19	-1.55	4.20	-1.61	4.07	0.030	0.075	1.90

P420	-1.56	4.17	-1.50	4.35	-1.49	4.35	-1.56	4.18	0.040	0.099	2.61
P430	-1.56	4.17	-1.49	4.35	-1.49	4.36	-1.56	4.18	0.041	0.103	2.69
P440	-1.46	4.44	-1.38	4.63	-1.38	4.64	-1.45	4.45	0.045	0.112	3.18
P450	-1.52	4.29	-1.41	4.55	-1.41	4.55	-1.52	4.30	0.060	0.149	4.08
P460	-1.60	4.09	-1.48	4.40	-1.47	4.40	-1.59	4.10	0.070	0.175	4.57
P470	-1.55	4.21	-1.46	4.44	-1.46	4.45	-1.55	4.22	0.053	0.131	3.51
P480	-1.61	4.06	-1.52	4.29	-1.52	4.29	-1.61	4.06	0.053	0.133	3.41
P490	-1.51	4.31	-1.38	4.64	-1.38	4.65	-1.51	4.32	0.076	0.189	5.25
P500	-1.41	4.56	-1.33	4.75	-1.33	4.76	-1.40	4.58	0.044	0.110	3.23
P510	-1.54	4.23	-1.42	4.54	-1.42	4.54	-1.54	4.24	0.071	0.177	4.80
P520	-1.53	4.27	-1.40	4.57	-1.40	4.58	-1.52	4.28	0.070	0.175	4.79
P530	-1.40	4.59	-1.31	4.80	-1.31	4.81	-1.39	4.61	0.048	0.119	3.53
P540	-1.43	4.51	-1.36	4.69	-1.35	4.70	-1.42	4.52	0.042	0.105	3.03
P550	-1.22	5.03	-1.18	5.14	-1.17	5.15	-1.22	5.04	0.026	0.064	2.13
P560	-1.41	4.55	-1.35	4.72	-1.34	4.73	-1.41	4.56	0.038	0.095	2.78
P570	-1.30	4.84	-1.23	5.02	-1.22	5.02	-1.30	4.84	0.042	0.104	3.32
P580	-1.35	4.72	-1.27	4.91	-1.26	4.92	-1.34	4.73	0.045	0.112	3.43
P590	-1.28	4.87	-1.20	5.07	-1.20	5.08	-1.28	4.88	0.047	0.116	3.75
P600	-1.24	4.98	-1.17	5.15	-1.17	5.16	-1.24	4.99	0.039	0.098	3.26

Appendix F. Other MBT_{5ME} Temperature Calibrations

Table F1. Two soil MBT_{5ME} temperature calibrations applied to peat core RP-1A-REPA, Danau Padang, Sumatra, Indonesia.

De Jonge et al. 2014 (soil)	$MAAT (^{\circ}C) = -8.57 + 31.45 \times MBT'5me$	N = 222, R ² = 0.66, RMSE = 4.8
Naafs et al. 2017b (soils)	$MAAT (^{\circ}C) = 40.01 \times MBT'5me - 15.25$	N = 350, R ² = 0.60, RMSE = 5.3

Table F2. Different temperature calibrations applied to the MBT_{5ME} index from peat core RP-1A-REPA, Danau Padang, Sumatra, Indonesia. The left-most column contains proposed temperatures given that today's average yearly temperature at the study site is 22 °C, and supposing a maximum temperature variability of 3 °C during the last 7,787 yr.

Depth (cm)	Sample Name	Naafs et al. 2017a (peat)	Dearing Crampton-Flood et al. 2020 (both)	De Jonge et al. 2014 (soil)	Naafs et al. 2017b (soil)	Proposed Temperature
10	P10	25.17	24.28	20.49	21.73	21.37
20	P20	27.08	25.72	21.64	23.19	22.00
30	P30	25.97	25.01	20.98	22.34	21.64
40	P40	25.76	24.66	20.85	22.18	21.57
50	P50	25.99	25.03	20.99	22.35	21.64
60	P60	25.87	25.00	20.92	22.26	21.60
70	P70	25.60	24.60	20.75	22.06	21.52
80	P80	24.42	23.84	20.04	21.15	21.13
90	P90	25.12	24.27	20.46	21.69	21.36
100	P100	24.84	24.32	20.30	21.47	21.27
110	P110	24.64	23.85	20.17	21.32	21.20
120	P120	25.42	24.39	20.64	21.92	21.46
130	P130	20.52	21.73	17.69	18.16	19.85
140	P140	22.39	22.68	18.82	19.60	20.46
150	P150	25.26	24.46	20.55	21.80	21.40
160	P160	23.19	23.38	19.30	20.21	20.73
170	P170	21.94	22.18	18.54	19.24	20.31
180	P180	23.75	23.54	19.64	20.63	20.91
190	P190	22.47	22.73	18.87	19.66	20.49
200	P200	22.85	23.07	19.09	19.94	20.61
210	P210	24.26	23.88	19.94	21.02	21.07
220	P220	21.85	22.26	18.49	19.17	20.28
230	P230	22.95	23.10	19.15	20.02	20.65
240	P240	22.54	22.90	18.91	19.71	20.51
250	P250	23.24	23.26	19.33	20.24	20.74
260	P260	19.30	20.92	16.95	17.22	19.45
270	P270	21.00	21.81	17.98	18.52	20.01

280	P280	19.51	21.13	17.08	17.38	19.52
290	P290	20.67	21.61	17.78	18.27	19.90
300	P300	20.35	21.41	17.59	18.02	19.79
310	P310	21.64	22.07	18.37	19.02	20.22
320	P320	23.99	23.74	19.78	20.82	20.99
330	P330	24.23	23.56	19.93	21.00	21.07
340	P340	24.50	24.23	20.09	21.21	21.16
350	P350	22.64	22.67	18.97	19.78	20.54
360	P360	22.88	22.98	19.12	19.97	20.62
370	P370	22.05	22.31	18.61	19.33	20.35
380	P380	21.79	22.37	18.45	19.13	20.26
390	P390	22.54	22.53	18.91	19.71	20.51
400	P400	23.30	23.37	19.37	20.29	20.76
410	P410	21.80	22.34	18.47	19.14	20.27
420	P420	22.54	22.69	18.91	19.71	20.51
430	P430	23.01	23.22	19.19	20.07	20.67
440	P440	21.78	22.33	18.45	19.13	20.26
450	P450	21.75	22.68	18.43	19.10	20.25
460	P460	21.46	22.20	18.26	18.88	20.16
470	P470	21.25	21.92	18.13	18.72	20.09
480	P480	22.60	22.92	18.94	19.75	20.53
490	P490	22.31	22.61	18.77	19.53	20.44
500	P500	21.92	22.51	18.54	19.23	20.31
510	P510	22.23	22.88	18.72	19.47	20.41
520	P520	21.83	22.33	18.48	19.16	20.28
530	P530	20.42	21.33	17.63	18.08	19.82
540	P540	19.99	21.15	17.37	17.75	19.68
550	P550	22.04	22.64	18.60	19.32	20.35
560	P560	22.78	23.12	19.05	19.89	20.59
570	P570	21.07	22.12	18.02	18.58	20.03
580	P580	19.71	20.95	17.20	17.53	19.58
590	P590	18.60	20.28	16.53	16.68	19.22
600	P600	17.93	19.55	16.13	16.17	19.00